

# Hydro-elasticity of a Bulge Wave Energy Converter in the 2D Frank Close-Fit Method

MT54015 MSc Thesis

L. J. Kemp



# Hydro-elasticity of a Bulge Wave Energy Converter in the 2D Frank Close-Fit Method

MT54015 MSc Thesis

by

L. J. Kemp

to obtain the degree of Master of Science  
at the Delft University of Technology,  
to be defended publicly on Monday May 13, 2019 at 15:00.

Student number: 4239350  
Project duration: September 3, 2018 – May 13, 2019  
Thesis committee: Dr. ir. P. R. Wellens, TU Delft, supervisor  
Dr. ir. H. J. de Koning Gans, TU Delft  
Dr. ir. J. F. J. Pruijn, TU Delft

An electronic version of this thesis is available at <http://repository.tudelft.nl/>.

The figure placed on the cover is retrieved from [3].



# Preface

This report is part of the MSc thesis project to obtain the MSc degree Maritime Technology at Delft University of Technology. The thesis project is performed at Delft University of Technology, department of Maritime and Transport Technology at Ship Hydromechanics and Structures. The subject of this thesis connects the goals of a research assignment about the Frank close-fit method [39] to one of my interests, wave energy.

The main methodology and findings of this study are presented in a paper, which is the main part of this report. Readers who are particularly interested in the theory of Frank and the implementation of this method into Matlab, should read Appendix C and D. Appendix A and B indicate the background of the observed goal and the research steps in the graduation research. The three-dimensional response of a Bulge Wave Energy converter is observed in the Appendices E and F.

I would like to express my gratitude to my daily supervisor, Peter Wellens and the other graduation committee members for guidance during the graduation process. Big thanks to my fellow students Willemijn, Renske and Maarten that inspired me during our brainstorming. I would also express my appreciation to Lisette, Danique, Maarten, Benno, Martijn and Johan for reading my paper and appendices. Next, I have to thank my family and friends for their endless support in the former years of my educational career.

*L. J. Kemp*  
*Delft, May 2019*



# List of Symbols

## Greek symbols

$\alpha$	Angle between element and the x-axis (in <i>Appendix C and D</i> )	[rad]
$\alpha_f$	Fractional coefficient for rubber (in <i>Appendix A</i> )	[-]
$\alpha_n$	Scaling variable for the n-th mode in the <i>modal analysis</i>	[-]
$\beta$	Energy loss coefficient (in <i>Appendix A</i> )	[s]
$\gamma$	Hysteresis loss coefficient in tube material (in <i>Appendix B</i> )	[m <sup>-1</sup> ]
$\gamma_1, \gamma_2$	Frequency related parameter for bulging in <i>modal analysis</i>	[-]
$\Gamma_n$	Generalised force in <i>modal analysis</i>	[N]
$\delta$	Loss angle of tube's material	[°]
$\delta\lambda$	Deformation rate in <i>modal analysis</i>	[-]
$\varepsilon$	Convergence value in <i>modal analysis</i>	[-]
$\varepsilon_0$	Amplitude of hoop strain (in <i>Appendix B</i> )	[-]
$\varepsilon_h$	Hoop strain (in <i>Appendix A</i> )	[-]
$\zeta$	Complex variable	[-]
$\zeta$	Time-dependent wave amplitude	[m]
$\zeta_I$	Incident wave amplitude	[m]
$\eta$	Rate of strain (wall damping) coefficient	[m <sup>2</sup> /s]
$\eta_{wec}$	Efficiency of the WEC	[-]
$\theta$	Plane angle in polar, cylindrical and spherical coordinate system	[rad]
$\theta$	Phase difference in <i>modal analysis</i>	[rad]
$\Theta^{(m)}$	Displacement of the forced harmonic oscillation in the <i>FCFM</i>	[m]
$\dot{\Theta}^{(m)}$	Velocity of the forced harmonic oscillation in the <i>FCFM</i>	[m/s]
$\ddot{\Theta}^{(m)}$	Acceleration of the forced harmonic oscillation in the <i>FCFM</i>	[m/s <sup>2</sup> ]
$\lambda$	Wavelength of the incident wave	[m]
$\lambda_n$	n-th wavelength of force resonance in <i>Modal analysis</i>	
$\nu$	Wavenumber	[m <sup>-1</sup> ]
$\nu_b$	Wavenumber of bulge wave	[m <sup>-1</sup> ]
$\xi_n$	Modal coordinate for bulging modes in <i>modal analysis</i>	[m]
$\rho$	Fluid density	[kg/m <sup>3</sup> ]
$\rho_{tube}$	Density of tube's material	[kg/m <sup>3</sup> ]
$\sigma_\theta$	Hoop stress (in <i>Appendix A</i> )	[Pa]
$\zeta_n$	Modal coordinate for bending modes in <i>modal analysis</i>	[m]
$\varphi_n$	Eigenvector of eigenvalue problem in <i>modal analysis</i>	[-]
$\phi$	(Time-independent) velocity potential	[-]
$\phi_D$	(Time-independent) diffraction potential	[-]
$\phi_R$	(Time-independent) radiation potential	[-]
$\phi_W$	(Time-independent) incident wave potential	[-]
$\Phi$	Velocity potential	[-]
$\Phi_D$	Diffraction potential	[-]
$\Phi_R$	Radiation potential	[-]
$\Phi_W$	Incident wave potential	[-]
$\chi(x,t)$	Additional variable in bulge differential equation in <i>modal analysis</i>	[m]
$\psi$	(Time-independent) streamfunction	[-]
$\omega$	(Wave) frequency	[Hz]
$\boldsymbol{\omega}$	Vorticity vector	
$\omega_b$	Bulging frequency (in <i>Appendix E</i> )	[Hz]
$\omega_m$	Irregular frequency in <i>FCFM</i>	[Hz]
$\omega_n$	Natural frequency (or eigenfrequency)	[Hz]

## Latin symbols

$a$	Horizontal coordinate of point along the cross-sectional contour (in <i>FCFM</i> )	[-]
$a_{23}, a_{32}$	Coupled hydrodynamic mass coefficients between sway and heave	[kg]
$a_B$	Hydrodynamic added mass coefficient for the bending mode in 2D <i>FCFM</i>	[kg]
$a^{(m)}$	Hydrodynamic added mass coefficient for the m-th mode in 2D <i>FCFM</i>	[kg]
$a^{(m)}$	Non-dimensional hydrodynamic added mass coefficient for the m-th mode in 2D <i>FCFM</i>	[-]
[A]	Matrix with influence coefficients (in <i>Appendix C and D</i> )	[-]
$A_1, A_2$	Constants in mode shapes of <i>modal analysis</i>	[-]
$A^{(m)}$	Amplitude of forced oscillation in <i>FCFM</i>	[m]
$A_m(x, \omega)$	Added mass defined by [8] (in <i>Appendix E</i> )	[kg]
$A_{nm}$	Three-dimensional added mass matrix for bending in <i>modal analysis</i>	[kg]
$A_{nm}^*$	Three-dimensional added mass matrix for bulging in <i>modal analysis</i>	[kg]
$b$	Vertical coordinate of point along the cross-sectional contour (in <i>FCFM</i> )	[-]
$b_{23}, b_{32}$	Coupled fluid damping coefficients between sway and heave	[kg/s]
$b_B$	Hydrodynamic fluid damping coefficient for the bending mode in 2D <i>FCFM</i>	[kg/s]
$b^{(m)}$	Hydrodynamic fluid damping coefficient for the m-th mode in 2D <i>FCFM</i>	[kg/s]
$b^{(m)}$	Non-dimensional hydrodynamic fluid damping coefficient for the m-th mode in 2D <i>FCFM</i>	[kg/s]
$B$	Width of the cross-section (in <i>FCFM</i> )	[m]
{B}	Columnvector in <i>FCFM</i> , corresponding to the panel's force velocity	[m/s]
$B_1, B_2$	Constants in mode shapes of <i>modal analysis</i>	[-]
$B_a$	Pressure amplitude along bulge tube (in <i>Appendix B</i> )	[m]
$B_e$	Equivalent beam (in <i>Appendix D</i> )	[m]
$B_m(x, \omega)$	Fluid damping defined by [8] (in <i>Appendix E</i> )	[kg]
$B_{nm}$	Three-dimensional fluid damping matrix for bending in <i>modal analysis</i>	[kg/s]
$B_{nm}^*$	Three-dimensional fluid damping matrix for bulging in <i>modal analysis</i>	[kg/s]
$B_{PTO}$	Damping of the PTO	[Pa·s]
$B_r$	Viscous damping coefficient	[Pa·s]
$c$	Complex coordinate of panel in <i>FCFM</i>	[-]
$c$	Wave speed (mentioned in <i>Appendix E</i> )	[m/s]
$c$	Frequency related parameter for bulging in <i>modal analysis (Appendix F)</i>	[-]
$\bar{c}$	Complex conjugate of $c$	[-]
$c_{ij}$	Stiffness matrix (in <i>Appendix A</i> )	[N/m]
$c_n(t)$	Time-dependent bulging amplitude (in <i>modal analysis</i> )	[m]
$\dot{c}_n(t)$	Deformation velocity of bulging (in <i>Appendix E</i> )	[m/s]
$\ddot{c}_n(t)$	Deformation acceleration of bulging (in <i>Appendix E</i> )	[m/s <sup>2</sup> ]
$C_0$	Submerged (initial) cylindrical contour	[m]
$C_1 - C_4$	Constants in mode shapes of <i>modal analysis</i>	[-]
$C_n$	Normalisation constant of mode shapes in <i>modal analysis</i>	[-]
$C_s$	Additional irregular frequency variable (in <i>Section D.3</i> )	[-]
$d$	Depth of submergence in <i>FCFM</i>	[m]
$d\eta$	Wave amplitude decrease over length (in <i>Appendix B</i> )	[m]
$dC$	Integration constant over cylindrical contour	[m]
$D$	Distensibility of a deformable body	[Pa]
$D$	Diameter of the tube's cross-section	[m]
$D_j$	Divergence of shape function as defined by [53]	
$E$	Young's modulus	[Pa]
$F(z)$	Complex potential	[-]
$F_{FK}$	Froude-Krilov force	[N]
$F_{FK,m}^*$	Froude-Krilov force for the m-th bulging mode	[N]
$F_{FK,n}$	Froude-Krilov force for the n-th bending mode	[N]
$F_{i,s}$	Mooring pretension	[N]
$F_{rad,D}^{(m)}$	Damping force due to radiation (in <i>modal analysis</i> )	[N]
$F_R^{(m)}$	Radiation force for the m-th mode	[N]

$F_{wa}$	Wave force amplitude	[N]
$g$	Gravitational constant	[m/s <sup>2</sup> ]
$G(z,c)$	Green's function	[-]
$G_0(z,\zeta)$	Green's function for low frequencies in <i>FCFM</i>	[-]
$G_\infty(z,\zeta)$	Green's function for very high frequencies in <i>FCFM</i>	[-]
$h$	Wall thickness of tube	[m]
$h$	Depth of the fluid domain	[m]
$h_s$	Static wall thickness of tube	[m]
$h_e$	Equivalent draft (in <i>Appendix D</i> )	[m]
$H$	Wave height	[m]
$i$	Complex unit	[-]
$i$	Iteration index (as a subscript in <i>modal analysis</i> )	[-]
$I$	Area moment of inertia	[m <sup>4</sup> ]
$I_n$	$n$ -th diagonal value of the identity matrix $\mathbf{I}$	[-]
$j$	Complex unit	[-]
$J_W(\omega)$	Mean wave energy per unit wavecrest	[W/m]
$k$	Additional irregular frequency variable (in <i>Section D.3</i> )	[-]
$k$	Integration variable in Principal Value integral	[-]
$k_n$	Frequency related parameter in <i>modal analysis</i>	[-]
$K_0$	Constant in the low frequency range of the <i>FCFM</i>	[-]
$K_\infty$	Constant in the very high frequency range of the <i>FCFM</i>	[-]
$K_m$	Mooring stiffness coefficient (in <i>Appendix E</i> )	[N/m]
$K_n$	Frequency related parameter for bending in <i>modal analysis</i>	[-]
$K_{nm}$	Structural stiffness matrix in <i>modal analysis</i>	[N/m]
$L$	Length of the tube	[m]
$m$	Mode of oscillation	[-]
$m$	(Continuous distribution of) mass in <i>modal analysis</i>	[kg]
$m$	Index for the $m$ -th irregular frequency (in <i>Section D.3</i> )	[-]
$m_{tube}$	Mass of the tube without inner fluid	[kg]
$M$	Mass	[kg]
$M_{bend}$	Bending moment	[Nm]
$M^{(m)}$	Added mass force in <i>FCFM</i>	[N]
$M_{nm}$	Structural mass matrix in <i>modal analysis</i>	[kg]
$M_{towhead}$	Mass of S3 towheads (in <i>Appendix E</i> )	[kg]
$n$	Index for the $n$ -th branch (in <i>Section D.5</i> )	[-]
$\vec{n}$	Unit normal vector	[-]
$n_i$	Directional cosine on $i$ -th panel	[-]
$n^{(m)}$	Normal of $m$ -th motion in <i>FCFM</i>	[-]
$N^{(m)}$	Fluid damping force in <i>FCFM</i>	[N]
$N_{mode}$	Number of modes observed in the <i>modal analysis</i>	[-]
$N_{elem}$	Number of elements along the contour (in <i>Appendix C and D</i> )	[-]
$p(x,t)$	Pressure	[Pa]
$\bar{p}_{0i}$	Pressure due to incoming wave (in <i>Appendix E</i> )	[Pa]
$\bar{p}_{7i}$	Pressure due to diffracted wave (in <i>Appendix E</i> )	[Pa]
$p_e$	(Dynamic) external pressure	[Pa]
$p_e^*$	External pressure (in <i>Appendix E</i> )	[Pa]
$\bar{p}_e$	Contour averaged external pressure	[Pa·m]
$p_{ex}$	Excitation pressure	[Pa]
$\bar{p}_{ex}$	Contour averaged excitation pressure	[Pa·m]
$p_i$	Internal pressure	[Pa]
$p_{i,s}$	Static internal pressure	[N]
$p_n$	Normal component of the pressure inside the tube (in <i>Appendix A</i> )	[Pa]
$p_{r,b}$	Radiation pressure due to bulging	[Pa]
$p_{r,rb}$	Radiation pressure due to bending	[Pa]
$p_R^{(m)}$	Radiation pressure for the $m$ -th mode	[Pa]
$\bar{p}_R$	Contour averaged radiation load	[N·m]

$p_{rad}$	Radiation pressure	[N/m]
$p_{R,i}^{(m)}$	Radiation pressure on the $i$ -th element for the $m$ -th mode	[Pa]
$p_t$	Frictional pressure component (in <i>Appendix A</i> )	[Pa]
$\bar{P}$	Mean absorbed power over one wave period	[W]
$P_b$	Power absorbed in wave energy device	
$P_{wec}(\omega)$	Absorbed power by the WEC	[W]
$p_W$	Pressure along the tube's wall due to the incident wave	[Pa]
$\bar{p}_W$	Contour averaged wave (or Froude-Krilov) load	[N/m]
$q_n(t)$	Time-dependent bending amplitude (in <i>modal analysis</i> )	[m]
$\dot{q}_n(t)$	Time-dependent bending velocity (in <i>modal analysis</i> )	[m]
$\ddot{q}_n(t)$	Time-dependent bending acceleration (in <i>modal analysis</i> )	[m]
$Q_j$	(Array of) complex source strength	[-]
$r$	Distance in a polar, cylindrical and spherical coordinate system	[m]
$r_{in}$	Inner tube diameter	[m]
$r_{out}$	Outer tube diameter	[m]
$R$	Radius of cylinder	[m]
$R_s$	Static radius of the cylinder	[m]
$S_0$	Initial cross-sectional area	[m <sup>2</sup> ]
$S_j$	Modal displacement as defined by [53]	
$S$	Cross-sectional area	[m <sup>2</sup> ]
$S_\delta$	Deformed surface (as defined <i>Appendix A</i> )	[m <sup>2</sup> ]
$ s_i $	Length of $i$ -th element along the contour	[m]
$S_s$	Static cross sectional area	[m <sup>2</sup> ]
$t$	Time	[s]
$T$	Tension in the tube wall (as defined in <i>Appendix A</i> )	[N]
$T$	Draft of cross-section (in <i>FCFM</i> )	[m]
$T(t)$	Time-dependent function of mode shapes in <i>modal analysis</i>	[-]
$T_S$	Longitudinal tension in the bulge WEC in <i>modal analysis</i>	[N]
$u$	Velocity (in x-direction)	[m/s]
$u_d$	Deformation velocity in <i>modal analysis</i>	[m/s]
$u_z$	Velocity component in longitudinal direction of the tube	[m/s]
$U$	Generalised inner fluid velocity (according to [8])	[m/s]
$U$	Elastic strain energy	[J]
$U^{(m)}$	Deformation velocity (in <i>modal analysis</i> )	[m/s]
$v$	Velocity (in y-direction)	[m/s]
$v_n$	Velocity of the structure in the normal direction	[m/s]
$V_{shear}$	Shear force in <i>modal analysis</i>	[N]
$w(x, t)$	Deflection of the bending WEC (in <i>modal analysis</i> )	[m]
$w$	Velocity (in z-direction)	[m/s]
$W(z)$	Complex velocity	[m/s]
$W_n(x)$	Mode shape for bending mode $n$ in <i>modal analysis</i>	[-]
$W_m(x)$	Mode shape for bending mode $m$ in <i>modal analysis</i>	[-]
$x$	Longitudinal coordinate (in <i>Modal analysis</i> )	[m]
$X_n(x)$	Mode shape for bulging mode $n$ in <i>modal analysis</i>	[-]
$\tilde{X}$	Modal coordinate for bulging modes in <i>modal analysis</i>	[m]
$z$	Complex coordinate	[-]
	Vertical coordinate (in <i>Modal analysis</i> )	[m]

### Mathematical definitions

*	Refers to the mathematical operation of Equation F.64	
$E_1$	Exponential integral	
$i$	Imaginary unit (with respect to space in <i>Appendix C and D</i> )	$i = \sqrt{-1}$
$j$	Imaginary unit (with respect to time in <i>Appendix C and D</i> )	$j = \sqrt{-1}$
$\nabla$	Nabla operator	$\nabla = \left( \frac{\partial}{\partial x_1}, \frac{\partial}{\partial x_2}, \dots, \frac{\partial}{\partial x_n} \right)$
$\partial$	Partial derivative symbol	

$PV \int_0^{\infty} f(x) dx$	Principal Value integral of <i>function</i> $f(x)$
$T$	Transpose of a matrix

## Subscript

0	Refers to an initial condition or time $t = 0$ s
$\delta$	Refers to deformations
$\theta$	In direction of the angular coordinate
a	Refers to amplitude (in $\zeta_a$ )
b	Refers to the bulge or bulging motion
h	Refers to hoop stress/strain (in circumferential direction)
i	An index for an element along the contour
I	Refers to imaginary unit i
ij	Matrix indices for the influence and potential coefficients
j	An index for an element along the contour
J	Refers to imaginary unit j
n	Refers to the normal direction
rs	Refers to rigid body or bending motions
s	Refers to the static conditions (in <i>Modal analysis</i> )
t	Refers to the tangential direction
W	Refers to the wave
x	Refers to the x-coordinate
y	Refers to the y-coordinate
z	Refers to the z-coordinate

## Abbreviations

2D	Two-dimensional
3D	Three-dimensional
ALE	Eulerian Lagrange method
ASAP	A Seakeeping Analysis Program [66]
BEM	Boundary Element Method
CW	Capture Width
EAP	Electro-Active Polymer
FCF	Frank Close-Fit
FCFM	Frank Close-Fit method
OWC	Oscillating Water Column
PTO	Power Take Off
RAO	Response Amplitude Operator
WEC	Wave Energy Converter



# Contents

<b>Preface</b>	<b>iii</b>
<b>List of Symbols</b>	<b>v</b>
<b>List of Figures</b>	<b>xiii</b>
<b>List of Tables</b>	<b>xv</b>
<b>1 Frank’s close-fit method included in hydro-elasticity of a bulge wave energy converter</b>	<b>1</b>
1.1 Introduction	1
1.2 Numerical model	2
1.3 Results and discussion	7
1.4 Conclusions	10
<b>Bibliography</b>	<b>11</b>
<b>A Problem definition</b>	<b>15</b>
A.1 Background and problem	15
A.2 Research questions	21
A.3 Schedule and project approach	21
<b>B Project Approach</b>	<b>23</b>
B.1 Results	23
B.2 Project steps	23
<b>C Franks Close Fit Method</b>	<b>27</b>
C.1 Assumptions and boundary conditions	27
C.2 Geometry description	28
C.3 Solving method	29
C.4 Results	35
C.5 Validation and verification	38
C.6 Conclusions	40
<b>D Description of FCF numerical model</b>	<b>41</b>
D.1 Constants and geometrical characteristics	41
D.2 Mapping of geometry	42
D.3 Irregular frequencies	44
D.4 Non-frequency parts of influence and potential coefficients	45
D.5 Frequency parts of influence and potential coefficients	47
D.6 Assembling influence and potential matrices	49
D.7 Calculate source strengths	50
D.8 Calculate pressure distribution	51
D.9 Determine hydrodynamic coefficients	52
<b>E Bulging cylinder</b>	<b>53</b>
E.1 Simple distensible cylinder	53
E.2 Fluid-filled bulging cylinder operating under waves	56
E.2.1 Literature review . . . . .	56
E.2.2 Methodology of bulging WEC . . . . .	63
E.2.3 Assumptions and boundary conditions . . . . .	64
E.3 Conclusions	66

---

<b>F</b>	<b>Modal analysis of Bulge WEC</b>	<b>67</b>
E.1	Pure bending	67
E.2	Pure bulging	74
E.3	Results	82
E.4	Validation and verification	91
E.5	Conclusions	96

# List of Figures

1.1	Configuration of bending tube including directional cosines on the cross-sectional panels. . . .	2
1.2	Configuration of bulging tube including directional cosines on the cross-sectional panels. . . .	2
1.3	2D hydrodynamic coefficients of a cylinder submerged at $d/R = 1.25$ . . . . .	7
1.4	Hydrodynamic coefficients ( $A_{nm}(\omega)$ and $B_{nm}(\omega)$ ) of first five bending modes. . . . .	7
1.5	Hydrodynamic coefficients ( $A_{nm}(\omega)$ and $B_{nm}(\omega)$ ) of first six bulging modes. . . . .	7
1.6	Added mass and radiation damping coefficients of third bulging mode as calculated by [8]. . . .	8
1.7	The first five bending mode shapes. . . . .	8
1.8	The first six bulging mode shapes. . . . .	8
1.9	Generalised wave-exciting force ( $F_{FK,n}(\omega)$ ) for the first five bending modes. . . . .	8
1.10	Excitation load for the second bulging mode defined by the adapted modal analysis model and the numerical model of [8]. . . . .	9
1.11	Bending deformation ( $w(x, \omega)$ ) at the midpoint of the beam ( $x = 5$ m). . . . .	9
1.12	Bulging deformation ( $\delta\lambda = \frac{S}{S_s} - 1$ ) at the midpoint of the beam ( $x = 0$ m). . . . .	9
1.13	WEC efficiency ( $\eta_{wec}$ ) of bending motions on left vertical axis and bulging motions on right vertical axis with $B_{PTO} = 100$ Pa·s. . . . .	10
A.1	Configuration of the hinged barges by Newman [53] . . . . .	16
A.2	Layout of the Pelamis Wave Energy Converter [5] . . . . .	16
A.3	Definition of the forces working on an element of the tube wall [47] . . . . .	19
A.4	Force and power capture widths versus wave frequency for WEC (Pelamis) [56] . . . . .	21
B.1	Deformation of tube due to a prescribed sinusoidal strain ( $\varepsilon_h(t)$ ). . . . .	24
C.1	Geometry descriptions as defined by Frank [26] . . . . .	29
C.2	Continuous source distribution discretised into a single source strength for an element. . . . .	30
C.3	Definition of the surface source element and its reflected element (based on [30]). . . . .	31
C.4	Hydrodynamic coefficients of floating cylinder compared with analytical values found by Liu et al. [46] and experimental values obtained by Vugts [68]. . . . .	35
C.5	Hydrodynamic coefficients of floating barge compared with experimental values obtained by Vugts [68]. . . . .	36
C.6	Geometry (C.6a) and hydrodynamic coefficients (C.6b) for heave of a submerged cylinder ( $d/R = 1.25$ ) compared with first order theory results obtained by Ogilvie [26]. . . . .	37
C.7	Hydrodynamic coefficients of a submerged cylinder at $d/R = 1.5$ compared with analytical values found by Liu et al. [46]. . . . .	37
C.8	ASAP Results and Vugts' experiments for Added Mass and Fluid Damping coefficient of swaying cylinder section [66]. . . . .	38
C.9	Hydrodynamic added mass and fluid damping of a submerged circular cylinder at different submersion depths, where $d$ is the submersion depth and $R$ the tube's radius [49]. . . . .	39
D.1	Example of asymmetric and symmetrical bodies. . . . .	42
D.2	Geometry characteristics for image segments. . . . .	43
D.3	Panels and their midpoints for a circular cylinder with $NE = 18$ . . . . .	43
D.4	Example of a multi-valued logarithm with multiple branches and a single-valued logarithm with a principal branch along the negative x-axis [71]. . . . .	46
E.1	Coordinate transformation between FCFM (of <i>Appendix C and D</i> ) and bulging motion in 3D (for <i>Appendix E and F</i> ) . . . . .	53
E.2	Directional cosines for E.2a sway, E.2b heave and E.2c bulging. . . . .	54
E.3	Hydrodynamic coefficients of a cylinder submerged at $d/R = 1.25$ for heave, sway and bulge. . .	55

E.4	Hydrodynamic coefficients of a cylinder submerged at $d/R = 1.25$ for heave, sway and bulge. . .	55
E.5	Experimental setup used by Chaplin et al. for the Anaconda WEC [14]. . . . .	57
E.6	Wave energy converter S3 submerged in waves [7, 8] . . . . .	58
E.7	First six eigenmodes of a tube of $L = 10$ m, $r_s = 0.274$ m, $h_s = 0.01$ m and submergence $z_s = -0.265$ m as found by Babarit et al. [8]. . . . .	62
F.1	Scheme of the iteration procedure and its coupling to the FCFM for the bending model. The value for the convergence test is set to $\varepsilon = 1 \cdot 10^{-12}$ . (Adapted from <i>Loukogeorgaki et al., Fig. 4</i> [48]) . . . . .	72
F.2	First 5 normalized 'wet' eigenmodes of bending mode. . . . .	73
F.3	Mode shapes of the first six eigenmodes. . . . .	77
F.4	Dry mode shapes and derivatives of the bulging mode shapes. . . . .	78
F.5	Characteristic equations of set 1 (Equation F.51) and set 2 (Equation F.52) including the numerical eigenfrequencies (given by red crosses). . . . .	79
F.6	Dry mode shapes and derivatives of the mode shapes without the 'numerical eigenfrequencies' of bulging. . . . .	79
F.7	Hydrodynamic coefficients for the first 5 bending mode shapes. . . . .	83
F.8	Excitation pressure for the first 5 bending mode shapes. . . . .	84
F.9	Modal coordinates for the first 5 bending mode shapes. . . . .	84
F.10	Deformation of the tube at 10 positions along the tube. . . . .	85
F.11	First 6 mode shapes of the bulging tube. . . . .	86
F.12	Hydrodynamic coefficients for the first 6 bulging mode shapes. . . . .	86
F.13	Excitation pressure for the first 6 bulging mode shapes. . . . .	87
F.14	Modal coordinates for the first 6 bulging mode shapes. . . . .	87
F.15	Deformation of the tube at 10 positions along the tube for bulging. The blue line represents the FCFM results, the green are the numerical results of Babarit et al. and the red dots represent the experimental values found by Babarit et al. [8]. . . . .	88
F.16	Mode shapes of a bending tube. . . . .	89
F.17	WEC efficiency calculated by Equation F.74 in subfigure F.17a and validation of bulging WEC efficiency of [8] in subfigure F.17a . . . . .	90
F.18	WEC efficiency based on Equation F.78. . . . .	91
F.19	Hydrodynamic coefficients of first bulging mode against wave period. . . . .	92
F.20	Exciting forces of a bulging tube, where the first mode is represented by the solid curves and the second with the dashed curves in F.20a. . . . .	92
F.21	Exciting forces of a bulging tube. . . . .	93
F.22	Mode shapes of a bending tube. . . . .	94
F.23	Exciting forces of a bending tube. . . . .	95
F.24	Mode shapes and exciting forces of a bending tube (with length scale $L/2$ ). . . . .	95
F.25	Regions of importance of viscous and diffraction forces on the structure. Figure adapted from [45]. . . . .	96

# List of Tables

1.1	Values of $k_n, \omega_n^{dry}, \omega_n^{wet}$ for the first five bending modes. . . . .	4
1.2	Values of $k_n, K_n, \omega_n^{dry}, \omega_n^{wet}$ for the first 6 bulging modes. . . . .	6
C.1	Forced oscillation and forced velocity components in two different methods of analysis. . . . .	32
C.2	Non-dimensional definitions of Vugts [69], Frank [26] and Van 't Veer [66] for circular and rectangular cross sections. . . . .	34
D.1	Principal data of tested cylinder and barge . . . . .	41
D.2	Non-frequency components of kinematic boundary condition (CB) in numerical model. . . . .	45
D.3	Non-frequency components of velocity potential (CU) in numerical model. . . . .	47
D.4	Frequency-depending components of kinematic boundary condition (CB) in numerical model. . . . .	47
D.5	Frequency-depending components of velocity potential (CU) in numerical model. . . . .	49
E.1	Boundary value problems for the diffracted and radiated wave problem in linear potential theory [8]. . . . .	60
F.1	'Dry' and 'wet' eigenfrequencies of the 5 bending modes of a bulge WEC with dimension given in Table E2. . . . .	73
F.2	Geometry and material properties for numerical calculations on elastic-hydrodynamic motions [8]. . . . .	80
F.3	Check for conservation of mass of first six mode shapes for 100 panels along the tube's length. . . . .	80
F.4	'Dry' and 'wet' eigenfrequencies of the bulging modes of a bulge WEC with dimension given in Table E2. . . . .	81



# Frank's close-fit method included in hydro-elasticity of a bulge wave energy converter

Hydro-elasticity is important in the evaluation of a category of wave energy converters (WEC). In this paper, the hydro-elastic response of a bulge wave energy converter is examined by the implementation of a two-dimensional potential theory. The numerical implementation of the Frank Close-Fit method (FCFM) defines hydrodynamic coefficients and incident wave loads, where computation time is reduced with respect to the three-dimensional boundary element methods (BEM). These coefficients are included by a two-way coupling in the equation of motion for bending and bulging, which defines the interaction between incident waves, radiated waves and wall deformations. The results are compared to analytical and numerical methods and this analysis reveals that the addition of the FCFM to a modal analysis is valid to use for hydro-elastic problems in bulge wave energy converters.

Keywords: *bulge wave energy converter, hydro-elasticity, potential flow & Frank close-fit method*

## Introduction

Wave energy is a source of energy which is of large interest [11]. Different types of wave energy converters are elaborated by Wolgamot and Fitzgerald and these are divided into three types [72]:

- Wave overtopping devices.
- Oscillating Water Column (OCW) devices.
- Wave-activated devices.

It has been shown by Newman in 1994 [53] that the hydro-elasticity is the primary factor for wave-activated devices. Different types of wave energy converters (WECs) are examined, where hydro-elastic deformations are included in the equation of motion.

This study describes the implementation of a new method to calculate the hydro-elastic response of a bulge wave energy converter (WEC). The aim of this study is to investigate whether the implementation of the Frank close-fit method (FCFM) is valid to obtain radiation forces for a deformable body with significant reduced computation effort. The hydrodynamic results of the two-dimensional potential method will be related to the hydro-elasticity based on two-way coupling methods which would result in valid predictions of the hydro-elastic response of the WEC. This study includes the bending modes of a bulge WEC, since it is assumed that these bending modes are important in the hydro-elastic analysis.

A number of authors have considered a bulge wave energy converter to extract energy from incoming waves [12–14, 21–23]. This distensible wave-energy converter is a long elastic tube filled with water. The tube is positioned in head waves where the inner fluid experiences a bulge wave (pressure wave) traveling in along the tube. [23] developed a mathematical theory based on experiments to un-

derstand the process of a bulge wave energy converter. [6] stated that Farley et al. neglected the radiation and diffraction contributions to the hydrodynamic forces on the bulge WEC. A three-dimensional adapted BEM is used to define the pressures on the tube on several positions along the tube. A three-dimensional numerical model is presented to deal with the bulge modes of an elastic wave energy converter, where simplified Navier-Stokes equations are expressed in the bulge wave equation. This numerical model investigated the non-linear hydrodynamic response of the bulge WEC, including inner fluid damping and viscous damping of the elastic wall. The coupling between radiation loads and the elastic deformation is related by one-way coupling, where the final deformation of the tube is compared to experiments.

Up to now, several studies reported the bulge wave response by analytical, numerical and experimental results. These studies neglected the bending response due to incident gravity waves [8, 60].

For this study, elastic deformations of a bulge WEC includes a two-way coupling of the fluid and the structure, since natural frequencies of the structural deformations are in the same frequency range as the first order wave loads [53]. The WEC is modelled in a fluid domain which is assumed to be incompressible, irrotational and inviscid, and the tube floats directly under the free surface. Since the tube is slender and is situated along the wave crests, diffraction effects will be neglected, since the end effects are assumed to be small. Therefore, the incident gravity wave is driving the bending and bulging deformations of the tube. Unlike the numerical model of Babarit [8], the non-linear terms are not considered in this study.

Radiation effects due to the presence of the tube in the waves, will be calculated by a numerical method founded by Frank in 1967 [26]. The theory

of Frank is a strong tool to calculate the added mass and fluid damping for any arbitrary floating or submerged cross-sectional shape for heave, sway and roll. In this article the theory of Frank is adapted to model bulging deformations of a submerged circular cross-section and is used to find the hydro-elastic response of the bending and bulging mode shapes of a bulge WEC. The theory of Frank is modelled in a numerical model, which will be evaluated in *a. Frank Close Fit Method*. The remaining part of the Section *Numerical model* contains the modal analysis of the bending and bulging deformations, resulting in the deformation of the tube due to incident waves. The Section *Results and discussion* analyses the results of this numerical model, where the results are verified by existing methods. The fourth section (*Conclusions*) presents the conclusions of this paper.

## Numerical model

Before explaining the hydro-elasticity of the bulge WEC by a modal analysis (Subsection b.), it is necessary to specify the implementation of the Frank Close-Fit method for bending and bulging deformations (Subsection a.). The FCFM is supplied by a function, where this linear numerical method assumes incompressible, inviscid and irrotational flow. The resulting panel method is a strong and fast tool to calculate the hydrodynamic terms of the equation of motion. The equation of motion is defined by a modal expansion of the bending and bulging modes, which is a simplified method to define deformations with little or no damping, where deformations are assumed to be small. In both sections, specific notes are added to indicate modelling difference between bending and bulging deformations.

### a. Frank Close Fit Method

The Frank Close-Fit method requires a panel distribution along the cross-sectional contour. On each straight-line element a distribution of sources or sinks is smeared out. The elementary flow elements are assumed to have a constant source strength density along each individual segment. The source strength will contribute to the fluid velocity and hydrodynamic pressure on each contour segment in its panels midpoint. Therefore, the value of the source strength in a midpoint is of main interest in this method to find the hydrodynamic coefficients.

To solve the source strengths along the cross-sectional panels, a harmonic oscillation of unit amplitude is applied to the cross-section. The kinematic boundary on the contour provides the fluid velocity on each panel due to the oscillation of the body. The normal to the panel pointing into the fluid is used to define the directional cosine of the mode of oscil-

ation. For bending, the heave motion is observed, since the cross-section is only translated in the vertical direction. The bending and heave motion will be denoted by the subscript  $m = 3$ . The configuration of a bending tube is shown in Figure 1.1, where the orange arrows are representing the directional cosines of the bending oscillation in the lower right figure. For bending, the motion is denoted by  $m = 4$  in the governing equations.

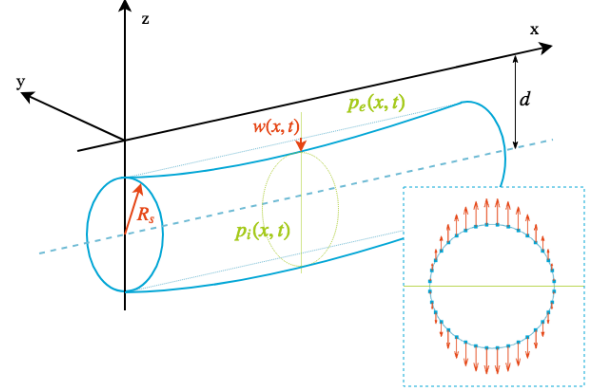


Figure 1.1: Configuration of bending tube including directional cosines on the cross-sectional panels.

For bulging the panels velocity is in the normal direction, which is indicated by the directional cosine of bulging, which is shown in Figure 1.2.

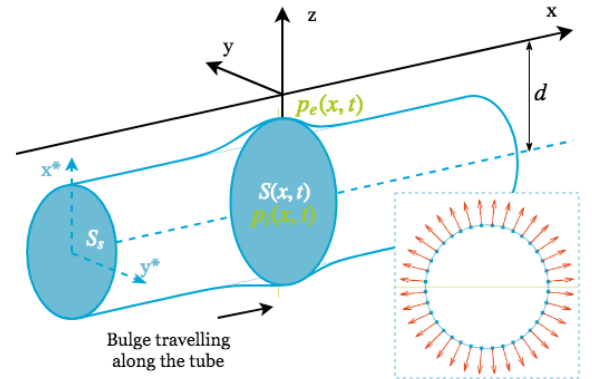


Figure 1.2: Configuration of bulging tube including directional cosines on the cross-sectional panels.

On each panel the kinematic boundary condition is solved for motion ( $m$ ), where:

$$\begin{aligned} \vec{n} \cdot \nabla \Phi &= \text{Re}_I \left\{ \sum_{j=1}^N Q_j (\vec{n} \cdot \nabla) \int_{C_0} G(z, c) dC \cdot e^{-j\omega t} \right\} \\ &= v_n \end{aligned} \quad (1.1)$$

where  $Q_j$  denotes the source strength and  $G(z, c)$  is the Green's function for a pulsating source in position  $z$  towards panel's coordinate  $c$ . Both, the source strength distribution and Green's function are time-complex quantities, where the Green's function definition is based on the work of Wehausen and Latoine

[70]:

$$G(z, c) = \frac{1}{2\pi} \left[ \log(z - c) - \log(z - \bar{c}) + 2PV \int_0^\infty \frac{e^{-ik(z-\bar{c})}}{v - k} dk \right] - j \cdot e^{-iv(z-\bar{c})} \quad (1.2)$$

where  $\bar{c}$  is the complex conjugate of complex coordinate  $c$  and  $v$  is the wavenumber given by  $v = \omega^2/g$ . The contribution of each panel is calculated by Equation 1.1 and 1.2 and is assigned to a matrix where the influence between the elements is defined. This rectangular matrix's size depends on the number of elements along the contour and consist of time-complex values. This influence matrix multiplied with the array of time-complex source strengths gives the time-complex oscillating velocity at the right-hand side and represents the matrix formulation of Equation 1.1. The velocity on the  $i$ -th panel is defined as:

$$v_{n,i} = -j \cdot A^{(m)} \cdot \omega \cdot n_i^{(m)} \quad (1.3)$$

where  $j$  is denotes the complex unit in the time-complex domain.  $A^{(m)} = 1$  is the unit amplitude for the  $m$ -th mode ( $m = 3$  for bending and  $m = 4$  for bulging),  $\omega$  refers to the oscillation frequency and  $n_i^{(m)}$  is the direction cosine of the  $m$ -th mode. The bulging mode ( $m = 4$ ) consists of both sway ( $m = 2$ ) and heave ( $m = 3$ ) motions, which will be coupled in a later stage of the model.

### Velocity potential

Solving the matrix equation results in the complex source strengths on each panel. These source strengths ( $Q(c)$ ) are combined with the Green's function  $G(z, c)$  to describe the velocity potential on every panel:

$$\phi(z) = \text{Re}_I \left\{ \sum_{j=1}^N \int_{C_0} Q(c) G(z, c) dC \right\} \quad (1.4)$$

where velocity potential is complex in time and the subscript 'I' refers to the space-complexity of the Green's function, which is denoted by the complex unit 'i'. The contribution of each element to the potential is also calculated by a matrix equation, where the components of the rectangular matrix are the time-complex parts of the Green's function integrated over the element. The time-independent velocity potential  $\phi(z)$  is the result of a combination of the source strengths and the potential coefficient matrix. The radiation pressure  $p_R^{(m)}$ , is then related to the (time-independent) radiation potential  $\phi_R$  for the  $m$ -th motion on position  $z$ :

$$p_R^{(m)}(z, \omega) = -\rho \cdot \frac{\partial \Phi_R}{\partial t} = \rho \cdot j \cdot \omega \cdot \phi_R(z) \quad (1.5)$$

The pressure is found for every position along the tube's contour. The radiation pressure is defined based on symmetry characteristics of either vertical (sway) or horizontal movements (heave), where the vertical movement will describe the cross-sectional oscillation of bending. For bulging, the radiations are in both directions, and the resulting pressure distributions is a vector summation of both motions of oscillations. This is the major difference between the bending and bulging oscillation modes. The total radiation force,  $F_R^{(m)}$  is defined by the radiation pressure which will be integrated over the submerged contour  $C_0$  in the direction of the applied oscillation (denoted by  $m$ ).

$$F_R^{(m)}(\omega) = - \int_{C_0} p_R^{(m)}(z, \omega) \cdot \bar{n} dC = - \sum_{i=1}^{N_{elem}} p_{R,i}^{(m)}(z_i, \omega) \cdot n_i^{(m)} \cdot |s_i| \quad (1.6)$$

The subscript  $i$  in this equation denote the  $i$ -th panel, where  $|s_i|$  is the panel length along the submerged contour. The total number of elements along the contour is denoted by  $N_{elem}$ . The radiation force contains of two terms; one in phase with the velocity of the forced cross-section body ( $\dot{\Theta}^{(m)}$ ) and the other in phase with the acceleration of the body ( $\ddot{\Theta}^{(m)}$ ). These terms are related to the forced oscillation of the cylinder described by  $\Theta^{(m)} = A^{(m)} \cdot e^{-j\omega t}$  where  $A^{(m)}$  is the amplitude of oscillation of the  $m$ -th mode. Both terms are influenced by frequency-dependent coefficients, which are known as the hydrodynamic added mass  $a^{(m)}$  and fluid damping coefficients ( $b^{(m)}$ ):

$$F_R^{(m)}(\omega) = -a^{(m)} \cdot \ddot{\Theta}^{(m)} - b^{(m)} \cdot \dot{\Theta}^{(m)} = a^{(m)} \cdot \omega^2 \cdot A^{(m)} \cdot e^{-j\omega t} + b^{(m)} \cdot j \cdot \omega \cdot A^{(m)} \cdot e^{-j\omega t} \quad (1.7)$$

As a result of Equation 1.2 and Equations 1.5 to 1.7 the hydrodynamic coefficients are found by a summation over the contour panels,

$$a^{(m)} = -\frac{\rho \cdot \omega}{\omega^2 \cdot A^{(m)}} \cdot \sum_{i=1}^N \text{Re}_J \left\{ p_{R,i}^{(m)} \right\} \cdot n_i^{(m)} \cdot |s_i|$$

$$b^{(m)} = \frac{\rho \cdot \omega}{\omega \cdot A^{(m)}} \cdot \sum_{i=1}^N \text{Im}_J \left\{ p_{R,i}^{(m)} \right\} \cdot n_i^{(m)} \cdot |s_i| \quad (1.8)$$

To compare hydrodynamic coefficients for various cross-sectional dimensions (cross-sectional area  $S_S$ ), the hydrodynamic coefficients are non-dimensionalised in line with the results of Frank [26],

$$a'_{(m)} = \frac{a^{(m)}}{\rho S_S} \quad b'_{(m)} = \frac{b^{(m)}}{\rho S_S \omega} \quad (1.9)$$

These non-dimensional coefficients are widely used and can be scaled for different cylinder radii. A more detailed description of the Frank Close-Fit method is

revealed in Appendix C and several parts of the numerical implementation are attached in Appendix D.

### Incident wave pressure

The elements along the cross-sectional contour are also used to define the cross-sectional averaged incident wave pressures. The incident wave potential  $\Phi_W$  for in deep water with wave amplitude  $\zeta_a$  is [41, 69]:

$$\Phi_W(x, z, \omega) = \frac{\zeta_a g}{\omega} e^{vz} \cdot e^{ivx} \cdot e^{-i\omega t} \quad (1.10)$$

The incident wave load is integrated over the submerged contour of the three-dimensional tube, by a multiplication of the pressure distribution and directional cosines along the contour of the body. The contour averaged part of this Froude-Krilov load is defined as [8, 69]:

$$\bar{p}_W(x, \omega) = i\rho g \zeta_a \cdot e^{ikx} \cdot e^{-i\omega t} \cdot \int_{C_0} e^{kz} \cdot ndC \quad (1.11)$$

The incident wave pressure varies along the length of the tube, where it causes deformations due to the hydro-elasticity.

## b. Modal analysis

The response of the tube due to incident waves is defined for both bending and bulging modes.

### Bending modes

The modal response of bending is applied under the assumptions of the Euler-Bernoulli beam theory [35]. The differential equation of a slender (cylindrical) beam surrounded by fluid is described by [35, 53, 55],

$$m \frac{\partial^2 w(x, t)}{\partial t^2} + EI \frac{\partial^4 w(x, t)}{\partial x^4} = p(x, t) \quad (1.12)$$

where the deformation  $w(x, t)$  is demonstrated in Figure 1.1. The deflection of the beam  $w(x, t)$  is estimated to be [35, 55]:

$$w(x, t) = \sum_{n=1}^{\infty} W_n(x) q_n(t) \quad (1.13)$$

which is a linear superposition of mode shapes ( $W_n(x)$ ) and a constant which will be defined by initial conditions ( $q_n(t)$ ).

In accordance with Equation 1.12, bending of the tube depends on the continuous distribution of mass  $m$ , the Young's modulus  $E$  and the area moment of inertia  $I$  which is defined by the cross-sectional dimensions.

The mode shapes of the free-free beam are defined by two boundary conditions at both ends; the shear force and bending moment at the bow and stern are equal to zero. These boundary conditions

result in  $N_{mode}$  normal mode shapes (which depends on  $x$ ):

$$W_n(x) = \sin k_n x + \sinh k_n x + \alpha_n \cdot (\cos k_n x + \cosh k_n x) \\ \text{with } \alpha_n = \left( \frac{\sin k_n L - \sinh k_n L}{\cosh k_n L - \cos k_n L} \right) \\ \text{for } n = 1, 2, \dots, N_{mode} \quad (1.14)$$

The values of  $k_n$  are found by the characteristic equation:

$$\cos k_n L \cosh k_n L = 1 \quad (1.15)$$

and  $k_n$  is related to the 'dry' natural frequency by  $k_n^4 = \frac{m\omega_n^2}{EI}$ . The values of the  $k_n$  and  $\omega_n$  are given in Table 1.1 for a tube of 10 m length, a radius of 0.274 m, 0.01 m wall thickness and a Young's modulus of  $0.0020 \cdot 10^9$  Pa.

Mode	$k_n$	$\omega_n^{dry}$	$\omega_n^{wet}$
1	0.473	0.522	0.453
2	0.785	1.440	1.230
3	1.10	2.823	2.351
4	1.41	4.667	4.372
5	1.73	6.971	6.755

Table 1.1: Values of  $k_n$ ,  $\omega_n^{dry}$ ,  $\omega_n^{wet}$  for the first five bending modes.

The orthogonality properties of the mode shapes and the definition of  $k_n$  define the equation of motion by the implementation of Equation 1.13 into 1.12:

$$m \sum_{n=1}^{\infty} W_n(x) \frac{\partial^2 q_n(t)}{\partial t^2} + EI \sum_{n=1}^{\infty} k_n^4 W_n(x) q_n(t) = p(x, t) \\ m \sum_{n=1}^{\infty} \int_L W_n \frac{\partial^2 q_n(t)}{\partial t^2} W_m dx \\ + EI \sum_{n=1}^{\infty} \int_L \left( \frac{m\omega_n^2}{EI} \right) W_n(x) q_n(t) W_m(x) dx = \Gamma_n \\ \ddot{q}_n(t) + \omega_n^2 q_n(t) = \frac{\Gamma_n}{m} \quad (1.16)$$

where  $\Gamma_n$  is the generalized force, defined as [35, 55],

$$\Gamma_n = \int_L p(x, t) \cdot W_n(x) dx \\ = \int_L \bar{p}_W(x, t) \cdot W_n(x) dx - A_{nm} \cdot \ddot{q}_n - B_{nm} \cdot \dot{q}_n \quad (1.17)$$

The hydrodynamic coefficients are added to the right-hand side of Equation 1.16, where  $A_{nm}$  and  $B_{nm}$  are the matrices containing added mass and fluid damping coefficients. Since these coefficients are frequency-dependent, the values of these matrices depend on the 'wet' natural frequency. This 'wet' natural frequency is defined by a neglected incident wave pressure. Assuming zero fluid damping gives the following reduced equation of motion:

$$(M_{nm} + A_{nm}(\omega_n^{wet})) \ddot{q}_n + K_{nm} q_n = 0 \quad (1.18)$$

where the structural mass matrix  $M_{nm}$  exists of the mass of the structure and the structural stiffness matrix  $K_{nm}$  is defined by  $EI \cdot k_n^4$ . The value of  $A_{nm}$  is defined by an iterative process, where the 'wet' frequency converges towards a final value of the 'wet' natural frequency. During each iteration step the added mass and damping matrices are defined by:

$$\begin{aligned} A_{nm}(\omega_n^{wet}) &= \int_{x=0}^L a^{(3)}(\omega_n^{wet}) \cdot W_n \cdot dx \\ B_{nm}(\omega_n^{wet}) &= \int_{x=0}^L b^{(3)}(\omega_n^{wet}) \cdot W_n \cdot dx \end{aligned} \quad (1.19)$$

The eigenfrequencies are found by a rearrangement of the matrices for each iteration step [48]:

$$\begin{aligned} [-\omega^2(M_{nm} + A_{nm}) + K_{nm}] \zeta_n \cdot e^{-i\omega t} &= 0 \\ \rightarrow (\omega_n^{wet})^2 &= \frac{K_{nm}}{M_{nm} + A_{nm}} = \frac{EI \cdot k_n^4}{m + A_{nm}(\omega_n^{wet})} \end{aligned} \quad (1.20)$$

The resulting values of the 'wet' eigenfrequency are given in Table 1.1. The constant  $\zeta_n$  is introduced by the time dependent function  $q_n = \zeta_n \cdot e^{-i\omega t}$  and is known as the modal amplitude of each mode. The value of these modal amplitudes are defined by the complete equation of motion, which includes fluid damping and the incident wave load [35, 48]:

$$\begin{aligned} (M_{nm} + A_{nm}) \ddot{q}_n - i\omega B_{nm} \dot{q}_n + K_{nm} q_n \\ = \int_L \bar{p}_W(x, t) \cdot W_n(x) dx = F_{FK,n}(\omega) \end{aligned} \quad (1.21)$$

All of the matrices of Equation 1.21 are diagonal matrices, since the influence between the bending modes is not taken into account. The modal coordinate  $\zeta_n$  (of Equation 1.20) is defined for every mode and wave frequency, where the time-depending deformation and the Froude-Krilov force are assumed to be a function of the wave frequency  $q_n = \zeta_n \cdot e^{-i\omega t}$ ,

$$\zeta_n(\omega) = \frac{F_{FK,n}}{M_{nm} + A_{nm}} \left( -\omega^2 - \frac{iB_{nm}\omega}{M_{nm} + A_{nm}} + \omega_n^2 \right)^{-1} \quad (1.22)$$

These modal coordinates are included in Equation 1.13 and the bending deformation is defined by the first six modes as:

$$w(x, t) = \sum_{n=1}^6 W_n(x) \cdot \zeta_n \cdot e^{-i\omega t} \quad (1.23)$$

### Bulging modes

The modal response of the bulging modes is based on simplified mass and momentum-equations as defined by [7, 8], where non-linear terms are neglected:

$$\frac{\partial^2 \chi}{\partial t^2} - \frac{1}{\rho D} \frac{\partial^2 \chi}{\partial x^2} + \frac{1}{\rho D} \frac{T_s D}{4\pi} \frac{\partial^4 \chi}{\partial x^4} = -\frac{1}{\rho} \frac{\partial \bar{p}_e}{\partial x} \quad (1.24)$$

where  $\chi$  is an auxiliary variable which time-derivative represents the section-averaged flow velocity. This auxiliary variable  $\chi(x, t) = \sum_{n=1}^{\infty} X_n(x) c_n(t)$ , is a linear superposition of mode shapes and time-dependent constants. Two boundary conditions are necessary to define the mode shapes at both ends of the tube:

- At the bow and stern the ends are closed and the inner fluid velocity is equal to zero;  $\chi(x = \pm \frac{L}{2}) = 0$ .
- At both ends, the cross-sectional area is fixed;  $\frac{\partial \chi}{\partial x}(x = \pm \frac{L}{2}) = 0$ .

The differential equation relates the internal fluid velocity to the distensibility of the tube ( $D = 1.29 \cdot 10^3$  Pa<sup>-1</sup>), the longitudinal stress of the tube ( $T_s = 18.8 \cdot 10^3$  N) and the fluid density ( $\rho = 1025$  kg/m<sup>3</sup>). The general modeshapes are the solutions of the ordinary differential equation supported by the boundary conditions [8]:

$$\begin{aligned} X_n^{(1)}(x) &= \tanh\left(\frac{K_n^{(1)} L}{2}\right) \frac{\sin(k_n^{(1)} x)}{\cos(k_n^{(1)} L/2)} \\ &\quad - \tan\left(\frac{k_n^{(1)} L}{2}\right) \frac{\sinh(K_n^{(1)} x)}{\cosh(K_n^{(1)} L/2)} \end{aligned} \quad (1.25)$$

$$\begin{aligned} X_n^{(2)}(x) &= K_n^{(2)} \tanh\left(\frac{K_n^{(2)} L}{2}\right) \frac{\cos(k_n^{(2)} x)}{\cos(k_n^{(2)} L/2)} \\ &\quad + k_n^{(2)} \tan\left(\frac{k_n^{(2)} L}{2}\right) \frac{\cosh(K_n^{(2)} x)}{\cosh(K_n^{(2)} L/2)} \end{aligned} \quad (1.26)$$

which are a symmetric and asymmetric solution of the differential equation. The values of  $k_n$ ,  $K_n$  and  $\omega_n$  are found as a solution of the first set of equations (for  $X_n^{(1)}$ ) and the second set of equations (for  $X_n^{(2)}$ ):

$$(S1) \begin{cases} k_n^{(1)} \cdot \tanh \frac{K_n^{(1)} L}{2} - K_n^{(1)} \cdot \tan \frac{k_n^{(1)} L}{2} = 0 \\ \left(k_n^{(1)}\right)^2 = \frac{2\pi}{DT_s} \left( \sqrt{1 + \frac{T_s \rho D^2 (\omega_n^{(1)})^2}{\pi}} - 1 \right) \\ \left(K_n^{(1)}\right)^2 = \frac{2\pi}{DT_s} \left( \sqrt{1 + \frac{T_s \rho D^2 (\omega_n^{(1)})^2}{\pi}} + 1 \right) \\ \left(\omega_n^{(1)}\right)^2 = \frac{(k_n^{(1)})^4 T_s}{4\pi\rho} + \frac{(k_n^{(1)})^2}{D\rho} \end{cases} \quad (1.27)$$

$$(S2) \begin{cases} K_n^{(2)} \cdot \tanh \frac{K_n^{(2)} L}{2} + k_n^{(2)} \cdot \tan \frac{k_n^{(2)} L}{2} = 0 \\ \left(k_n^{(2)}\right)^2 = \frac{2\pi}{DT_s} \left( \sqrt{1 + \frac{T_s \rho D^2 (\omega_n^{(2)})^2}{\pi}} - 1 \right) \\ \left(K_n^{(2)}\right)^2 = \frac{2\pi}{DT_s} \left( \sqrt{1 + \frac{T_s \rho D^2 (\omega_n^{(2)})^2}{\pi}} + 1 \right) \\ \left(\omega_n^{(2)}\right)^2 = \frac{(k_n^{(2)})^4 T_s}{4\pi\rho} + \frac{(k_n^{(2)})^2}{D\rho} \end{cases} \quad (1.28)$$

where the first equations of both sets represent the characteristic equation to define combinations of  $k_n$  and  $K_n$ . The values of  $k_n$ ,  $K_n$  and  $\omega_n$  for a bulge WEC of the given dimensions of a bending tube, are given in Table 1.2. Five 'dry' natural frequencies are observed in the observed range of wave frequencies ( $0.2 < \omega \leq 8.0$ ).

Mode	Type	$k_n$	$K_n$	$\omega_n^{dry}$	$\omega_n^{wet}$
1	(2)	0.34	2.30	0.96	0.92
2	(1)	0.68	2.38	1.97	1.83
3	(2)	1.02	2.50	3.07	2.75
4	(1)	1.35	2.65	4.32	4.03
5	(2)	1.68	2.83	5.73	5.59
6	(1)	2.00	3.03	7.33	7.05

Table 1.2: Values of  $k_n$ ,  $K_n$ ,  $\omega_n^{dry}$ ,  $\omega_n^{wet}$  for the first 6 bulging modes.

According to the differential equation, a structural stiffness and mass matrix are defined. The mass-term is not directly clear from Equation 1.24, but an acceleration-term is observed by the first term of this equation. The mass matrix should therefore be an identity matrix  $\mathbf{I}_n$  [8], since the mass term of the inertia is rearranged. The stiffness matrix is a combination of the second and third term of Equation 1.24, which is defined for each mode shape:

$$K_{nm} = \frac{1}{\rho D} \left( \int_{-L/2}^{L/2} \frac{\partial^2 X_n}{\partial x^2} X_m dx + \frac{T_s D}{4\pi} \int_{-L/2}^{L/2} \frac{\partial^4 X_n}{\partial x^4} X_m dx \right) \quad (1.29)$$

$$M_{nm} = \mathbf{I}_n \quad (1.30)$$

As shown at the right-hand side of Equation 1.24, the loads are assigned to the system in a remarkable way. The influence of the load is defined by the momentum equation which is the basis of the differential equation in combination with the continuity equation. The averaged external loads  $\bar{p}_e$  are defined by a combination of the radiation load  $\bar{p}_R$  and incident wave pressure  $\bar{p}_W$ :

$$-\frac{1}{\rho} \frac{\partial \bar{p}_e}{\partial x} = -\frac{1}{\rho} \frac{\partial \bar{p}_W(x, t)}{\partial x} - \frac{1}{\rho} \frac{\partial \bar{p}_R(x, t)}{\partial x} \quad (1.31)$$

A transformation of the pressure loads into a generalised excitation force and hydrodynamic added mass and damping matrices, requires a mathematical operation to solve the pressure-influence in the differential equation:

$$A_{nm}^* = \frac{1}{\rho} \int_{-L/2}^{L/2} a^{(m)}(\omega) \frac{\partial X_m}{\partial x} dx$$

$$B_{nm}^* = \frac{1}{\rho} \int_{-L/2}^{L/2} b^{(m)}(\omega) \frac{\partial X_m}{\partial x} dx \quad (1.32)$$

$$F_{FK,m}^* = -\frac{1}{\rho} e^{-i\omega t} \cdot \int_{C_0} e^{vz} n dS$$

$$\cdot \int_{-L/2}^{L/2} i \rho g \zeta_a \cdot e^{ivx} \cdot \frac{\partial X_m}{\partial x} dx \quad (1.33)$$

where the hydrodynamic coefficients are defined by the Frank Close-Fit method and these coefficients depend on the frequency. An iterative process is required to define the hydrodynamic coefficients for each mode shape. The 'wet' natural frequency is updated by the iterative process which depends on a simplified equation of motion:

$$(\mathbf{I}_n + A_{nm}^*(\omega_n^{wet})) \ddot{c}_n + K_{nm} c_n = 0 \quad (1.34)$$

where the 'wet' natural frequency will be found by the following eigenvalue problem:

$$\{K_{nm} - (\omega_n^{wet})^2 \cdot (\mathbf{I}_n + A_{nm}^*)\} \cdot \xi_n \cdot e^{-i\omega t} = 0$$

$$(\omega_n^{wet})^2 = \frac{K_{nm}}{\mathbf{I}_n + A_{nm}^*(\omega_n^{dry})} \quad (1.35)$$

The 'wet' eigenfrequencies corresponding with the mode shapes are given in Table 1.2. The particular solution of the ordinary differential equation for the bulging modes also includes the radiation damping matrix and incident wave load (also called the 'Froude-Krilov' force). The equation of motions can be written as a matrix equation:

$$(\mathbf{I}_n + A_{nm}^*) \ddot{c}_n + B_{nm}^* \dot{c}_n + K_{nm} c_n = F_{FK,m}^*(\omega) \quad (1.36)$$

where the matrices are still diagonal matrices, since the bulging modes are not coupled. Therefore, the mode shapes are orthogonal and the modal coordinates can be defined in a simple way. The time-dependent function  $c_n$  is assumed to be an harmonic function, given as  $c_n = \xi_n \cdot e^{-i\omega t}$  where  $\xi_n$  is the normal coordinate related to the incoming wave frequency and the mode:

$$\xi_n(x, \omega) = \frac{F_{FK,m}^*}{1 + A_{nm}^*} \cdot \left( -\omega^2 - i \frac{B_{nm}^* \omega}{1 + A_{nm}^*} + (\omega_n^{wet})^2 \right)^{-1} \quad (1.37)$$

The solution of the auxiliary variable  $\chi(x, t)$  is estimated to be a linear combination of the first six bending modes:

$$\chi(x, t) = \sum_{n=1}^6 X_n(x) \cdot \xi_n(x, \omega) \cdot e^{-i\omega t} \quad (1.38)$$

These first six bending modes are in the observed range of observed wave frequencies ( $0.2 < \omega \leq 8.0$ ). The deformation of the cross-sectional area is related to the spatial derivative of  $\chi(x, t)$  [8]:

$$S(x, t) - S_s = -S_s \cdot \frac{\partial \chi(x, t)}{\partial x}$$

$$= -S_s \cdot \sum_{n=1}^6 \frac{\partial X_n}{\partial x} \cdot \xi_n(x, \omega) \cdot e^{-i\omega t} \quad (1.39)$$

Details about the modal analysis and the derivation of the bulging and bending mode shapes are attached in Appendix E and F.

## Results and discussion

The results of the Frank Close Fit Method for various mode shapes and frequencies are discussed in Subsection a. The mode shapes for bending and bulging are analysed in Subsection b. The wave excitation forces and final deformations of the tube are demonstrated in Subsection c. and d. As a final result, the efficiency of the WEC is defined in Subsection e.

### a. Hydrodynamic coefficients

The method of Frank for a submerged heaving (also referred as bending) circular cross-section is validated with analytical values of added mass and damping of [27, 54]. The results found by the FCFM (solid lines) and the corresponding values of Ogilvie's first order theory (dots) are shown in Figure 1.3. The cylinder is submerged at submersion depth  $d = 1.25 \cdot R$ , where  $R$  is the cylinder's radius. The values of the analytical values of Ogilvie are extrapolated from the non-dimensional values, which causes some deviations in the analytical values. In general, the values of the first order theory of Ogilvie comply with the FCFM method, where both methods do not include viscous effects.

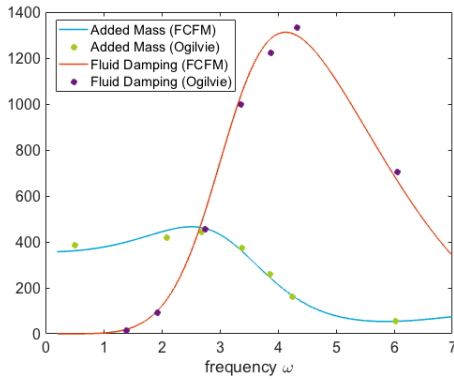


Figure 1.3: 2D hydrodynamic coefficients of a cylinder submerged at  $d/R = 1.25$ .

These hydrodynamic coefficients are inserted into the modal analysis, where these coefficients are included in the computation of the hydrodynamic matrices as given by Equation 1.19 (for bending) and 1.32 (for bulging). The results of the three-dimensional hydrodynamic coefficients of matrix  $A_{nm}$  and  $B_{nm}$  of the bending modes are shown in Figure 1.4. The purple dots represent the diagonal coefficients of the matrix  $A_{nm}$  and  $B_{nm}$ , which are the three-dimensional hydrodynamic coefficients for the corresponding 'wet' natural frequencies. Small differences are obtained between the different modes,

which is due to the integration of the hydrodynamic coefficients over the mode shapes as defined in Equation 1.19. The values of the added mass are around the order of the mass of the total tube, which is  $M_{nn} = 917$  kg.

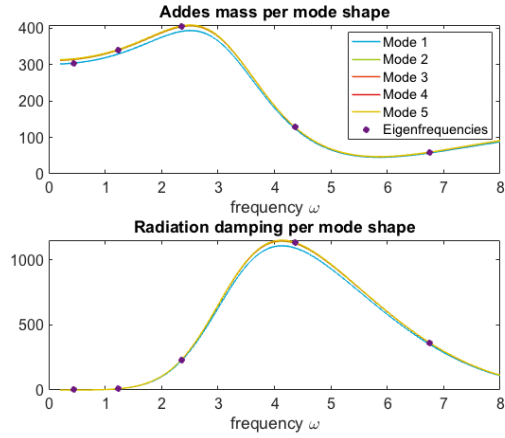


Figure 1.4: Hydrodynamic coefficients ( $A_{nm}(\omega)$  and  $B_{nm}(\omega)$ ) of first five bending modes.

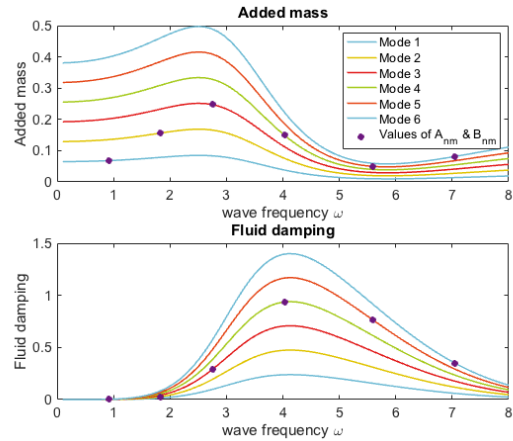


Figure 1.5: Hydrodynamic coefficients ( $A_{nm}(\omega)$  and  $B_{nm}(\omega)$ ) of first six bulging modes.

The definition of the hydrodynamic matrices  $A_{nm}$  and  $B_{nm}$  for the bulging modes (see Equation 1.32) differs between the bending modes. Deviations between the different mode shapes (see Figure 1.5) are more obvious due to the relation between these matrices and the spatial derivative of  $\chi(x, t)$ . The magnitudes of the hydrodynamic coefficients of bulging in Figure 1.5 are substantially smaller than the same coefficients of bending. These differences are caused by the factor  $1/\rho$  in Equation 1.32 and the amplitude as a result of  $\partial\chi/\partial x$ .

The hydrodynamic coefficients of the first six bending modes, which are represented by purple dots, can be compared with the two-dimensional results of Figure 1.3. The values of each mode shape

correspond to the two-dimensional results of the heaving cylinder, where small difference between the mode shapes are obtained by the normalisation of the individual mode shapes. The results of the hydrodynamic coefficients of the bulging modes can be verified with the numerical results of Babarit et al. [8] (for the second mode in Figure 1.6). The results of [8] are represented by the blue dashed line for the added mass and by the green dashed line for damping. The results of the adapted modal analysis based on the FCFM method are represented by the solid blue and green lines. Differences between the two numerical results are caused by three-dimensional effects, which are not fully included in the modal analysis and the FCFM. The FCFM provides two-dimensional hydrodynamic coefficients which point in the radial directions, interactions between two 'strips' due to deformation are not included. In the bending modes, the Euler-beam method is used, which assumes the small elements (or 'strips') not to translate with respect to the beam's longitudinal axis. In reality, these elements will rotate due to bending and hydrodynamic coefficients of neighbouring strips will interact with each other.

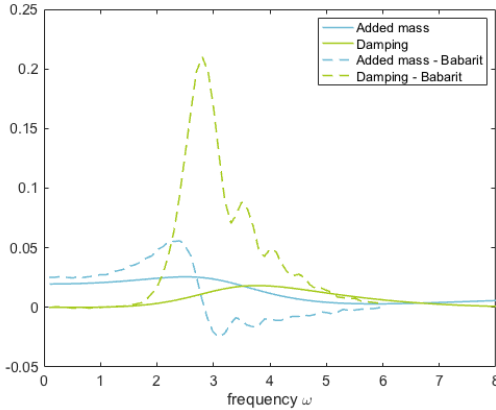


Figure 1.6: Added mass and radiation damping coefficients of third bulging mode as calculated by [8].

In [26], a note is added about very low and large frequencies in the 2D approach. An adaption of the Green's function is suggested, which will contribute a constant value to the velocity potential in case of a partly submerged body exposed to a harmonic heave motion. For submerged bodies, this contribution vanished. The last two terms of Equation 1.2 are not included in the Green's function any more. This adaptation for the small frequency range is not included in the FCFM model, however it could affect the hydrodynamic coefficients in the lower frequency ranges as well as in the higher frequency ranges.

## b. Mode shapes

The mode shapes defined by Equations 1.14 (bending), 1.25 and 1.26 (bulging) are presented in Figures 1.7 and 1.8.

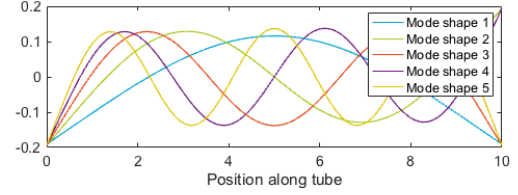


Figure 1.7: The first five bending mode shapes.

These modes are checked by their boundary conditions, which is provided in Appendix F.

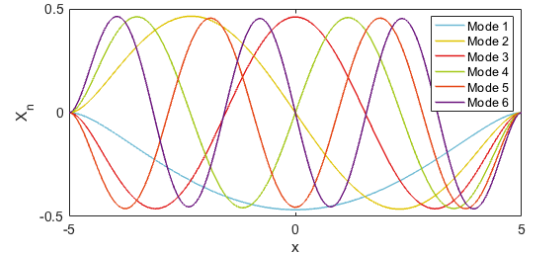


Figure 1.8: The first six bulging mode shapes.

For both motions, numerical eigenfrequencies are found due to the numerical solution of the characteristic equations. Mode shapes that belong to these numerical eigenfrequencies are not included since they do not fulfil the boundary conditions.

## c. Generalised wave-exciting force

The generalised wave-exciting forces are related to the first five bending and six bulging modes, as given by Equation 1.21 and 1.33. The incident wave interacts with the mode shape and is integrated along the tube, where the generalised values are shown in Figure 1.9 for the first five bending modes. The solid lines represent the wave-exciting forces as calculated by Equation 1.21. The dashed lines show the wave frequency of the equivalent wavelengths of the corresponding mode shapes.

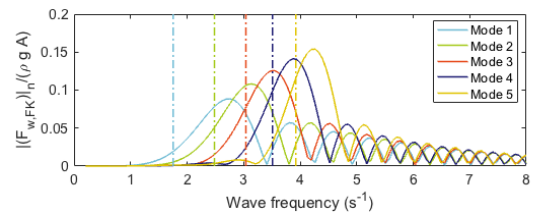


Figure 1.9: Generalised wave-exciting force ( $F_{FK,n}(\omega)$ ) for the first five bending modes.

For the first mode shape the corresponding wavelength is  $2 \cdot L = 20$  m. The blue dashed line is closer to the pressure load peak for bulging than for bending. The local peaks of the wave-exciting force are

related to resonance of the incoming wave with the mode shapes, and since the mode shapes of bulging are more similar to pure trigonometric functions, the peaks of bulging correspond better to the dashed resonance frequencies.

Figure 1.10 shows the generalised wave-exciting force of the second bulging mode. The solid blue line indicates the values found by the adapted modal analyses and the dashed line represents the equivalent wavelength  $\lambda_2 = L$ . The generalised wave-excitation force is also calculated by [8], where the excitation load and Froude-Krilov force are indicated by the green and blue dots in Figure 1.10. The excitation load of [8] includes the Froude-Krilov and diffraction force, which is not included in the FCFM modal analysis model. The values of the Froude-Krilov force of [8] corresponds to the generalised wave-exciting force found by the adapted modal analysis, as expected.

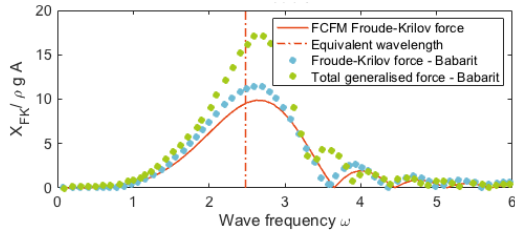


Figure 1.10: Excitation load for the second bulging mode defined by the adapted modal analysis model and the numerical model of [8].

More details and figures related to verification of the wave-exciting force are attached in Appendix F.

#### d. Deformation of a tube

The modal coordinates of the individual bending and bulging modes are inserted into Equation 1.23 and Equation 1.39, where the total deformation on each position due to bending or bulging is defined.

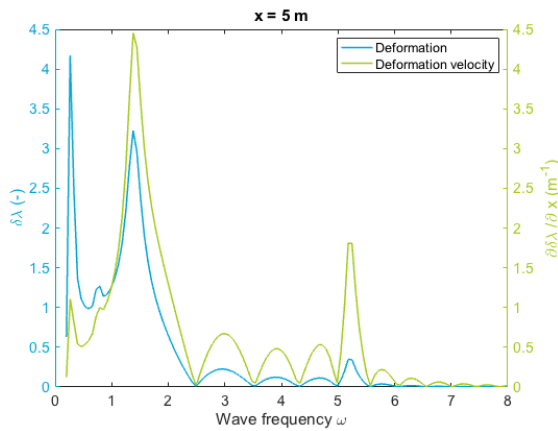


Figure 1.11: Bending deformation ( $w(x, \omega)$ ) at the midpoint of the beam ( $x = 5$  m).

At the midpoint of the tube (for bending at  $x = 5$  m and for bulging at  $x = 0$  m) these deformations are presented in Figure 1.11 and Figure 1.12.

Some of the peaks observed in the figures, correspond to the 'wet' frequencies of the bending or bulging mode. Other peaks are related to local excitation pressure peaks (especially in higher frequency ranges). One interesting finding is that the response of bending and bulging is significant in the same frequency region. The peak at  $\omega \approx 1.8$  Hz in Figure 1.12 corresponds to the second bulging mode. For bending, the first mode ( $\omega_n^{wet} = 0.453$  Hz) and second mode ( $\omega_n^{wet} = 1.230$  Hz) dominate the modal deformation. At these frequencies, the radiation damping is very low, but inclusion of material damping and inner fluid damping will decrease the response to this 'wet' natural frequency [8].

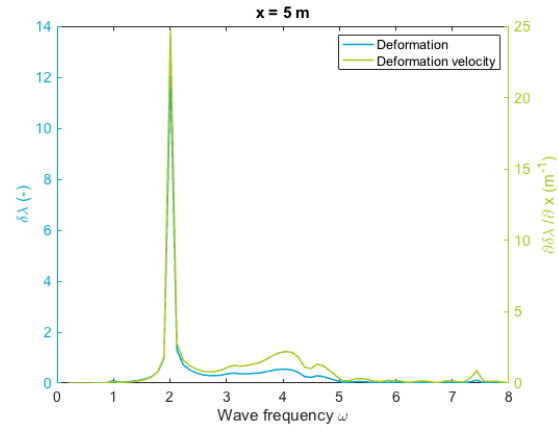


Figure 1.12: Bulging deformation ( $\delta\lambda = \frac{S}{S_s} - 1$ ) at the midpoint of the beam ( $x = 0$  m).

#### e. WEC efficiency

The efficiency of both deformation modes is shown in Figure 1.13. The efficiency as the ratio between absorbed power of the WEC and the mean energy of an incident wave crest of 1 m width. The absorbed power is defined by the force due to damping of the bulge WEC and the fluid velocity due to the deformations  $U^{(m)}$ . In this linear model the hydrodynamic damping is used as damping force in the definition of the time-averaged absorbed power by the WEC ( $\bar{P}$ ) for bending and bulging:

$$\bar{P} = \overline{F_{rad,D}^{(m)} \cdot U^{(m)}} = \frac{1}{T} \int_T F_{damp}^{(m)} \cdot U^{(m)} dt \quad (1.40)$$

where  $T$  is the wave period and the damping force  $F_{damp}$  due to radiation and a Power Take-Off (PTO) is

defined by:

$$F_{damp}^{(3)} = \sum_{n=1}^5 \int_L (B_{PTO} + b^{(3)}(\omega)) W_n \dot{q}_n(t) \cdot dx$$

$$F_{damp}^{(4)} = \sum_{n=1}^6 \int_L \left( B_{PTO} + \frac{h_s S_s b^{(4)}(\omega)}{\rho R_s} \right) \cdot \frac{\partial X_n(x)}{\partial x} \dot{c}_n(t) dx \quad (1.41)$$

The deformation velocity  $U^{(m)}$  is defined for bending and bulging by:

$$U^{(3)}(x, t) = \frac{\partial w(x, t)}{\partial t} = \sum_{m=1}^5 W_m(x) \dot{q}_m(t)$$

$$U^{(3)}(x, t) = \frac{\partial}{\partial t} \frac{\partial \chi(x, t)}{\partial x} = \sum_{m=1}^6 \frac{\partial X_m(x)}{\partial x} \dot{c}_m(t) \quad (1.42)$$

Equations 1.41 and 1.42 can be substituted in Equation 1.40 to find the mean absorbed power by the WEC. The mean wave energy per meter width is expressed by  $J_W = \rho g^2 \zeta_l^2 / 4\omega$  [72], which contributes to the definition of the WEC efficiency,

$$\eta_{wec} = \frac{\tilde{P}/L}{J_W} \quad (1.43)$$

The values of the of bending and bulging are shown in Figure 1.13, where the bending results are related to the left vertical axis and the bulging efficiency is related to the right vertical axis.

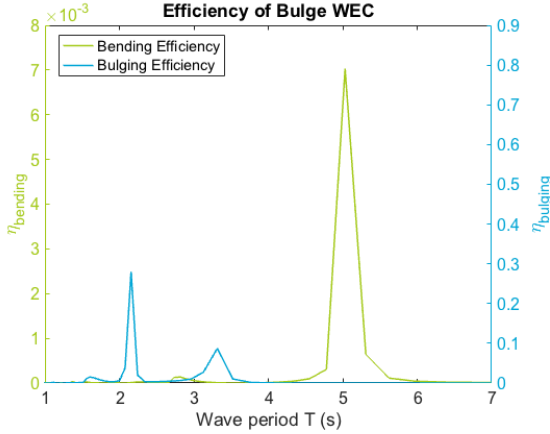


Figure 1.13: WEC efficiency ( $\eta_{wec}$ ) of bending motions on left vertical axis and bulging motions on right vertical axis with  $B_{PTO} = 100$  Pa.s.

The values of bending are relative small compared to the power absorbed by the bulging motions, which means that conversion of wave energy into power is dominated by the bulging motion. Since bending and bulging deformations and power conversion are in the same frequency range, it is interesting to include both motions in the hydro-elastic analysis of a bulge WEC. Since the WEC efficiency calculation is based on radiation damping and a mechanical damper (the PTO), not all energy is captured. Further work can improve the efficiency of the WEC with the addition of several non-linear damping terms, such as wall damping and inner fluid damping.

## Conclusions

The Frank Close-Fit method can contribute to the prediction of hydro-elastic response of a bulge WEC in regular waves. The method is shown to be a fast tool to calculate the two-dimensional hydrodynamic coefficients for added mass and damping of bending and bulging deformations. The two-dimensional coefficients are translated into the three-dimensional hydrodynamic matrices which contribute to the equation of motion for bending and bulging. Since the values of these hydrodynamic matrices are iterated until the 'wet' frequency is found, the coupling between modal deformation and fluid radiation effects is related by two-way coupling. The final bending and bulging deformation rates are significant in the observed frequency, which confirms the hypothesis that bending of the tube is of importance in the hydro-elastic response of a bulging WEC.

More research that incorporates experimental values is needed to validate the numerical model for both bending and bulging modes. The numerical model itself could be expanded by the addition of wall damping and inner fluid damping and including diffracted wave loads in the model. A further study could provide extra terms to model the non-radial effects of the two-dimensional added mass and damping coefficients in the three-dimensional modal analysis.

Further research might explore more valuable results of a hydro-elastic numerical method that includes the Frank's Close-Fit method for other types of deformable body applications.

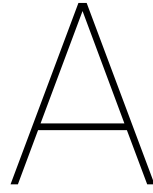
# Bibliography

- [1] Wave devices : EMEC: European Marine Energy Centre. URL <http://www.emec.org.uk/marine-energy/wave-devices/>.
- [2] Renewable Energy - SBM Offshore. URL <https://www.sbmoffshore.com/what-we-do/our-products/renewables/>.
- [3] Downloads and Resources - Wave Technologies, 2012. URL <http://www.aquaret.com/images/stories/aquaret/stills/bulgewave-animationstill.bmp>.
- [4] Fluid-Structure Interaction, 2017. URL <https://www.comsol.com/multiphysics/fluid-structure-interaction>.
- [5] Electricity from Ocean Wave, 2018. URL <http://potomacstewards.com/wavepower>.
- [6] Aurélien Babarit and Pierre Ferrant. Investigation on the radiation and diffraction forces of a bulging tube. *26th International Workshop of Water Waves and Floating Bodies*, (2):2–5, 2011.
- [7] Aurélien Babarit, Benjamin Gendron, Jitendra Singh, Cécile Melis, and Philippe Jean. Numerical and experimental modeling of an electro-active deformable wave energy converter. 2013.
- [8] Aurélien Babarit, Jitendra Singh, Cécile Méliis, Ambroise Wattez, and Philippe Jean. A linear numerical model for analysing the hydroelastic response of a flexible electroactive wave energy converter. *Journal of Fluids and Structures*, 74:356–384, 2017. ISSN 10958622. doi: 10.1016/j.jfluidstructs.2017.06.003.
- [9] R. E D Bishop and W. G. Price. On the relationship between "dry modes" and "wet modes" in the theory of ship response. *Journal of Sound and Vibration*, 45(2):157–164, 1976. ISSN 10958568. doi: 10.1016/0022-460X(76)90595-2.
- [10] R. E. D. Bishop, R. Eatock Taylor, and K. L. Jackson. On the structural dynamics of ship hulls in waves. *Transactions of the Royal Institution of Naval Architects*, 115:257–274, 1973.
- [11] K. Budar and J. Falnes. A resonant point absorber of ocean-wave power. *Nature*, 256(7):478–479, 1975.
- [12] J. R. Chaplin, F. J. M. Farley, M. E. Prentice, R. C. T. Rainey, S. J. Rimmer, and A. T. Roach. Development of the ANACONDA all-rubber WEC. In *Proceedings of the 7th European Wave and Tidal Energy Conference*, Porto, 2007. URL [www.bulgewave.com](http://www.bulgewave.com).
- [13] J. R. Chaplin, F. J. M. Farley, and G. E. Hearn. Hydrodynamic performance of the Anaconda Wavepower Device. *Proc. Of the ...*, (February):1–4, 2010. URL <https://www.researchgate.net/publication/268367051-Hydrodynamic-performance-of-the-Anaconda-wavepower-device>.
- [14] J. R. Chaplin, V. Heller, F. J.M. Farley, G. E. Hearn, and R. C.T. Rainey. Laboratory testing the Anaconda. *Philosophical Transactions of the Royal Society A: Mathematical, Physical and Engineering Sciences*, 370 (1959):403–424, 2012. ISSN 1364503X. doi: 10.1098/rsta.2011.0256.
- [15] Nicolas Choplain. Interactions of a submerged membrane with water waves and its use in harnessing nearshore wave power. 2012.
- [16] S. Copar. Seminar: Alternative hydroelasticity, 2009. URL <http://mafija.fmf.uni-lj.si/seminar/files/2008-2009/copar-seminar-eng.pdf>.
- [17] Robert H. Cox. Comparison of linearized wave propagation models for arterial blood flow analysis. *Journal of Biomechanics*, 2:251–265, 1969.

- [18] I. O. Erselcan. *A frequency domain strip theory applied to the seakeeping of the Zumwalt-class destroyer*. student thesis, Massachusetts Institute of Technology (MIT), 2010. URL <https://dspace.mit.edu/bitstream/handle/1721.1/61868/705937590-MIT.pdf;sequence=2>.
- [19] António Ede O. Falcão. Wave energy utilization: A review of the technologies. *Renewable and Sustainable Energy Reviews*, 14(3):899–918, 2010. ISSN 13640321. doi: 10.1016/j.rser.2009.11.003.
- [20] O. M. Faltinsen. A study of the two-dimensional added-mass and damping coefficients by the Frank close-fit method. Technical report, Det Norske Veritas, Oslo, 1969.
- [21] F. J. M. Farley and R. C. T. Rainey. Radical design options for wave-profiling wave energy converters. In *21st International Workshop on Water Waves and Floating Bodies*, number April, pages 2–6, Loughborough, UK, 2006.
- [22] F. J. M. Farley and R. C. T. Rainey. Distensible tube wave energy converter, 2011. ISSN 2004001828.
- [23] F. J. M. Farley, R. C. T. Rainey, and J. R. Chaplin. Rubber tubes in the sea. *Philosophical Transactions of the Royal Society A: Mathematical, Physical and Engineering Sciences*, 370(1959):381–402, 2012. ISSN 1364503X. doi: 10.1098/rsta.2011.0193.
- [24] Dariusz E. Fathi, Chang-Ho Lee, and J. Nicholas Newman. Computations of wave induced motions on a flexible container. In O. Faltinsen, C. M. Larsen, and T. Moan, editors, *International Conference on hydroelasticity in marine technology*, pages 301–308, Rotterdam, 1994.
- [25] N. Fonseca. 4 Methods to calculate the 2D potential coefficients. URL <https://fenix.tecnico.ulisboa.pt/downloadFile/3779571245980/MicrosoftPowerPoint-2Dpotentialflowmethods2.ppt.pdf>.
- [26] W. Frank. Oscillation of Cylinders in or below the free Surface of Deep Fluids. Technical Report October, Naval Ship Research and Development Center, Washington, D.C., 1967.
- [27] W. Frank and N. Salvesen. The Frank close-fit ship-motion computer program. Technical report, Naval ship research and development center, Washington, D.C., 1970.
- [28] W. Gautschi and W.F. Cahill. Exponential Integral and Related Functions. In M. Abramowitz and I.A. Stegun, editors, *Handbook of Mathematical Functions with Formulas, Graphs and Mathematical Tables*, chapter 5, pages 227–228. National Bureau of Standards, Washington, D.C., 1 edition, 1964. URL [http://people.math.sfu.ca/~cbm/aands/page\\_{\\_}227.htm](http://people.math.sfu.ca/~cbm/aands/page_{_}227.htm).
- [29] J.H. Gerrard. An experimental test of the theory of waves in fluid-filled deformable tubes. *Journal of Fluid Mechanics*, 156:321–347, 1985. ISSN 14697645. doi: 10.1017/S0022112085002129.
- [30] J.P. Giesing and A.M.O. Smith. Potential flow about two-dimensional hydrofoils. *Journal of Fluid Mechanics*, 28(1):113–129, 1967. ISSN 14697645. doi: 10.1017/S0022112067001934.
- [31] R.C. Hibbeler. Thin-Walled Pressure Vessels. In *Mechanics of Materials*, chapter 8, pages 435–438. Pearson, Jurong, 7 edition, 2008. ISBN 978-981-06-7994-1.
- [32] F. B. Hildebrand. Functions of a Complex Variable. In *Advanced Calculus for Applications*, chapter 10, pages 539–622. Prentice-Hall, Inc., New Jersey, 2 edition, 1976. ISBN 0-13-011189-9.
- [33] D.S. Holloway. *A High Froude Number Time Domain Strip Theory Applied to the Seakeeping of Semi-SWATHs*. Doctoral thesis, University of Tasmania, 1998.
- [34] L. H. Holthuijsen. Linear wave theory (oceanic waters). In *Waves in Oceanic and Coastal Waters*, chapter 5, pages 106–144. Cambridge University Press, New York, 3 edition, 2007. ISBN 978-0-521-12995-4.
- [35] S. Hylarides, T. N. Bosman, and H.L. Vredeveldt. Reader Scheepstrillingen en Geluid, 2013.
- [36] J. M. J. Journée. Quick strip theory calculations in ship design. In *PRADS'92 Conference on Practical Design of Ships and Mobile Structures*, volume I, pages 5–12, Newcastle, 1992. URL <http://www.shipmotions.nl/DUT/PapersReports/0902-PRADS-92.pdf>.

- [37] J. M. J. Journée, W. W. Massie, and R. H. M. Huijsmans. *Offshore Hydromechanics*. 3:7.1–7.41, 2015.
- [38] P.A. Kelly. Viscoelasticity. In *Lecture Notes: An introduction to Solid Mechanics*, chapter 10, pages 283–342. Auckland, 2015. URL [http://homepages.engineering.auckland.ac.nz/~pkel015/SolidMechanicsBooks/Part\\_I/BookSM\\_Part\\_I/10\\_Viscoelasticity/10\\_Viscoelasticity\\_Complete.pdf](http://homepages.engineering.auckland.ac.nz/~pkel015/SolidMechanicsBooks/Part_I/BookSM_Part_I/10_Viscoelasticity/10_Viscoelasticity_Complete.pdf).
- [39] L.J. Kemp. *Frank's 2D close-fit method*. Research assignment, Delft University of Technology, 2017.
- [40] C. H. Kim. *Ocean Engineering*. Technical Report 10, Stevens Institute of Technology, New Jersey, 1972.
- [41] Harald E. Krogstad and Øivind A. Arntsen. Lecture notes on Linear Wave Theory, 2000. ISSN 1469493X. URL [http://folk.ntnu.no/oivarn/hercules\\_ntnu/LWTcourse/lwt\\_new2000\\_Part\\_A.pdf](http://folk.ntnu.no/oivarn/hercules_ntnu/LWTcourse/lwt_new2000_Part_A.pdf).
- [42] G. Kundu, P.K., Cohen, I.M., Dowling, D.R. and Tryggvason. *Fluid Mechanics*. Elsevier Inc., Oxford, 6th editio edition, 2016. ISBN 978-0-12-405935-1.
- [43] C.M. Lee, H. Jones, and J.W. Bedel. Added Mass and Damping Coeficients of Heaving Twin Cyliners in a Free Surface. Technical Report August, Department of the navy naval ship research and development center, Bethesda, 1971.
- [44] James Lighthill. *Waves in fluids*. Cambridge University Press, Cambridge, 1978. ISBN 0521010454.
- [45] M. C. Linton and P. McIver. Energy of the fluid motion. In *Handbook of Mathematical Techniques for Wave/Structure Interactions*, chapter 1, pages 19–21. CRC Press LLC, Boca Raton, 2001.
- [46] Yingyi Liu, Ying Gou, Bin Teng, and Shigeo Yoshida. An extremely efficient boundary element method for wave interaction with long cylindrical structures based on free-surface Green's function.pdf. *Computation*, 4(3), 2016. URL <https://www.mdpi.com/2079-3197/4/3/36>.
- [47] G. Løland and J.V. Aarsnes. Fabric as construction material for marine applications. In O.M. Faltinsen, C.M. Larsen, and T. Moan, editors, *Hydroelasticity in Marine Technology*, pages 275–286. A.A. Balkema, Rotterdam, 1994. ISBN 9054103876.
- [48] Eva Loukogeorgaki, Constantine Michailides, and Demos C. Angelides. Hydroelastic analysis of a flexible mat-shaped floating breakwater under oblique wave action. *Journal of Fluids and Structures*, 31: 103–124, 2012. ISSN 08899746. doi: 10.1016/j.jfluidstructs.2012.02.011. URL <http://dx.doi.org/10.1016/j.jfluidstructs.2012.02.011>.
- [49] P. McIver and D.V. Evans. The occurrence of negative added mass in free-surface problems involving submerged oscillating bodies. *Journal of Engineering Mathematics*, 18:7–22, 1984.
- [50] C. Michailides, E. Loukogeorgaki, and D.C. Angelides. Influence of connectors' stiffness on the performance of flexible floating breakwaters. *the 19th International Offshore and Polar Engineering Conference, ISOPE*, 1:1094–1101, 2009. ISSN 10986189 15551792.
- [51] G.W. Morgan and J.P. Kiely. Wave Propagation in a Viscous Liquid Contained in a Flexible Tube. *The Journal of the Acoustical Society of America*, 26(3):323–328, 1954. ISSN 0001-4966. doi: 10.1121/1.1907335. URL <http://asa.scitation.org/doi/10.1121/1.1907335>.
- [52] J.N. Newman. *Marine Hydrodynamics*. The MIT Press, Cambridge, 1977. ISBN 0-262-14026-8.
- [53] J.N. Newman. Wave effects on deformable bodies. *Applied Ocean Research*, 16:47–59, 1994.
- [54] T. Francis Ogilvie. First- and second-order forces on a cylinder submerged under a free surface. *Journal of Fluid Mechanics*, 16(03):451, 1963. ISSN 14697645. doi: 10.1017/S0022112063000896. URL [http://www.journals.cambridge.org/abstract\\_S0022112063000896](http://www.journals.cambridge.org/abstract_S0022112063000896).
- [55] S. S. Rao. Continuous Systems. In Y. F. Fah, editor, *Mechanical Vibrations*, chapter 8, pages 699–751. Pearson Education, South Asia, Singapore, 5 edition, 2011.

- [56] C. Retzler. Measurements of the slow drift dynamics of a model Pelamis wave energy converter. *Renewable Energy*, 31(2):257–269, 2006. ISSN 09601481. doi: 10.1016/j.renene.2005.08.025.
- [57] A Roessling and J V Ringwood. Finite order approximations to radiation forces for wave energy applications. *Renewable Energies Offshore*, (3):359–366, 2015.
- [58] Lucie Rouleau, Jean François Deü, and Antoine Legay. A comparison of model reduction techniques based on modal projection for structures with frequency-dependent damping. *Mechanical Systems and Signal Processing*, 90:110–125, 2017. ISSN 10961216. doi: 10.1016/j.ymsp.2016.12.013. URL <http://dx.doi.org/10.1016/j.ymsp.2016.12.013>.
- [59] K. Sato. Complex Potential and Differentiation. In *Complex Analysis for Practical Engineering*, pages 19–79. Springer, Tokyo, 2015. ISBN 9783319130620. doi: 10.1007/978-3-319-13063-7.
- [60] Warren R. Smith. Wave–structure interactions for the distensible tube wave energy converter. *Proceedings of the Royal Society A: Mathematical, Physical and Engineering Science*, 472(2192), aug 2016. URL <http://rspa.royalsocietypublishing.org/content/472/2192/20160160.abstract>.
- [61] T. Sochi. Navier-Stokes flow in converging-diverging distensible tubes. *Alexandria Engineering Journal*, 54(3):713–723, 2015. ISSN 11100168. doi: 10.1016/j.aej.2015.03.028.
- [62] A. F. Spaargaren. *Excitation forces on a flexible wave energy converter*. Student thesis, Delft University of Technology, 2016.
- [63] F. Ursell. On the heaving motion of a circular cylinder on the surface of a fluid. *The Quarterly Journal of Mechanics and Applied Mathematics*, 2(2):218–231, 1949. URL <https://academic.oup.com/qjmam/article/2/2/218/1841872>.
- [64] F. Ursell and W. R. Dean. Surface waves on deep water in the presence of a submerged cylinder I. *Mathematical Proceedings of the Cambridge Philosophical Society*, 46(2):141–152, 1949.
- [65] R. van Loon, P. D. Anderson, F. N. van de Vosse, and S. J. Sherwin. Comparison of various fluid-structure interaction methods for deformable bodies. *Computers and Structures*, 85(11-14):833–843, 2007. ISSN 00457949. doi: 10.1016/j.compstruc.2007.01.010.
- [66] R. van ’t Veer. *Catamaran seakeeping prediction*. Student thesis, Delft University of Technology, 1993.
- [67] R. van ’t Veer. ASAP4, 1993.
- [68] J. H. Vugts. The hydrodynamic coefficients for swaying, heaving and rolling cylinders in a free surface. *International Shipbuilding Progress*, 15:251–276, 1968.
- [69] J. H. Vugts. *The Hydrodynamic Forces and Ship Motions in Waves*. PhD thesis, Delft University of Technology, 1970.
- [70] J. W. Wehausen and E.V. Laitone. Surface Waves. *Handbuch der Physik*, pages 446–778, 1960.
- [71] E.W. Weisstein. Principal Branch, 2018. URL <http://mathworld.wolfram.com/PrincipalBranch.html>.
- [72] Hugh A. Wolgamot and Colm J. Fitzgerald. Nonlinear hydrodynamic and real fluid effects on wave energy converters. *Proceedings of the Institution of Mechanical Engineers, Part A: Journal of Power and Energy*, 229(7):772–794, 2015. ISSN 20412967. doi: 10.1177/0957650915570351.
- [73] J.R. Womersley. XXIV. Oscillatory motion of a viscous liquid in a thin-walled elastic tube—I: The linear approximation for long waves. *The London, Edinburgh, and Dublin Philosophical Magazine and Journal of Science*, 46(373):199–221, 1955. ISSN 1941-5982. doi: 10.1080/14786440208520564. URL <http://www.tandfonline.com/doi/abs/10.1080/14786440208520564>.
- [74] X-J. Wu. A Two-Dimensional Source-Dipole Method for Seakeeping Analysis of Ships and Offshore Structures. In G.A. Keramidas, editor, *CADMO 86 - Proceedings of the International Conference on Computer Aided Design, Manufacture and Operation in the Marine and Offshore Industries*, chapter A4 - Ship, pages 223–235. Springer-Verlag Berlin, Heidelberg, 1986. ISBN 0-905451-59-7.



# Problem definition

This appendix includes background information about the theory used in this research project <sup>1</sup>. The Frank's close-fit method is used as a two-dimensional panel method, which will be used in a hydro-elastic problem, as addressed in the first section. Several governing equations are mentioned, which are used in the following appendices. Section A.2 indicates the main and subquestions during the research process.

## A.1. Background and problem

Wave energy is an interesting source of energy, which is partly a sustainable solution to the energy demand. Several types of wave energy converters (WECs) are developed in the past decades. These wave energy converters can be divided into three main categories [72]:

- Wave overtopping devices.
- Oscillating Water Column (OCW) devices.
- Wave-activated devices.

For each of this category, different designs are designed and some of them are already tested at full scale experiments. The interesting part of Wave energy converters is the complex interaction between waves, deformations and energy transition.

### Wave energy converters

The hydro-elasticity is a very important aspect for wave energy converters (WECs). A wave energy converter is a device that absorbs energy from the waves and converts it to an electric current that will be generated by a power take off (PTO). Various types of wave energy converters are defined by the EMEC [1]:

1. Attenuator
2. Point absorber
3. Oscillating wave surge converter
4. Oscillating water column (OWC)
5. Overtopping/terminator device
6. Submerged pressure differential
7. Bulge wave
8. Rotating mass
9. Other

In 1994 Newman wrote a paper about wave effects on a deformable body [53], which complies with an attenuator or a bulge wave energy converter. He did some computations on several illustrative set-ups. One of his calculations is about the motions of a hinged barge. This hinged bar shows some similarities with the concept of an attenuator. The hinged bar described by Newman is shown in Figure A.1. An example of an attenuator

---

<sup>1</sup>This part of the report was initially the plan of approach of the research.

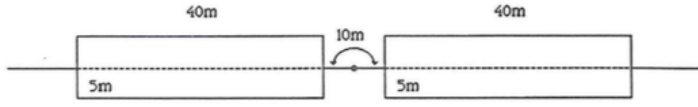


Figure A.1: Configuration of the hinged barges by Newman [53]

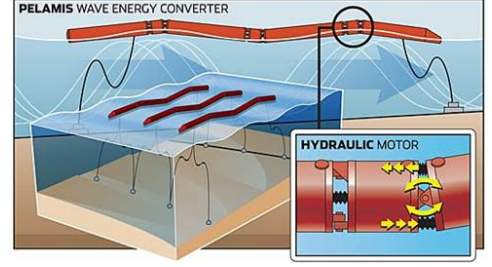


Figure A.2: Layout of the Pelamis Wave Energy Converter [5]

is the Pelamis, which layout is shown in figure A.2. The Pelamis is composed of four coupled 'rigid' cylinders, which have a total length in the order of a wavelength. Due to mooring the Pelamis and the flexibility, the Pelamis is self-referencing. The Pelamis is therefore excited mainly by the slowly varying second-order drift forces, which forces are used for the power absorption. Electric power is delivered by the hinges where high-pressure fluid is pumped into an accumulator [56].

Newman defines the body deformation modes in terms of the conventional rigid-body motions (surge, sway, heave, roll, pitch and yaw) denoted by  $\mathbf{S}_j$ , where the index  $j$  defines the motion. The modal displacement (or shape function)  $\mathbf{S}_j$  is assumed to be continuous and differentiable near the surface of the distensible tube. The shape function  $\mathbf{S}_j$  has a divergence  $D_j = \nabla \cdot \mathbf{S}_j$ , which is equal to zero for a rigid-body motion. Newman assumed potential flow and he linearized the body and free surface boundary conditions, which results in first-order pressure forces for each mode of motion [53]:

$$F_i = \iint_{S'_b} p n_i dS = -\rho \iint_{S_b} (i\omega\Phi + gz) n_i dS \quad (\text{A.1})$$

where the term  $i\omega\Phi$  is added as the trivial extension of the 'common' rigid-body analysis. Newman states that deformation of the body's geometry must be considered from the hydrostatic pressure  $-\rho gz$  since this pressure is of the order one. Separation of the initial wetted surface  $S_s$  and the deformed surface  $S_\delta$  after displacement in the considered mode gives a stiffness matrix<sup>2</sup> [53]:

$$c_{ij} = \rho g \iint_{S_\delta} z n_i dS - \iint_{S_s} z n_i dS \quad (\text{A.2})$$

For small deformations, the volume between the initial and deformed surface  $v$  is also small. Equation A.2 reduces to:

$$c_{ij} = \rho g \iint_{S_s} n_j (w_i + z D_i) dS \quad (\text{A.3})$$

where only the hydrostatic pressure is considered (due to the order of this pressure) in the generalised force.  $w_i$  is known as the  $z$ -component of  $\mathbf{S}_i$ , where the subscript  $i$  is an index to couple the modes  $i$  and  $j$ .

Not only the pressure forces are adapted in the case of a deformable body, also the mass force must be evaluated separately. The mass distribution is depending on the mode shape and should be evaluated separately [53].

Application of these formulations on a hinged barge-system is only considered for the hinge, since the barges themselves are considered as two rigid bodies. The interaction is captured in the discontinuous relative motion between these two rigid bodies. The hinged barge is symmetrical around the axis of the hinge, where the hinge does not affect the modes.

Calculations of the two barges in a hinged-configuration shows a greater vertical motion for the barge compared to the conventional considered heave motion of the rigid connected barges [53]

At least the concepts of the attenuator (like the Pelamis) and bulge wave energy converter are interesting to review with the Frank Close-Fit Method (FCFM) adapted for hydro-elasticity. This Frank close-fit method could provide hydrodynamic coefficients, which describe the radiation effects of the motions of a deformable body in hydro-elasticity.

<sup>2</sup>The stiffness matrix  $c_{ij}$  defines the change in hydrostatic force component  $F_i$  due to a unit displacement in mode  $j$  [53].

### Frank's close-fit method

The Frank close-fit method is a tool to calculate 2D potential coefficients. Frank has designed the close-fit method in 1967 for any arbitrary cross-sectional shape, which is partly or fully submerged [25].

Frank assumed in his report an irrotational, incompressible and inviscid flow which could be described by a 2D potential. He reduced the problem to a boundary-value problem of potential flow, where a forced oscillation is applied to the 2D cross section [26].

The contour of the cross section is divided into a finite number of segments, denoted by  $N_{elem}$ . Each segment represents a complex source or sink, where the complex source density is assumed to be constant along a segment. The flow on each segment is influenced by the sources and sinks from all the segments distributed over the submerged contour. His method solves the complex potential along the contour, where the resulting pressure distribution along the hull has a component in phase with the displacement and a term in phase with the velocity.

Integration of the term in phase with the displacement over the contour will result in a value for the 2D added mass coefficient of the arbitrary cross-sectional shape. The 2D damping coefficient is found by integration of the velocity-depending part of the pressure along the submerged contour. In 1967 this method was one of the methods used to determine hydrodynamic coefficients, where Ursell in 1949 considered oscillating cylinders. Several researchers used Ursell's method in combination with a Lewis transformation to describe more realistic ship cross sections. In 1960 Tasai used multi-parameter conformal mapping where he used two mapping coefficients to represent the ship cross sections even more accurately. These methods are all types of simplifications of the cross-sectional shape of a ship-like cross section, where Frank's method is applicable for any arbitrary cross sectional shape [25].

One of the main drawbacks of the Frank's close-fit method is the presence of irregular frequencies. These frequencies are occurring due to eigenfrequencies of the interior potential problem in the Green's function-integral equation [26]. Investigation into this irregular frequencies is described by Faltinsen, in a study where he used the Frank close-fit method for a cross section oscillating in the higher frequency-range [20]. Faltinsen introduces in his study approximations for both irregular frequencies and asymptotic values in the higher frequency range.

The method of Frank in combination with the approximations of Faltinsen are used for computation of the 2D hydrodynamic mass and damping coefficients. Since the hydrodynamic pressure is calculated on the defined segments along the contour, these pressures could also be used for other calculations. The method of Frank could still be interesting in nowadays problems to define the interaction of a fluid and the oscillating body where the pressure distribution is of interest.

### Hydro-elasticity

Partly or fully submerged bodies are in most cases calculated in two ways; a hydrodynamic and structural analysis. This approximation is valid for stiff structures where the eigenfrequencies of the elastic deflections are higher than the frequencies of the first-order wave loads. When the eigenfrequencies of the elastic deformations are in the range of the first-order wave loads, the interaction between wave radiation and structural modes should be taken into account [53].

The interaction between a (deformable) body inside a fluid domain, is defined as hydro-elasticity of Fluid Structure Interaction (FSI). In hydro-elasticity the laws that describe a fluid should be coupled with the structural mechanics of the body. Hydro-elasticity is significant for interactions between a deformable or moving structure and a surrounding or internal fluid flow [4].

Several methods are used nowadays to describe the moving and deformable bodies embedded in a fluid. In the Lagrangian Eulerian method (ALE) gridpoints on the boundary between the solid body and the fluid are moved in a Lagrangian way. This means that the observation is from the moving object, in this case the fluid-solid interface. The method is easy to implement and has relatively low costs, but for large deformations, the accuracy will decrease. In large deformations or rotations, the mesh of the fluid-solid boundary will become ill-shaped, where the accuracy could be improved by a remesh of this boundary [65].

Another method to describe the hydro-elasticity is the immersed boundary method. In this method the kinematic constraint on the fluid-solid interface is the main driver. This kinematic constraint states that each of the solid points on the interface should be coupled to the fluid velocity at that point. The interaction between the body and the fluid is included by local body forces influencing the velocities in the solid points.

The solid points are interconnected by an elastic law, where the points are combined in a finite difference grid. In contrast to the ALE method, the grid in the immersed boundary method is not changing, but the velocity will be interpolated to meet the kinematic constraint [65].

The fictitious domain method is closely similar to the immersed boundary method. The body is modelled as a field of finite elements. The coupling between the (rigid) body and the fluid is done by a Lagrange multiplier where the constraint is extended to the inner body. The multiplier in weak form represents the body forces. The distribution of forces along the interface is therefore described by an integral formulation [65].

Later on, small adjustments are made to the Extended Immersed Boundary Method and the Immersed Boundary Finite Element Method. In both of these methods the (rigid) body and fluid are described by a different numerical method. Coupling between the finite element method (for the body) and the finite difference or finite volume method (for the fluid) is done by a dirac delta function. The time-integration in both methods is explicit for the interaction of the fluid and the structure [65].

In all of these methods the hydro-elasticity is solved numerically. The interaction between the body and the fluid domain is solved by different methods. In the comparison study of Van Loon [65] the different methods are compared. The comparison is influenced by variations in discretisations, geometry, polynomial order or boundary conditions. In his study he found that the ALE method provides the strongest coupling due to the shared nodes on the solid boundary [65].

An interesting wave energy converter to observe with the close-fit method of Frank is the bulge wave. Wave energy in combination with hydro-elasticity is very important in the analysis of bulge wave systems. An example is the S3 from SBM, which is a slender cylinder of a deformable material floating in the waves. The material is used to transfer energy by the application of Electro Active Polymers [2]. This wave energy converter has an internal power take off and is floating directly beneath the free surface. The tube deforms due to the pressure difference between the fluid inside and outside the tube. A pressure wave, also called the bulge wave, travels along the tube in longitudinal direction. Comparison of the model of this S3 and experiments shows good resemblance of the results, but for short waves some other aspects have to be taken into account than only the deformation of the bulge tube. In her thesis, Floor Spaargaren stated two effects that are significant in the short wave-range. Incident gravity waves excite the S3, but the wave amplitude reduces along the length of the tube and therefore the forces along the tube reduce. These hydromechanical forces are studied in terms of a Froude-Krilov force and a diffraction force. Diffraction of the waves by the tube is shown to depend on the depth of submergence of the tube. The second effect is due to the tube operating directly beneath the free water surface. For shorter wavelengths, the tube isn't following the waves any more and it will behave more like a rigid tube. One of the effects that occur for rigid tubes floating directly beneath the free surface is surface piercing. The effects of surface piercing are approximated by adding a bending moment to the tube and by a decrease of the pressure amplitude for parts where the tube is piercing the surface. The research shows some aspects of a WEC operating in short waves, where the bulge motion of the WEC isn't dominant.

## Deformable bodies

In a wave energy converter like a bulge wave, the energy is interchanged between potential and kinetic energy. The potential energy is the energy in the elastic walls [23]. We assume the tube to be completely filled with water, where the analysis assumes small pressure changes in the tube due to small sea waves [16, 23].

The interaction of the deformation of the tube and the elasticity in the walls of a thin walled cylinder is considered in a two dimensional and axisymmetric structure.

The pressure difference between the inner and outer fluid domain causes a deformation. When an infinitesimal element of the membrane is observed, a force equilibrium can be used to define the relation between normal forces on and the tension in the membrane. The forces are defined in Figure A.3, where  $T$  denotes the tension in the tube's element with length  $dC$ .

The frictional pressure component  $p_t$  can be neglected in the static cases, but also in waves and steady flow since the tangential force is an order of magnitude less than the normal loads on the bulge. This assumption is of importance in the force equilibrium of the small element of the tube wall (with length  $dC$  in tangential direction) [47]:

$$dT + p_t \cdot dC = 0 \rightarrow dT = 0 \quad (\text{A.4})$$

where the tangential tensions along the tube's contour is constant, which is an important observation in

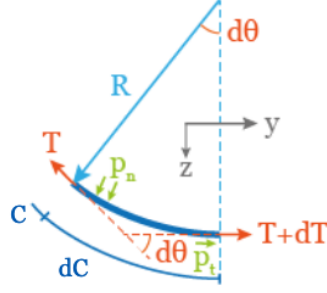


Figure A.3: Definition of the forces working on an element of the tube wall [47]

axisymmetric thin-walled structures (where the ratio radius over wall thickness,  $R/h \geq 10$ ). The combination of Figure A.3 and Equation A.4 will result in an differential equation for the shape of the cross section with respect to the pressure difference between the inner and outer fluid region. Since the element is assumed to be small, the differential equation can be simplified into [47]:

$$\begin{aligned}
 2 \cdot T \cdot \sin\left(\frac{d\theta}{2}\right) - p_n(y, z) \cdot dC &= 0 \\
 2 \cdot T \cdot \left(\frac{d\theta}{2}\right) - p_n(y, z) \cdot dC &\approx 0 \\
 \frac{d\theta}{dC} &= \frac{p_n(y, z)}{T}
 \end{aligned} \tag{A.5}$$

where  $p_n$  is the pressure difference between the inner and outer fluid flow and  $T$  is the tension inside the tube wall ( $T = \sigma_\theta \cdot h$ ), where  $\sigma_\theta$  is the hoop stress in the tube's wall. Equation A.5 could also be expressed in the radius of the tube by rewriting the surface tangent over the element as the radius  $R$  [47].

$$\frac{1}{R} = \frac{p_n(y, z)}{T} = \frac{p_n}{h \cdot \sigma_\theta} \tag{A.6}$$

Which shows that the internal pressure due to the completely filled cylinder causes a circumferential stress inside the (elastic) wall of the tube. For a thin-walled structure (where  $R/h \geq 10$ ) the bulge pressure<sup>3</sup> inside the tube is given by the Young-Laplace equation [31, 60]:

$$p_b = \frac{\sigma_\theta h}{R} \tag{A.7}$$

The material can be described by a Kelvin-Voigt model, where the material is defined by a parallel model of purely viscous damper and a purely elastic spring. Therefore, the equation for the stress in the viscoelastic material can be described by [38, 60]:

$$\sigma_1 = E\varepsilon_h + \eta\dot{\varepsilon}_h = E\left(\varepsilon_h + \beta\frac{\partial\varepsilon_h}{\partial t}\right) \tag{A.8}$$

Where  $E$  is known as the Young's modulus and  $\eta$  is coefficient that accounts for rate of strain, also known as the viscosity [38].  $\varepsilon_h$  represents the strain in the tube's wall due to the hoop stress. From Equation A.8 it follows that  $\beta = \eta/E$ .  $\beta$  corresponds to the energy loss by work done on the tube. Combination of the Equations A.7 and A.8 results in an expression for the bulge wave pressure [60]:

$$p_b = \frac{Eh}{R}\left(\varepsilon_h + \beta\frac{\partial\varepsilon_h}{\partial t}\right) \tag{A.9}$$

The bulge pressure ( $p_b$ ) will be rewritten in terms of a distensibility, which is a measurement for the stretching and compression of the cross-section  $S$  with respect to the pressure inside the cylinder. The distensibility  $D$

<sup>3</sup>We call the bulge pressure  $p_b$ , which is actually the same as the pressure difference as mentioned as  $p_n$ , the pressure component normal to the elastic wall

is given by equation A.10 [23]:

$$D = \frac{1}{S} \frac{dS}{dp_b} = \frac{1}{\pi R^2} \frac{2\pi R}{\frac{Eh}{R^2}} = \frac{2R}{Eh} \quad (\text{A.10})$$

The fluid inside the tube could be described by the Navier-Stokes equations for conservation of mass and conservation of momentum in cylindrical coordinates. Due to axial symmetry, an inviscid fluid and the neglected non-linear terms due to small disturbances, the conservation of mass and momentum reduce to [23, 51, 61]:

$$\frac{\partial S}{\partial t} + \frac{\partial(S \cdot u_x)}{\partial z} = 0 \quad (\text{A.11})$$

$$\frac{\partial u_x}{\partial t} = -\frac{1}{\rho} \frac{\partial p}{\partial z} \quad (\text{A.12})$$

where  $u_x$  is the velocity in longitudinal direction. Since we assume the volume flow to be linear with respect to  $S_s$ , equation A.11 simplifies to [23, 60]:

$$\frac{\partial S}{\partial t} = -S_s \frac{\partial u_x}{\partial z} \quad (\text{A.13})$$

Combination of the equations A.12 and A.13 results in an equation where the velocity in x-direction is eliminated. Furthermore, the cross-sectional area could be approximated by the following expression  $S = S_0(1+2\varepsilon)$  [60], which will be implemented in the Equations A.12 and A.13.

$$\frac{\partial^2 \varepsilon_h}{\partial t^2} = \frac{1}{2\rho} \left( \frac{\partial^2 p_b}{\partial z^2} + \frac{\partial^2 p_w}{\partial z^2} \right) \quad (\text{A.14})$$

where the pressure inside the tube is a summation of the bulge pressure  $p_b$  (due to distention of the elastic tube) and the pressure of the wave outside the tube  $p_w$  [60]. Equation A.14 expresses the strain in terms of the derivatives of the pressure components over the longitudinal axis of the bulge wave energy converter. The Equations A.11 till A.14 are important when the bulge wave energy converter is examined in the three-dimensional case. In this case, another boundary condition should be added for the bulge pressure at the bow of the WEC:

$$\frac{\partial}{\partial z} (p_b + p_w) = 0 \quad (\text{A.15})$$

at  $z = 0$ . At the stern of the bulge wave energy converter should also be a second boundary condition to determine the reflected wave. This reflected wave will cause a backward propagation wave. Since this backward propagation wave decays exponentially, the bulge wave is damped out and the second boundary condition will be neglected in a three-dimensional analysis of the bulge wave energy converter [60].

One of the main drawbacks of a fully rubber tube, is the generation of aneurisms, where the tube's wall becomes unstable and bulge motions will be uncontrollable. In the higher pressure regions, the non-linear characteristics of the material do not meet the linear tension in the rubber anymore. The local thickness of the tube's wall will decrease, due to the Poisson effect of bulge deformations. In this case, the Poisson's ratio should also be included in Equation A.8 [14]. For small pressures there is still an equilibrium point, but at a certain high pressure, aneurisms will be generated [23]. The pressure where these aneurism are generated is given by Chaplin et al. where  $h_s$  and  $R_s$  represent the static values of the wall thickness and tube's radius [14]:

$$p_{crit} = \frac{4Eh_s}{3R_s} \frac{1}{(1 + \alpha_f^{1/2})^2} \quad (\text{A.16})$$

where  $\alpha_f$  states the portion of rubber in the elastic material. So,  $\alpha_f = 1$  for a purely rubber tube [14]. To reduce the generation of aneurisms, the material of the tube could be adapted. Farley et al. state that for a rubber fraction of  $\alpha_f \approx 0.25$  the tendency to form aneurisms may be eliminated [23]. These kind of non-linear effects are neglected in the study, since the material characteristics are assumed to be linear.

### Efficiency of Wave Energy Converters

The energy absorbed by any type of wave energy converter is measured in terms of a capture width (CW). This value is given in equation form:

$$CW = \frac{P_b}{J_W} = \frac{\text{Power absorbed in wave energy device}}{\text{Mean energy per meter width in the sea with wave amplitude } \zeta_I} \quad (\text{A.17})$$

Therefore the capture width is an equivalent width of the wavefront, which energy is absorbed by the wave energy device. Both energy values are the mean during a period of either the wave or the motion of the wave energy device [16, 23, 56]. The capture width of a WEC differs for a wavefrequency, like shown in figure A.4 for the Pelamis. In this figure two capture widths are shown; the force capture width and the power capture width. The force capture width is a measurement for the power absorbed by the WEC with respect to the drift force. The power capture width is the most common measure for energy transport within wave energy converters. If we assume a regular incident wave with wave amplitude  $\zeta_I$  in infinite waterdepth, the mean power per meter of wave front is given by:

$$J_W = \frac{\rho g^2 \zeta_I^2}{4\omega} \quad (\text{A.18})$$

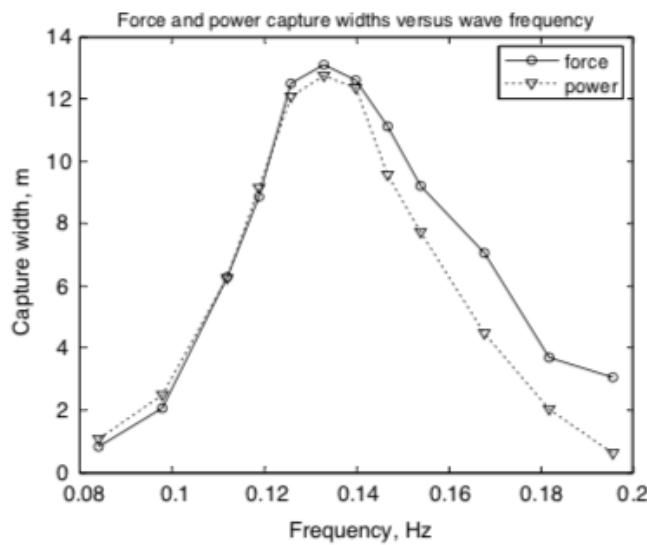


Figure A.4: Force and power capture widths versus wave frequency for WEC (Pelamis) [56]

## A.2. Research questions

In this research the goal is to implement the Frank close-fit method to nowadays' problems, like hydro-elasticity. The Frank close-fit method will be extended/adapted to cope with deformable bodies. The main question in this research is stated as:

**How can Frank's close-fit method contribute to hydro-elasticity in a bulge wave energy converter?**

To answer the main question, three secondary questions are defined to answer the main question. These questions are answered in the Appendices E and F:

1. Which assumptions need to be made to describe a bulge wave energy converter by 2D potential theory?
2. How can Frank's close-fit method be adapted to deal with deformable bodies in still water?
3. How can Frank's close-fit method be adapted to deal with deformable bodies operating in regular waves?

## A.3. Schedule and project approach

The research is divided into four phases, which define the approach of the research topic. These phases are described in Appendix B, including the validation included in this phases.



# B

## Project Approach

This appendix defines how the research will be executed. The predefined steps are evaluated in section B.2.

### B.1. Results

The result of this research will be a model (in Matlab) which is able to define pressure distributions along deformable bodies like a bulge wave energy converter considered in two dimensions. This model will be used for predicting the motions of for example wave energy converters.

In the last decade the interest into wave energy converters as a source of sustainable energy is risen considerably. During this research the model will be applied to a bulge wave energy converter, since the geometry is easy to model. The close-fit method developed in the 70s is used to define the deformation of a bulge wave energy converter.

### B.2. Project steps

The project steps are described in this section. For each phase a table is given, which states the goal, concerned sub questions, planning and deadlines.

#### Phase 0. Implementation of Frank's close-fit method in a Matlab model

The basis of the research is a Matlab model developed during a research assignment about Franks close-fit method [39]. This model calculates the added mass and damping coefficients in a 2D potential flow method. During the research assignment some difficulties are found with respect to the principal value integral in the calculations. Some deviations between the model and validation values are found, which are probable caused by the solver for the potential value integral. The current model should therefore be improved to continue with the steps involved in this research.

<b>Why</b>	To have an accurate model which is the basis of the further developments.
<b>How</b>	Different notes by Faltinsen and others about Frank's paper could help to find the main error in the current Matlab model.
<b>When</b>	This phase will be excused between the 1st os October and the 19th of October, with a total duration of three weeks.
<b>Result</b>	A Matlab model that is accurate to calculate the submerged cylinders which are experimentally tested by Vughts.

#### Validation

The zeroth phase of the research could still be tested with experimental values of an oscillating barge done by Vughts [69] even as the experimental values for an oscillating cylinder (both heave and sway) from Vughts [69].

#### Phase 1. Adapting Frank's close fit method for a bulging cylinder

When the Matlab model is up and running, the adaptations for a bulging cylinder can be made. In this phase we assume the bulge wave energy converter to be a slender cylinder with an finite width. The cylinder has a

circular cross-sections where the walls are deformable. The deformation of the tube is an increase or decrease of radius, where the cross-section remains circular.

In a two-dimensional case we assume the cylinder to expand and contract around a relaxed diameter  $R$ . In this phase of the research we assume a sinusoidal strain with amplitude  $\varepsilon_0$ , given by:

$$\varepsilon_h(t) = \varepsilon_0 \sin \omega t \quad (\text{B.1})$$

Implementation of Equation B.1 results in an expression for the bulge pressure due to sinusoidal strain [23]

$$p_b = \frac{Eh}{R} \varepsilon_0 (\sin \omega t + \beta \omega \cos \omega t) \quad (\text{B.2})$$

This phase identifies the 2D cross section with a time-dependent bulge distortions. Since the strain is defined as:

$$\varepsilon_h = \frac{R - R_s}{R_s} \quad (\text{B.3})$$

Combination of the definition of strain (equation B.3) and the assumed sinusoidal strain of equation B.1 result in a time-dependent radius:

$$R(t) = R_s (1 + \varepsilon(t)) = R_s (1 + \varepsilon_0 \sin \omega t) \quad (\text{B.4})$$

which is shown in Figure B.1. The Matlab model as a result of Phase 0 will be adapted by the kinematic boundary condition. On the moving surface of the tube, the following velocity is required for the fluid [60]

$$\vec{n} \cdot \left( \frac{\partial \Phi}{\partial x}, \frac{\partial \Phi}{\partial y} \right) = \frac{\partial R}{\partial t} \quad (\text{B.5})$$

at  $(z - d)^2 + y^2 = R^2$  (the deformed radius), with  $\vec{n}$  as the normal unit vector pointing into the fluid. Due to constant deformation, the direction of this unit normal vector will remain during one cycle of strain.

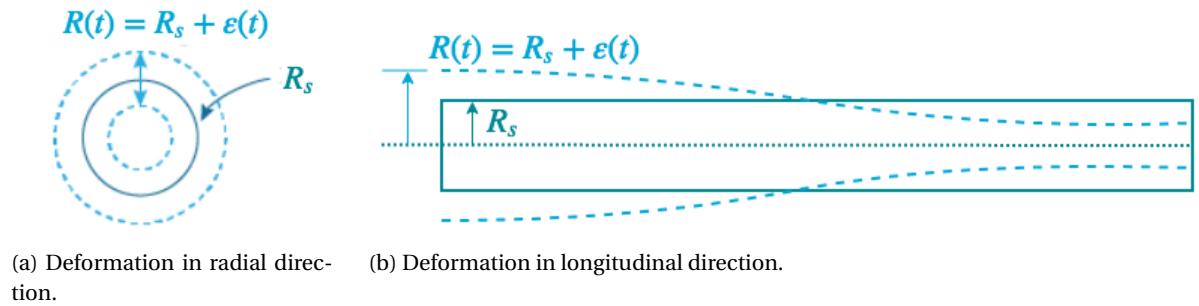


Figure B.1: Deformation of tube due to a prescribed sinusoidal strain ( $\varepsilon_h(t)$ ).

- Why** To have a simple starting point in the distensibility of the cylinder.  
**How** Only a sinusoidal strain is applied, where the oscillation of the bulging is in the radial direction instead of sway heave and roll.  
**Result** An extended Frank close-fit model, which could be checked with the analytical calculations of the equations B.5.  
 During this step an answer could be formulated to secondary question 1.

### Validation

In the first phase, the calculations done by the model are still checkable by analytical formula and boundary conditions. The model in this phase is not yet physically correct, and therefore it is impossible to validate the model in this phase by an experiment.

## Phase 2. Adding the elasticity pressure and deformation part into the model

The influence of the elasticity pressure is described in Appendix A where in the equations A.7 until A.15 the influence of the pressure on deformation of the bulge tube and fluid velocity inside the tube is described. Since the distensibility of the tube is related to the pressure difference and therefore the internal fluid flow, the model should be coupled to the preceding and following cross-section.

In this phase the model is limited to a bulging cylinder in still water, where  $p_w$  (as mentioned in equation A.14) is equal to 0. The bulge pressure due to an oscillating pressure with amplitude  $\rho g B_a$ , where  $B_a$  is the amplitude of the radial deformation. Therefore, the bulge pressure is assumed to be a solution in the form of a wave propagating along the tube [23]:

$$p_b = \rho g B_a e^{-\gamma z} e^{i(\omega t - v_b z)} \quad (\text{B.6})$$

where  $\gamma$  is a coefficient to represent the hysteresis of the tube's material and  $v_b$  is the wavenumber of the oscillating pressure. For small values of  $\gamma$  we can assume the horizontal velocity to be in phase with the bulge pressure.

The main goal of this phase is the investigation of possible solving methods for the pressure, velocity and distensibility problem coupled to the fluids transportation inside the tube. This solving method should also be implemented in the adapted Matlab model.

- Why** Transportation of fluid inside the tube causes extraction and compression of the tube diameter along the tube. This distensibility of the diameter should be modelled in the adapted close-fit method.
- How** Assuming the absence of waves, the pressure inside the tube is only defined by the bulging of the fluid transportation inside the tube.
- Result** A model where the bulge pressure is depending on the distensibility of the bulge tube. Answers secondary question 2.

### Validation

In 1985 Gerrard tested the theory of waves in fluid-filled deformable tubes. At one end of the tube a piston is applying a harmonic motion of the fluid. The oscillating pressure is measured with pressure gauges that were inserted through the tube wall [29]. The different experiments done by Gerrard could be used as a validation of the extended model of phase 2.

## Phase 3. Calculate the addition of incident and diffracted waves

The pressure inside the tube is depending on the incident wave and the bulge pressure, where resonance occurs when the speed of the incident wave matches the natural propagation speed of the bulge waves in the tube [12]. Therefore, we assume an incident linear harmonic wave that causes a pressure:

$$p_w(z, t) = \rho g \zeta_I \cos(\omega t - v z) \quad (\text{B.7})$$

where  $\zeta_I$  is the amplitude of the incident wave,  $\omega$  its angular frequency and  $v$  is known as the wavenumber.

In this phase the tube deformation amplitude  $B_a$  (of phase 2) should be expressed in terms of  $v$ ,  $v_b$  and hysteresis coefficient  $\gamma$ . For wavespeeds outside the resonance frequency region, a phaseshift could be added to relate the tube's deformation and incoming wave speed.

The pressure waves inside the tube are only considered to go in the forward direction by Farley, Rainey and Chaplin [23]. The amplitude of the waves is decreased over the length of the tube due to the power radiated by the bulge tube and diffraction of the waves by the tube. This results in a general formula for the decrease of wave amplitude over length  $d\eta$  [23]:

$$d\eta = \sqrt{\frac{v_b^3}{2\pi}} \cdot e^{v_b d} \cdot \frac{S}{\rho c^2} \frac{dp/dt}{\omega \sqrt{x}} dx \quad (\text{B.8})$$

which holds for incident waves, radiated and diffracted waves with a corresponding frequency. Diffracted and radiated waves from the first elements along the tube, decrease the incident wave amplitude by radiation of

energy. Therefore, the pressure distribution is important to observe along the tube and it should be coupled to the element's position along the bulge. The factor  $e^{v_b d}$  is added to the formula to take the distance of submergence  $d$  into account [23].

The main challenge in this phase is the coupling of the incident, radiated and diffracted waves with the two-dimensional FCFM method. Due to the dimensions of the slender tube, diffraction effects could be neglected, since they are assumed to be small.

- Why** The incident, radiated and diffracted wave do have an impact on the pressure inside the bulge and therefore the transportation of the fluid inside the tube.
- How** First modelling the incident wave and extending it by a amplitude reduction over the length of the tube.
- Result** The result is an extension of the Matlab model where the incident, (diffracted) and radiated wave are implemented (over the length of the bulge tube).  
Phase 3 will investigate a solution to secondary question 3.

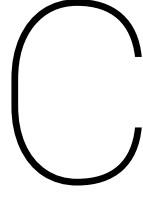
### Validation

In previous work of Chaplin et al. the Anaconda is tested experimentally. These results and assumptions can be used to validate the model without the effects of surface wave diffraction and radiation [14].

### Possible extensions of the model

Several extensions of the models are possible after finishing phase 3 or during the phases 1-3. An impression of the possibilities for a further expansion:

1. Transform the 2D-model into a 3D-model. In this case the application of the Navier-Stokes equations on the distensibility is of importance. As mentioned in phase 2, the moving fluid could be described by the Navier-Stokes equations A.12 and A.13. A Volume-of-Fluid method could be used to model the transportation of fluid through the bulge tube. An extension like the application of a numerical solver for the 3D fluid transportation problem would result in an iterative solver, where computational time will increase.
2. Model the application of a hinged barge and validate with the results of Newman [53]. In this case the body is deformable in the hinge axis by the rigid body translation and rotation of the two barges. This could be possible to calculate with the adapted Frank's close-fit method by a few adaptations to the model. Investigation in this problem, should enlarge the application of the adapted Frank's close-fit model.
3. Model the application of 'The Ocean Cleanup', where pressures and currents cause rotations of the body. The screen beneath the floating barrier will deform in 3D and the total system (barrier and screen) will rotate due to currents.



# Franks Close Fit Method

## C.1. Assumptions and boundary conditions

The Frank Close Fit Method is a solving method for an arbitrary object oscillating in or below the free surface. The method is based on an object in a 2D domain where linear behaviour is assumed. The flow around the object is described by potential theory, where [26, 39]:

1. the fluid is incompressible and inviscid, which means that the density  $\rho = \text{constant}$  and the viscosity  $\mu = 0$  everywhere in the fluid domain.
2. the effects of surface tension are negligible.
3. the fluid flow is irrotational;  $\boldsymbol{\omega} = \frac{\partial u}{\partial x} - \frac{\partial v}{\partial y} = 0$
4. the motion amplitudes and velocities are small enough, so that all but the linear terms of the free surface condition, the kinematic boundary condition on the cylinder, and the Bernoulli equation may be neglected.

Since the problem is in 2D, a complex variable can be used to describe the velocity field. Any point in this domain can be described by a complex variable  $z = x + i \cdot y = r e^{i\theta}$  [42]. In potential theory the fluid can be described by a (complex) potential  $F(z)$  [52]:

$$F(z) = \phi + i \cdot \psi \quad (\text{C.1})$$

where  $\phi$  is the velocity potential and  $\psi$  is the streamfunction. The velocity components can be determined by differentiating either the velocity potential or the streamfunction as given by the *Cauchy-Riemann equations* [42, 52]:

$$u = \frac{\partial \phi}{\partial x} = \frac{\partial \psi}{\partial y} \quad v = \frac{\partial \phi}{\partial y} = -\frac{\partial \psi}{\partial x} \quad (\text{C.2})$$

These velocity components are part of the complex velocity  $W$ . The complex velocity is defined as the derivative of the complex potential  $F$ , which is an analytic function of the complex variable  $z$  [42, 52]:

$$\frac{dF(z)}{dz} = W(z) = u - i \cdot v \quad (\text{C.3})$$

where in the previous equations the imaginary unit  $i$  refers to the space-complex potential components. The total potential is also complex in time, for example the velocity potential<sup>1</sup> [66]:

$$\Phi(z, t) = \text{Re}_{I,J} \left\{ \phi(z) \cdot e^{-j\omega t} \right\} \quad (\text{C.4})$$

where  $\omega$  is the frequency of oscillation. In equation C.4 the time-dependency is added by  $\exp(-j\omega t)$ . The velocity potential should be real in both space and time, where the subscript 'I,J' in equation C.4 shows that

<sup>1</sup>The choice for the exponent in the time-dependence is quite strict with respect to other related formulations, for example for the velocity in normal direction and the Green's function. Van 't Veer choose the exponent with  $j \cdot \omega t$  [66], while Frank and Lee et al. choose for  $-j \cdot \omega \cdot t$  [26][43]. In this report the time-dependency is based on the conventions of Frank and Lee et. all.

the potential is real with respect to both complex units  $i$  and  $j$ . The complex unit  $i$  refers to the space-complex variables and  $j$  refers to complex analysis in the time-domain<sup>2</sup>. The time-dependency of the velocity potential is most of the time not included in the derivations in this report, since a frequency-based analysis is performed. If time-dependency is important, the exponent term will be included again.

As long as we assume a linear behaviour in the 2D potential theory, boundary conditions reduce to be linear. The boundary conditions for the time-dependent velocity potential remain the same for the space-dependent velocity potential and therefore we continue with a space-dependent velocity potential [37]. This space-dependent velocity potential has to fulfil the following linear boundary conditions [26, 39]:

- **Continuity:** Since mass has to be conserved in any chosen domain below the free surface around the body. This equation is also called the 'Continuity equation' or 'Laplace's equation':

$$\Delta\phi = \nabla^2\phi = 0 \quad (\text{C.5})$$

- **Free surface:** A (linearized) boundary condition is given at the free surface; this kinematic boundary condition stating that the normal velocity of any fluid particle at the free surface should have the same velocity as the velocity of the surface in the normal direction. In combination with the dynamic boundary condition a linearized form of this equation is given [18, 43]:

$$\phi_y(z) - v \cdot \phi(z) = 0 \quad (\text{C.6})$$

where the subscript means that it is the derivative with respect to  $y$  of the space-dependent potential and  $v = \frac{\omega^2}{g}$  is the wavenumber.

- **Bottom:** At the (sea)bottom, the fluid is not able to penetrate through the bottom. In the case of an infinitely deep fluid, this boundary condition is described as:

$$\lim_{y \rightarrow -\infty} |\nabla\phi^{(m)}| = 0 \quad (\text{C.7})$$

- **Object's boundary:** On the surface between the fluid and the structure a kinematic boundary condition is defined:

$$\vec{n} \cdot \nabla\phi = v_n \quad (\text{C.8})$$

where the left term refers to the velocity of the fluid in normal direction and the right side defines the velocity of the structure in normal direction.

- **Far away from the structure,** a radiation condition is formulated. This condition states that waves generated by the object will vanish far away from the object [18].

## C.2. Geometry description

The straight-line elements are defined by  $N+1$  points defined on the submerged contour, which are represented by the complex variable  $c_i = a_i + i \cdot b_i$ . The subscript  $i$  refers to the  $i$ -th point along the contour, only panelled in the fourth quadrant of the complex plane for symmetrical submerged contours. For asymmetric body contours, the submerged sections should be panelled in total. Figure C.1 shows an example of a circular cross section with 4 panels.

The velocity and pressure components will be derived in the midpoints of each segment, these positions are defined by complex variable  $z_i = x_i + i \cdot y_i$ . In these midpoints, the subscript  $i$  refers to the  $i$ -th segment along the contour. In this part index  $i$  used, but later a second index  $j$  is used to determine the interaction between two elements or points.

The midpoints of each element are defined by linear interpolation:

$$x_i = \frac{a_i + a_{i+1}}{2} \quad y_i = \frac{b_i + b_{i+1}}{2} \quad (\text{C.9})$$

For each element an angle with the x-axis, where  $\alpha$  is defined to be positive for the counter-clockwise direction.

$$\alpha_i = \arctan\left(\frac{b_{i+1} - b_i}{a_{i+1} - a_i}\right) \quad (\text{C.10})$$

<sup>2</sup>The complex units  $i$  and  $j$  are separated by Faltinsen, to clarify the equations of Frank. The complex units  $i$  and  $j$  do not interact with each other, which is an important note for numerical implementation of the Frank Close Fit Method

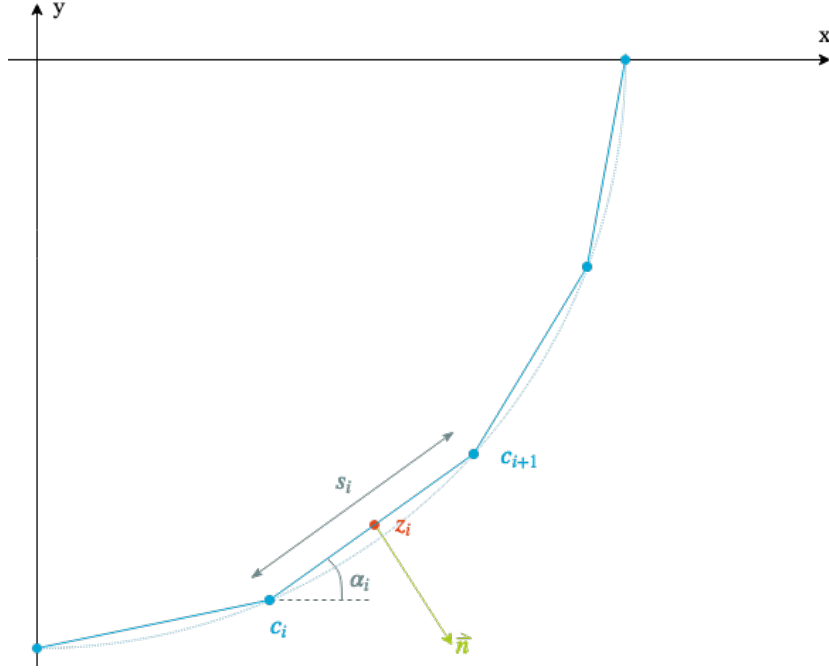


Figure C.1: Geometry descriptions as defined by Frank [26]

where the special points are defined as:

$$\alpha_i = \begin{cases} \frac{\pi}{2} & \text{if } a_{i+1} - a_i = 0 \text{ and } b_{i+1} - b_i > 0 \\ -\frac{\pi}{2} & \text{if } a_{i+1} - a_i = 0 \text{ and } b_{i+1} - b_i < 0 \\ 0 & \text{if } b_{i+1} - b_i = 0 \text{ and } a_{i+1} - a_i > 0 \\ \pi & \text{if } b_{i+1} - b_i = 0 \text{ and } a_{i+1} - a_i < 0 \end{cases} \quad (\text{C.11})$$

Since each element has a starting point and an end point, the length of each element is calculated according to equation C.12:

$$|s_i| = \sqrt{(a_{i+1} - a_i)^2 + (b_{i+1} - b_i)^2} \quad (\text{C.12})$$

### C.3. Solving method

In the Franks Close Fit method (FCFM) the submerged contour of the object is divided into  $N$  straight-line segments, where on each segment a continuous distribution of sources<sup>3</sup> is smeared out to represent the flow induced by the motion of body [40, 52]. The density of the sources is unknown and will be determined by applying the kinematic boundary condition to the submerged body contour [26]. The kinematic boundary condition is applied to the complex potential, which will be defined first. The velocity potential is given by the relation between a pulsating source and the Green's function. The Green's function (also called influence function) defines the influence of a pulsating source in point  $\zeta$  on the potential in point  $z$ . The Green's function is satisfying all boundary conditions except for the kinematic boundary condition on the bodies contour [37]. The velocity potential is described by:

$$\phi(z) = \text{Re}_I \left\{ \int_{C_0} Q(\zeta) G(z, \zeta) dC \right\} \quad (\text{C.13})$$

where  $C_0$  denotes the submerged contour of the body,  $Q(\zeta)$  the source distribution and  $G(z, \zeta)$  the Green's function. This velocity should be real in the space-complex analysis, since Equation C.4 should be real in both time and space complex planes.

<sup>3</sup>These sources could also be sinks, when the strenght of the source is negative. For simplicity, sources and sinks are both called sources in this thesis, where the value defines the source to be a source or a sink.

For the numerical model the submerged contour is composed of  $N$  straight-line elements denoted by  $j = 1, 2, \dots, N$ . Therefore the equation C.13 is transformed into [43]:

$$\phi(z) = \text{Re}_I \left\{ \sum_{j=1}^N \int_{C_j} Q(\zeta) G(z, \zeta) dC \right\} \quad (\text{C.14})$$

When it is assumed that the elements are small enough, the source distribution will be constant on each segment. The definition for the velocity potential is simplified into [43]:

$$\phi(z) = \sum_{j=1}^N Q_j \cdot \text{Re}_I \left\{ \int_{C_j} G(z, \zeta) dC \right\} \quad (\text{C.15})$$

where the source strength of each element is basically the integration of the source distribution over the segments' length. This is shown in Figure C.2.

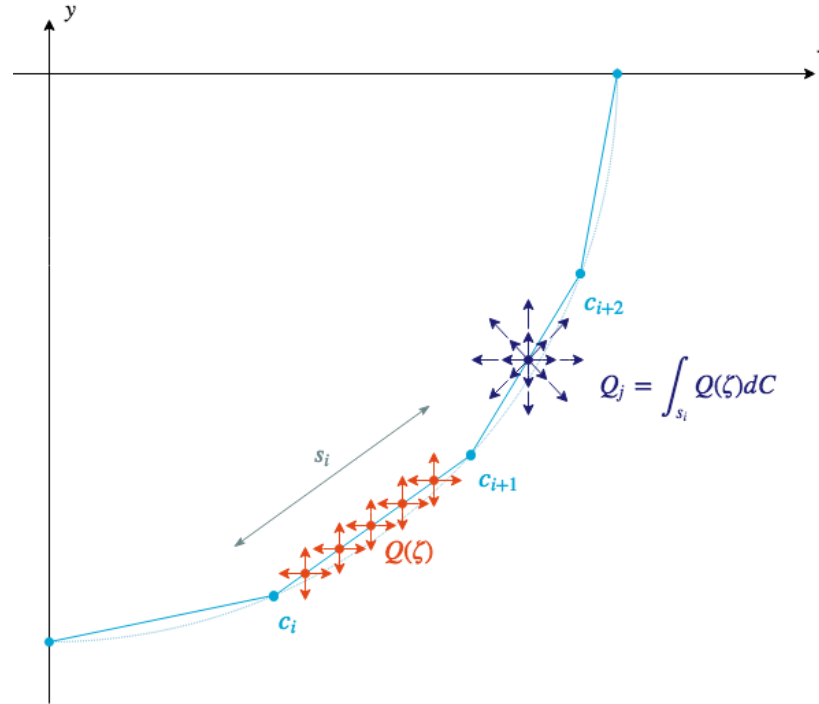


Figure C.2: Continuous source distribution discretised into a single source strength for an element.

The source strength  $Q_j$  of Equation C.15 is still unknown, but can be found by the other components of Equation C.15. The Green's function for a pulsating source is determined by Wehausen and Latoine [26, 43, 70], where the position variable  $\zeta$  along the contour is changed into variable  $c$  to simplify the equations:

$$G(z, c) = \frac{1}{2\pi} \left[ \log(z - c) - \log(z - \bar{c}) + 2PV \int_0^\infty \frac{e^{-ik(z - \bar{c})}}{v - k} dk \right] - j \cdot e^{-iv(z - \bar{c})} \quad (\text{C.16})$$

In this equation the  $\bar{c}$  is the complex conjugate of  $c$  and it is representing the same point but on the reflected body (see Figure C.3). Therefore, the second term in Green's function fulfils the free surface boundary condition (which is in this case the still water free surface).  $v = \frac{\omega^2}{g}$  is representing the wavenumber of an oscillatory motion of a body in deep water.

The third and fourth terms are the result of a singularity in the integration along the segments. The complex variable  $z$  could be any point inside the fluid domain, but when this variable is very close to the source distribution an improper integral is found. Since the total source strengths of the elements are represented in the midpoints of the panels (at  $z_i$ ), integration along the segments will result in a pole at the point  $c = z$ .

Such a pole should be avoided, since integrals are not proper anymore. Therefore the path of integration is splitted in a principal value integration along the real axis of the contour and a half of the residual term in the singularity point [32, 52]. In these terms, the calculation of the fourth term is straight forward, but the third term has to be rewritten into [30, 43]

$$PV \int_0^{\infty} \frac{e^{-ik(z-\bar{c})}}{v-k} dk = e^{-iv(z-\bar{c})} \cdot (-E1[iv(z-\bar{c})] - i\delta\pi) \quad (C.17)$$

Where E1() is the exponential integral as defined by Abramowitz and Stegun [28]. The value for  $\delta$  is depending on the integral path, defined for the argument of the exponential integral [33, 43]:

$$\delta = \begin{cases} 1, & \text{for } \text{Im}_I(-iv(z-\bar{c})) < 0 \\ -1, & \text{for } \text{Im}_I(-iv(z-\bar{c})) \geq 0 \end{cases} \quad (C.18)$$

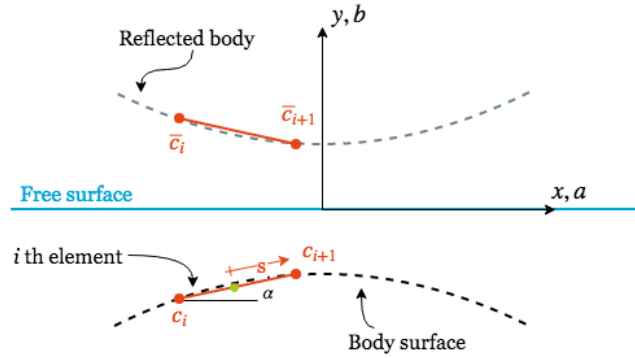


Figure C.3: Definition of the surface source element and its reflected element (based on [30]).

All of the terms in the Green's function are defined, where two imaginary units  $i$  and  $j$  are used to refer to the space-complex (unit  $i$ ) or time-complex parts (unit  $j$ ).

The given Green's function will be implemented in the definition of the velocity potential of Equation C.15. The integration over the submerged panels will result in:

$$\begin{aligned} \phi(z) = & \sum_{j=1}^N Q_j \cdot \text{Re}_I \left\{ \frac{1}{2\pi} \cdot \left[ e^{-i\alpha_j} \cdot ((z_i - c_{j+1}) - (z_i - c_{j+1})) \cdot \log(z_i - c_{j+1}) - (z_i - c_j) + (z_i - c_j) \cdot \log(z_i - c_j) \right] \right. \\ & - e^{i\alpha_j} \cdot ((z_i - \bar{c}_{j+1}) - (z_i - \bar{c}_{j+1})) \cdot \log(z_i - \bar{c}_{j+1}) - (z_i - \bar{c}_j) + (z_i - \bar{c}_j) \cdot \log(z_i - \bar{c}_j) \\ & + 2 \cdot \frac{-ie^{i\alpha_j}}{v} \cdot \left( \log(z_i - \bar{c}_j) - \log(z_i - \bar{c}_{j+1}) + PV \int_0^{\infty} \frac{e^{-ik(z_i - \bar{c} - j + 1)}}{v - k} dk - PV \int_0^{\infty} \frac{e^{-ik(z_i - \bar{c} - j)}}{v - k} dk \right) \\ & \left. - j \cdot \frac{-ie^{-i\alpha_j}}{v} \cdot \left( e^{-iv(z_i - c_{j+1})} - e^{-iv(z_i - c_j)} \right) \right\} \\ = & \text{CU}(i, j) \end{aligned} \quad (C.19)$$

With the definition of the velocity potential (of Equation C.19), there is still one boundary condition that is not satisfied yet. The kinematic boundary condition on the surface of the body will be satisfied by the source distribution over the surface. This kinematic boundary condition is a tool to determine this unknown source density over the elements.

Substitution of the time-dependent velocity potential into the kinematic boundary condition results in Equation C.20. The right-hand side of this equation shows the real part with respect to complex unit  $i$ , which refers to the complex analysis in space. The complex unit  $j$  in this equation refers to the time-complex character of the oscillation.

$$\vec{n} \cdot \nabla \Phi = \text{Re}_I \left\{ \sum_{j=1}^N Q_j (\vec{n} \cdot \nabla) \int_{C_j} G(z, c) dC \cdot e^{-j\omega t} \right\} = v_n \quad (C.20)$$

where  $v_n$  is the component of the forced velocity of the cylinder in normal direction. The definition of  $v_n$  is depending on the motion (with normal vector  $\vec{n}$ ) and on the definition of the forced oscillatory motion.

The oscillatory motion applied by Frank and the corresponding velocity component  $v_n$  is given in Table C.1, where a complex notation<sup>4</sup> is added in the third column.

	Real method of analysis	Complex method of analysis
forced oscillatory motion	$\Theta^{(m)} = A^{(m)} \cdot \cos(\omega t)$ $= \text{Re}_J \left\{ A^{(m)} \cdot e^{-j\omega t} \right\}$	$\Theta^{(m)} = A^{(m)} \cdot e^{-j\omega t}$
component of the forced velocity of the cylinder in normal direction	$v_n^{(m)} = -A^{(m)} \cdot \omega \cdot \sin(\omega t) \cdot n_i^{(m)}$ $= \text{Re}_J \left\{ -j \cdot A^{(m)} \cdot \omega \cdot e^{-j\omega t} \right\} \cdot n_i^{(m)}$	$v_n^{(m)} = -j \cdot A^{(m)} \cdot \omega \cdot e^{-j\omega t} \cdot n_i^{(m)}$

Table C.1: Forced oscillation and forced velocity components in two different methods of analysis.

where the velocities are based on the directional cosines [26]:

$$n_i^{(m)} = \begin{cases} -\sin(\alpha_i), & \text{for sway (m = 2)} \\ \cos(\alpha_i), & \text{for heave (m = 3)} \\ (y_i - y_0) \cdot \sin(\alpha_i) + x_i \cdot \cos(\alpha_i), & \text{for roll (m = 4)} \end{cases} \quad (\text{C.21})$$

Since the boundary conditions are applicable to both the time-depending and time-independing velocity potential, the kinematic boundary condition can be simplified by omitting  $e^{-j\omega t}$ . Equation C.20 reduces into[66]:

$$\text{Re}_I \left\{ \sum_{j=1}^N Q_j (\vec{n} \cdot \nabla) \int_{C_j} G(z, c) dC \right\} = -j \cdot A^{(m)} \cdot \omega \cdot n_i^{(m)} \quad (\text{C.22})$$

The left hand side of Equation C.22 is the combination of the unknown  $Q_j$  and the influence matrix, which is given in Equation C.23.

$$\begin{aligned} \text{Re}_I \left\{ (\vec{n} \cdot \nabla) \int_{C_j} G(z, c) dC \right\} &= \frac{1}{2\pi} \cdot \text{Re}_I \left\{ i e^{i(\alpha_i - \alpha_j)} \cdot (\log(z_i - c_{j+1}) - \log(z_i - c_j)) \right. \\ &\quad - i e^{i(\alpha_i + \alpha_j)} \cdot (\log(z_i - \bar{c}_{j+1}) - \log(z_i - \bar{c}_j)) \\ &\quad \left. + 2 \cdot i e^{i(\alpha_i + \alpha_j)} \cdot \left( PV \int_0^\infty \frac{e^{-ik(z_i - \bar{c}_{j+1})}}{v - k} dk - PV \int_0^\infty \frac{e^{-ik(z_i - \bar{c}_j)}}{v - k} dk \right) \right\} \\ &\quad - j \cdot \text{Re}_I \left\{ i e^{i(\alpha_i + \alpha_j)} \cdot (e^{-iv(z_i - c_{j+1})} - e^{-iv(z_i - c_j)}) \right\} \\ &= \text{CB}(i, j) \end{aligned} \quad (\text{C.23})$$

In the numerical analysis of Frank's Close Fit Method the position coordinates  $z$  and  $c$  are defined over the panels. Since the Green's function determines the influence between these points, the variable  $z$  is defined on the  $i$ -th panel and  $c$  is defined on the  $j$ -th panel. These indices are different from the previous mentioned imaginary units and are always represented in the equations and figures as subscript. The index  $i$  is used for variables defining the panel which is influenced by panel  $j$ . As an example, the source strengths are always inducing flow, so they always have the index  $j$ . Since Equation C.23 consist of both indices, this equation defines the influence of each pulsating source on an element and is therefore a square matrix in the numerical model. This matrix is called  $A$ , where the right-hand side of Equation C.22 is given in the columnvector  $B$ . The complex source strengths  $Q_j$  are found by the matrix equation:

$$[A] \{Q\} = \{B\} \Rightarrow \{Q\} = [A] \setminus \{B\} \quad (\text{C.24})$$

<sup>4</sup>In the complex method of analysis, all the parts of the potential, velocity and influence coefficients stay complex. When the potential is solved, the real parts are used to transform from a complex method into real method of analysis.

where

$$\{Q\} = [Q_1 \quad Q_2 \quad \dots \quad Q_N] \quad \text{and} \quad \{B\} = \begin{bmatrix} -j \cdot A^{(m)} \cdot \omega \cdot n_1^{(m)} \\ -j \cdot A^{(m)} \cdot \omega \cdot n_2^{(m)} \\ \vdots \\ -j \cdot A^{(m)} \cdot \omega \cdot n_N^{(m)} \end{bmatrix} \quad (\text{C.25})$$

The Equations C.19 and C.23 are calculated for a symmetric and asymmetric body. In the case of a symmetric body, less calculations have to be carried out to get the same results. Calculations of the coefficients of half of the body have to be done and a transformation into the left ('image') part of the body, is enough to get valid results. An example of this transformation is given in Appendix D, Section D.6.

The calculated values of  $Q_j$  (of Equation C.25) can be substituted into the velocity potential, which is of importance for the pressure calculation. Pressure can be defined on each element of the submerged contour of the body by the linearised Bernoulli equation [26]:

$$\begin{aligned} p^{(m)}(z_i, \omega) &= -\rho \cdot \frac{\partial \Phi^{(m)}(z_i, \omega)}{\partial t} \\ &= -\rho \cdot \text{Re}_J \left\{ \sum_{j=1}^N Q_j \cdot \left( \frac{1}{2\pi} \text{Re}_I \int_{C_j} \left[ \log(z-c) - \log(z-\bar{c}) + 2PV \int_0^\infty \frac{e^{-iv(z-\bar{c})}}{v-k} dk \right] dC \right. \right. \\ &\quad \left. \left. - j \cdot \text{Re}_I \int_{C_j} e^{-iv(z-\bar{c})} dC \right) \cdot -j\omega \cdot e^{-j\omega t} \right\} \\ &= -\rho \cdot \text{Re}_J \left\{ \sum_{j=1}^N Q_j \cdot \left( \frac{1}{2\pi} (-j\omega) \text{Re}_I \int_{C_j} \left[ \log(z-c) - \log(z-\bar{c}) + 2PV \int_0^\infty \frac{e^{-iv(z-\bar{c})}}{v-k} dk \right] dC \right. \right. \\ &\quad \left. \left. - \omega \cdot \text{Re}_I \int_{C_j} e^{-iv(z-\bar{c})} dC \right) e^{-j\omega t} \right\} \\ &= +\rho \cdot \omega \cdot \text{Re}_J \left\{ \sum_{j=1}^N Q_j \cdot \left( \frac{1}{2\pi} (j) \text{Re}_I \int_{C_j} \left[ \log(z-c) - \log(z-\bar{c}) + 2PV \int_0^\infty \frac{e^{-iv(z-\bar{c})}}{v-k} dk \right] dC \right. \right. \\ &\quad \left. \left. + \text{Re}_I \int_{C_j} e^{-iv(z-\bar{c})} dC \right) e^{-j\omega t} \right\} \end{aligned} \quad (\text{C.26})$$

which is the definition of the time-dependent force located at the midpoint of the elements. The blue parts of the pressure definition refer to the time-dependency, which is important in the definition of the hydrodynamic coefficients in Equation C.28. The integration of this pressure over the segments, will result in the total force on the submerged body ( $F_R^{(m)}$ ). This force is calculated according to [37]:

$$\begin{aligned} F_R^{(m)}(\omega) &= - \int_{C_o} p^{(m)}(z_i, \omega) \cdot \vec{n} \cdot dC \\ &= - \sum_{i=1}^N p_i^{(m)}(z_i, \omega) \cdot n_i^{(m)} \cdot |s_i| \end{aligned} \quad (\text{C.27})$$

The added mass and fluid damping are defined according to the force and applied oscillation [43]. The real components in the time-complex pressure definition are collected, as well as the imaginary components where the resulting values are transformed into:

$$\begin{aligned} F_R^{(m)}(\omega) &= -a^{(m)} \cdot \dot{s}^{(m)} - b^{(m)} \cdot \ddot{s}^{(m)} \\ &= a^{(m)} \cdot \omega^2 \cdot A^{(m)} \cdot e^{-j\omega t} + b^{(m)} \cdot j \cdot \omega \cdot A^{(m)} \cdot e^{-j\omega t} \end{aligned} \quad (\text{C.28})$$

where the first term is in phase with the velocity of the oscillating cylinder and the second term is related to the acceleration (or displacement) of the cross-section.

So the added mass and fluid damping forces can be solved by the Equations C.26, C.27 and C.28:

$$\begin{aligned} a^{(m)} &= \frac{\rho \cdot \omega}{\omega^2 \cdot A^{(m)}} \sum_{i=1}^N \text{Re}_J \left\{ \sum_{j=1}^N Q_j \cdot \text{Re}_I \int_{C_j} e^{-iv(z-\bar{c})} \cdot \vec{n} \cdot n_j^{(m)} \cdot dC \right\} \\ b^{(m)} &= \frac{\rho \cdot \omega}{\omega \cdot A^{(m)}} \sum_{i=1}^N \text{Re}_J \left\{ \sum_{j=1}^N Q_j \cdot \frac{1}{2\pi} \cdot \text{Re}_I \int_{C_j} \left[ \log(z-c) - \log(z-\bar{c}) + 2PV \int_0^\infty \frac{e^{-iv(z-\bar{c})}}{v-k} dk \right] \cdot n_j \cdot dC \right\} \end{aligned} \quad (\text{C.29})$$

### Non-dimensional analysis

Since the hydrodynamic coefficients depend on the geometry characteristics and frequencies, the results will be rewritten into non-dimensional variables to compare the results with experimental values. Experiments with various cross-sections are carried out by Vugts, who introduced non-dimensional variables as given in Table C.2. The results of Frank are shown by different non-dimensional variables. Frank's non-dimensional definitions are also stated in Table C.2. The last definitions of non-dimensional analysis are given by Van 't Veer in his FORTRAN routine called ASAP (A Seakeeping Analysis Program). Small differences between the definition of this non-dimensional results have to be obtained during validation and verification of the FCF model.

Unit	Mode of motion	Vugts [69]	Frank [26]	Van 't Veer [66]
Frequency $\omega$	m = 2		$\frac{\omega^2 T}{g}$	
	m = 3	$\omega \cdot \sqrt{\frac{B}{2 \cdot g}}$	$\frac{\omega^2 B}{2 \cdot g}$	$\omega^2 \frac{B}{2 \cdot g}$
	m = 4		<i>not defined</i>	
Added mass $a$	m = 2		$\frac{a^{(2)}}{\rho \omega S_s}$	
	m = 3	$\frac{a^{(m)}}{\rho S_s}$	$\frac{a^{(3)}}{\rho \omega S_s}$	$\frac{a^{(m)}}{\rho S_s}$
	m = 4	$\frac{a^{(4)}}{\rho S_s B^2}$	<i>not defined</i>	$\frac{a^{(4)}}{\rho S_s B^2}$
Damping $b$	m = 2		$\frac{b^{(2)}}{\rho \omega S_s}$	
	m = 3	$\frac{b^{(m)}}{\rho S_s} \cdot \sqrt{\frac{B}{2 \cdot g}}$	$\frac{b^{(3)}}{\rho \omega S_s}$	$\frac{b^{(m)}}{\rho S_s} \omega$
	m = 4	$\frac{b^{(4)}}{\rho S_s B^2} \cdot \sqrt{\frac{B}{2 \cdot g}}$	<i>not defined</i>	$\frac{b^{(4)}}{\rho S_s B^2} \cdot \omega$
Wave force amplitude $F_{wa}$	m = 2	$\frac{F_{wa}}{\rho g v \cdot S_s}$	<i>not scaled</i>	<i>not scaled</i>
	m = 3	$\frac{F_{wa}}{\rho g B}$	<i>not scaled</i>	<i>not scaled</i>
	m = 4	$\frac{12 \cdot F_{wa}}{\rho g v \cdot B^3}$	<i>not defined</i>	<i>not scaled</i>

Table C.2: Non-dimensional definitions of Vugts [69], Frank [26] and Van 't Veer [66] for circular and rectangular cross sections.

## C.4. Results

The solving method is modelled in Matlab, where two different geometries are tested:

- Circular cross-section
- Rectangular cross-section

Both of these cross-sections are experimentally tested by Vugts [69] and numerically solved by Frank [26]. Both non-dimensionalized the results in a different manner. These non-dimensional definitions are given in Table C.2.

The results of the Frank Close Fit method are plotted in Figure C.4a until C.4d, together with the experimental values found by Vugts [68] and the numerical values found by Liu [46]. In Figures C.5a until C.5d three width over depth ratio's are plotted, since Vugts tested these cross-sections as well. All of the values are non-dimensionalised by the definitions of Vugts [68].

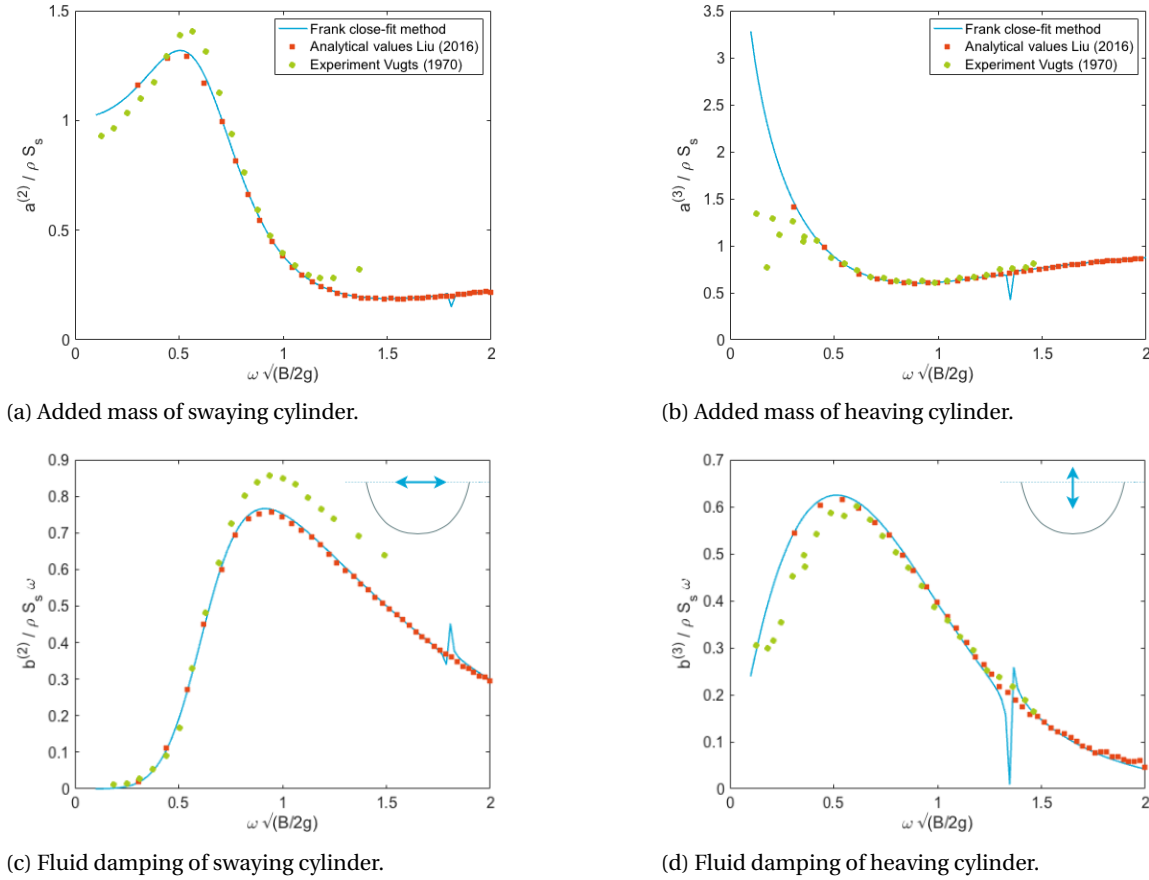


Figure C.4: Hydrodynamic coefficients of floating cylinder compared with analytical values found by Liu et al. [46] and experimental values obtained by Vugts [68].

The Frank Close Fit method is also able to calculate the hydrodynamic coefficients for fully submerged cross section [26]. Frank only verified the results of a circular cylinder in heave at an axis of submersion of  $1.25R$ . The results of this configuration are shown in Figure C.6b. Added mass and fluid damping are in this case non-dimensionalised as shown in the figure. These non-dimensionalised values are resulting from Equation C.28, where  $M^{(3)}$  and  $N^{(3)}$  are related to the total force:

$$F^{(3)}(\omega) = -M^{(3)} \cdot e^{-j\omega t} - N^{(3)} \cdot j \cdot e^{-j\omega t} \quad (C.30)$$

The non-dimensional values should be transformed into non-dimensional coefficients, depending on frequency, fluid density, amplitude of oscillation and cross-sectional area. Since the cross-section is the submerged cross-section, the non-dimensional coefficient differs from the coefficient given in Table C.2. The

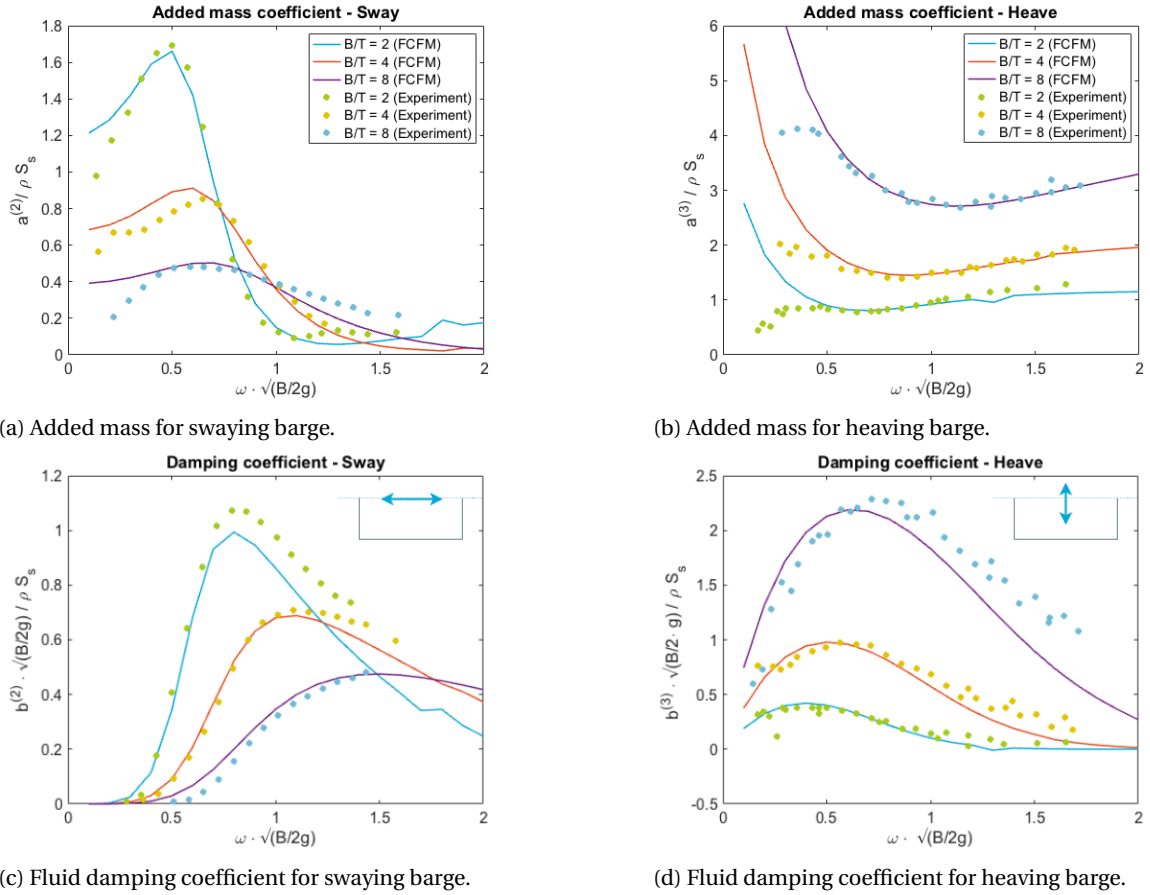


Figure C.5: Hydrodynamic coefficients of floating barge compared with experimental values obtained by Vugts [68].

transformation of the added mass and fluid damping forces into coefficients is similar to Equation C.29:

$$a^{(3)} = \frac{M^{(3)}}{\omega^2 \cdot A^{(3)}}, \quad b^{(3)} = \frac{N^{(3)}}{\omega \cdot A^{(3)}} \quad (C.31)$$

The results of Figure C.6b are non-dimensionalised as:

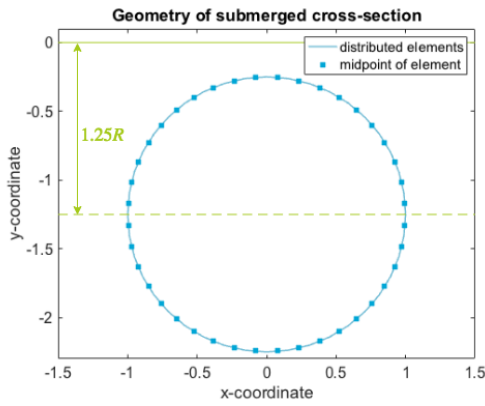
$$a^{(3)'} = \frac{a^{(3)}}{\rho \cdot S_s}, \quad b^{(3)'} = \frac{b^{(3)}}{\rho \cdot S_s \cdot \omega} \quad (C.32)$$

This non-dimensional coefficients from Equation C.31 and C.32 are given in Figure C.6b for added mass and fluid damping in heave. For smaller depths of submergence ( $R/d < 1.25$  as shown in Figure C.6a) no verified data is found, and for very small depths physical incorrect results are found. For  $R/d = 1.0$  and  $R/d = 1.1$  negative values for added mass and fluid damping are found. Possible explanations for these negative coefficients are given as:

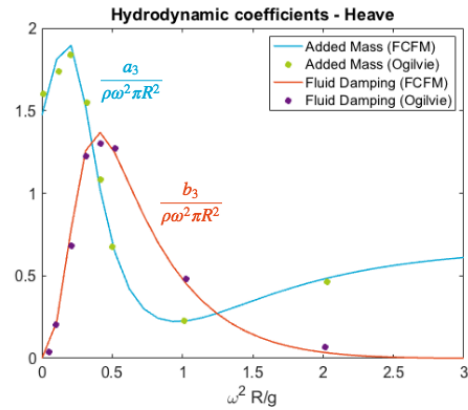
- The free surface is non-linear and therefore the assumption of a linearised free surface boundary condition is not valid anymore.
- The water above the submerged cylinder behaves similar to waves travelling in waters of small depth. Therefore the wavenumber changes since the dispersion relation is given as  $\omega^2 = gv \tanh(vd)$  for waters with small depth [34]. For very small depths, the waves generated will break which is still poorly understood in coastal engineering [34]. These effects are both not included in the FCFM, since they are (directly or indirectly) depending on the waterdepth above the submerged cylinder.

Larger depths of submergence are shown in Figure C.7 for cylinders in heave and sway motion. Remarkable is the similarity between the added mass and fluid damping behaviour of sway and heave motion. This implies

that hydrodynamic coefficient of a submerged cylinder at  $d/R = 1.5$  are both influenced by the free surface for the same amount.

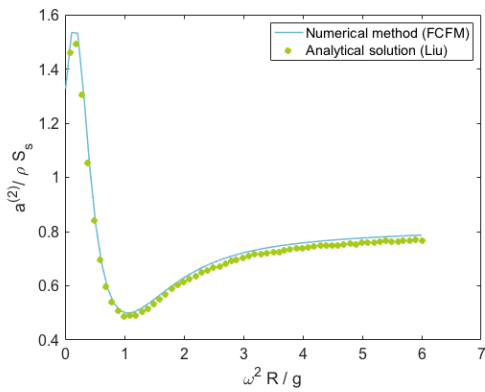


(a) Geometry of submerged cylinder

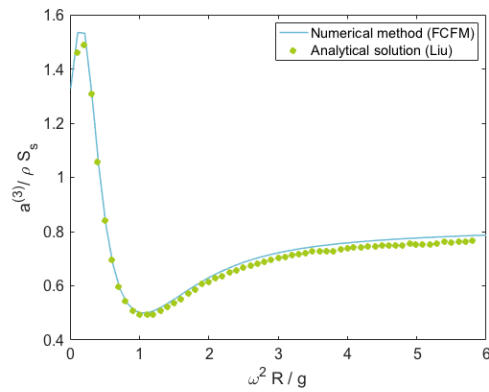


(b) Hydrodynamic coefficients of submerged cylinder

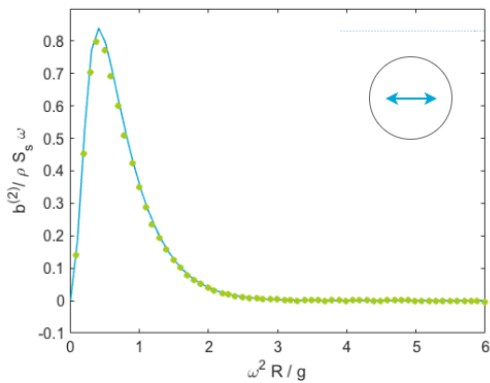
Figure C.6: Geometry (C.6a) and hydrodynamic coefficients (C.6b) for heave of a submerged cylinder ( $d/R = 1.25$ ) compared with first order theory results obtained by Ogilvie [26].



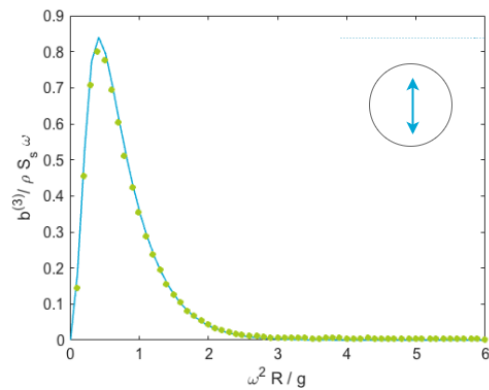
(a) Added mass of swaying cylinder.



(b) Added mass of heaving cylinder.



(c) Fluid damping of swaying cylinder.



(d) Fluid damping of heaving cylinder.

Figure C.7: Hydrodynamic coefficients of a submerged cylinder at  $d/R = 1.5$  compared with analytical values found by Liu et al. [46].

## C.5. Validation and verification

The results of the Frank Close Fit method are validated with experiments of Vugts [68]. These experimental values are shown in the Figures C.4 and C.5 and provide significant agreement with the numerical values of the FCFM. The differences between the fluid damping coefficients in the Frank Close Fit method and the experimental values are also visible in graphs made by Vugts [68].

The numerical model is partly based on the FORTRAN code ASAP [67], which is a program to predict the seakeeping behaviour of a catamaran. The code includes the Frank Close Fit method to calculate hydrodynamic coefficients for the cross-sections along the longitudinal axis of the catamaran [66]. For example Figure C.8 shows the same deviations between the results of ASAP and the experimental values (of Vugts) for a swaying cylinder. The ASAP program is also validated with the experiments of Vugts (as shown in Figure C.8 [66]) and shows the same deviation between the numerical code and the experiments as in Figure C.4.

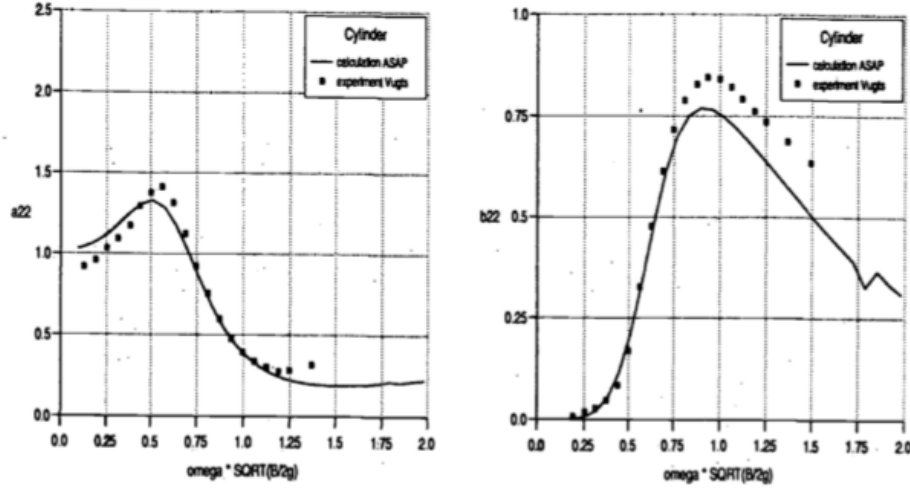


Figure C.8: ASAP Results and Vugts' experiments for Added Mass and Fluid Damping coefficient of swaying cylinder section [66].

In his report, Frank states that for very low and very large frequencies, the velocity potential differs somewhat from Equation C.19 [26]. In the low frequency range, the free-surface boundary condition should change into a wall equation. As a result of this altered boundary condition the Green's function ( $G_0$ ) is of the form [26]:

$$G_0(z, \zeta) = \frac{1}{2\pi} [\log(z - \zeta) + K_0 \log(z - \bar{\zeta})] \quad (C.33)$$

The attentive readers will note a change of sign between the two first parts of the Green's function in comparison with Equation C.16, where also the last two terms are left out. This is due to the fact that for very low frequencies (where  $\omega \rightarrow 0$ ) the free-surface boundary condition changed into a wall-condition. Since the velocity potential is found by integrating this Green's function multiplied with the source strength of the segment over the submerged contour, the factor  $K_0$  won't contribute to the velocity in some specific conditions:

- For submerged contours, the influence of the directional cosine  $n^{(m)}$  counterbalanced the addition of  $K_0$  since the contour is closed. Therefore the contribution of  $K_0$  vanishes [26].
- For even modes, the normal cosines of the left and right panels are related by  $n_{-i} = -n_i$ . This means that the contribution of  $K_0$  vanishes along the submerged contour, which also holds for roll-motions (which are not considered in this research project).

These two exceptions do not hold for a partly submerged cross-sections in heave-motions, where the terms [26]:

$$\int_{C_0} K_0 \cdot n^{(3)} \neq 0 \quad (C.34)$$

The value of constant  $K_0$  is undefined, but the value can be estimated by taking the limit of  $nu \rightarrow 0$  of Equation C.16.

For large frequencies, the free-surface changes into an 'impulsive' surface condition. In the Green's function (Equation C.16) the last two terms are replaced by a constant  $K_\infty$ , which is undefined. Since the Green's function for  $z \rightarrow \infty$  and therefore  $G_\infty \rightarrow 0$ , we can state that  $K_\infty = 0$  [26]. This problem for the large frequencies does not raise any problem for the FCFM as defined in this appendix. The change in velocity potential for the lower limit is not included in the numerical method yet. Probably the deviations at the boundaries of the frequency range, could probably be solved by adding this special conditions for the Green's functions in the specific region.

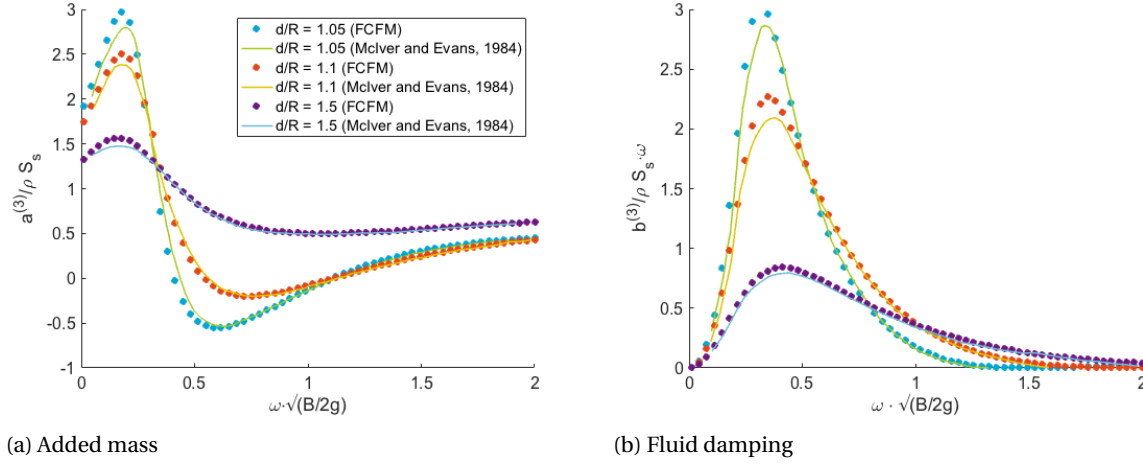


Figure C.9: Hydrodynamic added mass and fluid damping of a submerged circular cylinder at different submersion depths, where  $d$  is the submersion depth and  $R$  the tube's radius [49].

The numerical model of the Frank Close Fit method is verified for fully submerged cylinders for  $d/R \geq 1.25$ , as shown in Figure C.6. The values found by the Frank Close Fit Method (FCFM) are compared to the first order results of Ogilvie (as given by Frank) [26] for a cylinder submerged at  $1.25 \cdot R$ . For a cylinder that is submerged at  $d/R \geq 1.5$ , the values can be verified by the analytical calculation obtained by Liu et al. [46]. Results of this submerged cylinder are shown in Figure C.7. The analytical calculation of Liu et al. are based on the multipole expansion method as first introduced by Ursell [63]. Ursell's method provides a mathematical solution for oscillating cross-sections that can be mapped from a circle [43]. Ursell obtained solutions for cylinders oscillating in on the free surface [63] and for submerged cross sections [64]. The main reason to use the results of Liu [46] is that the analytical solution requires a lot of mathematics, which is not yet fully understood.

The results of  $d/R = 1.05$  show a negative added mass for a specific frequency range. This effect is also obtained in the past by McIver and Evans (1983) [49]. They claim that free-surface effects are causing a negative added mass. When ratio between the submersion depth and the cylinders radius is sufficiently small, a certain range of frequency shows this effect. The effects are also recognised in experiments carried out for squared and circular cross-sections. The cause of this effect should be found by energy equilibrium between kinetic and potential energy. For a deeply submerged cylinders, the effect of the potential energy is negligible and the added mass can be obtained as a mass of fluid that is accelerated by the motion of the body. For small depths of submergence, the mean potential energy can exceed the mean kinetic energy. As a result of this energy balance, a standing wave is formed above the cross-section [49].

## C.6. Conclusions

This Appendix discusses the Frank close-fit method which is a strong tool to calculate hydrodynamic coefficient. The added mass and fluid damping coefficient are defined by for a floating of fully submerged body. The bodies boundary is covered with panels of a constant source strength distribution. On this boundary, the strength of these sources is solved by the kinematic boundary condition. Finally the source strengths will be implemented in the velocity potential for each panel and the radiation pressure is found for every pressure.

Results are obtained for a floating cylinder and barges of different width/depth-ratios. The numerical results show a good resemblance with experimental values found by Vugts [69]. The fully submerged cylinders are verified with analytical values of Ogilvie [27] and Liu [46]. For both analytical sets of solutions, conformity is found with the numerical values. Overall, these results indicate that the numerical implementation of the Frank Close-Fit method corresponds to the linear potential solution of the radiation coefficients.

Implementation of the FCFM method into Matlab and tips to deal with mathematical challenges are attached in Appendix D.



# Description of FCF numerical model

This appendix is the description of the Matlab model to calculate the hydrodynamic coefficients  $a^{(m)}$  and  $b^{(m)}$ . These coefficients are derived with the Frank Close Fit (FCF) method as described in Appendix C. The order in this appendix differs from Appendix C, since the order is based on calculations in the Matlab model.

## D.1. Constants and geometrical characteristics

Two constants are used in the Matlab program:

- fluid density;  $\rho = 1025 \text{ kg/m}^3$
- gravitational acceleration;  $g = 9.81 \text{ m/s}^2$

Furthermore the geometry is described by several variables and parameters, this principal data is given for a cylinder and barge in Table D.1.

Dimension	Variable	Cylinder	Barge
(Bilge)radius	$R$	1 m	2.5 mm
Draft	$T$	1 m	1, 0.5 & 0.25 m
Width	$B$	2 m	2 m
Submersion depth	$d$	0 m	1 m
Cross-sectional area	$S_s$	$0.5 \cdot \pi \cdot R^2$	$\text{abs}(B \cdot T)$

Table D.1: Principal data of tested cylinder and barge

In the numerical model hydrodynamic coefficients are calculated in the frequency-domain. Since the frequency will be non-dimensionalised as mentioned in Section C.3, the frequency range will be defined by non-dimensional boundaries based on Vugts. Three parameters are important in this frequency range:

```
% Input parameters | Frequency
Nf = 40;           % [-] Number of frequencies
Nstart = 0.1;     % [-] Start point of non-dimensional frequency range
Nend = 2.0;       % [-] End point of non-dimensional frequency range
```

Furthermore, the submerged contour should be described as well. The number of panels on the submerged cross-section is given as 'NE', where the number of points  $NP = NE + 1$ . If the cross-section is symmetrical about the vertical axis, only the right part of the subsection has to be given as input. The left part of the contour is the image of the right part, where the variable 'IDSYM' is used to define whether the cross-section is symmetric. In Figure D.1 the values for IDSYM are shown with the input points to clarify the use of this variable. In the script the variables are defined as:

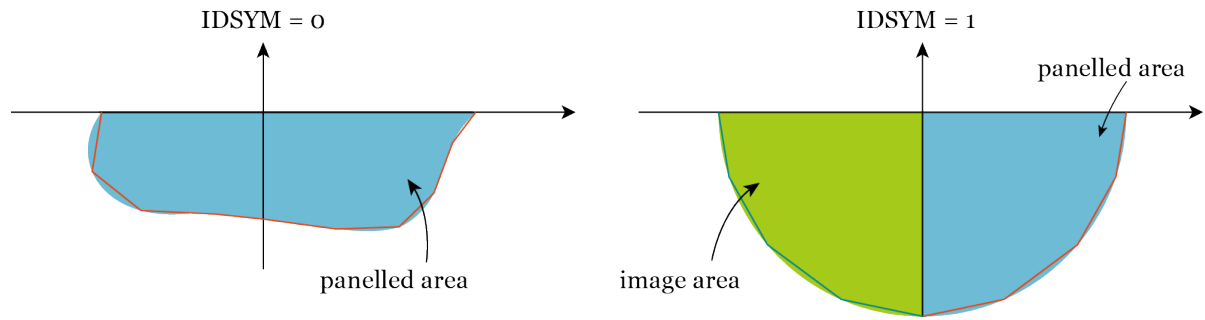


Figure D.1: Example of asymmetric and symmetrical bodies.

```
% Input parameters | Geometry
NE = 36;           % [-] Number of (initial) elements = 36
NP = NE+1;        % [-] Number of points (corners of elements)
IDSYM = 1;        % [-] IDSYM = 1 for symmetric body, IDSYM = 0 for asymmetric body
```

The last variable in this section is the amplitude of the forced oscillation. The amplitude should not influence the motion, as mentioned by Vugts [69]. The amplitude of the oscillation is given as:

```
% Input variables | Oscillatory motion
Am = 0.01;        % [m] Amplitude of oscillatory motion
```

## D.2. Mapping of geometry

The geometry is described by a number of points (NP) that define NE straight-line panels. This geometry description could be given by an input file, or could be defined by the script itself. For a floating cylinder the geometry description could be given for the 'asymmetrical' (IDSYM = 0) or a 'symmetrical' (IDSYM = 1) case.

```
if IDSYM == 0
    Ac = 0.5*pi*R^2;           % [m^2] cross-sectional area

    dtheta = pi/NE;           % [rad] Distribution parameter of panels
    theta = -pi:dtheta:0;     % [rad] Angular position of each point
    a = R*cos(theta);         % [m] x-coordinate of each point
    b = d+R*sin(theta);       % [m] y-coordinate of each point
    clear theta dtheta

    NE2 = NE;                 % [-] Number of elements to calculate
    NDEPTH = (NE/2) + 1;     % [-] Element with highest depth

elseif IDSYM == 1
    Ac = 0.5*pi*R^2;           % [m^2] cross-sectional area

    dtheta = 0.5*pi/NE;       % [rad] Distribution parameter of panels
    theta = -pi/2:dtheta:0;   % [rad] Angular position of each point
    a = R*cos(theta);         % [m] x-coordinate of each point
    b = d+R*sin(theta);       % [m] y-coordinate of each point
    clear theta dtheta

    % Define elements in the image plane (3rd quadrant)
    for i = 1:1:NP             % Extra parameter to define panels in 3rd quadrant
        ai(i) = a(i);
        bi(i) = b(i);
    end
    for i = 1:1:NP             % Change direction of panelling
        a(i) = -ai(NP+1-i);
        b(i) = bi(NP+1-i);
    end
    for i = NP+1:1:NP*2-1     % Translate panels into 4th quadrant
        a(i) = -a(2*NP-i);
    end
```

```

        b(i) = b(2*NP-i);
    end
    clear ai bi

    NDEPTH = NP;           % [-] Element with highest depth
    NP = 2*NP-1;          % [-] Number of total points
    NE = NP - 1;          % [-] Number of total elements
    NE2 = NE/2;           % [-] Number of elements to calculate
end

```

In the previous code, two remarks have to be made. Firstly, the panels on the image area are described (see previous code) and are used in the further calculations as input as well. Secondly, two new variables are introduced in this part of the code: NE2 and NDEPTH. NE2 is used to reduce calculation time, since the image elements are coupled to the initial elements as given in Table D.2. NDEPTH is referring to the point with the maximum depth.

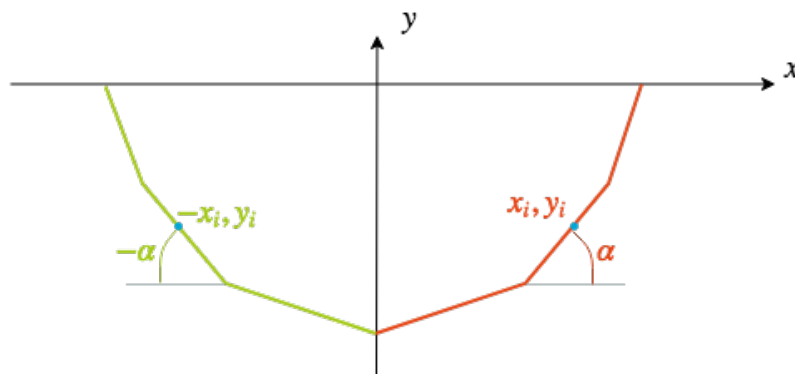


Figure D.2: Geometry characteristics for image segments.

The angle of each element with the horizontal, the midpoint coordinates  $x_i$  and  $y_i$  and the length of each segment are calculated according to the Equations C.9 until C.12 given in Appendix C.

This geometry description with the input variables of Table D.1 with  $IDSYM = 1$  results in a cross-section as shown in Figure D.3.

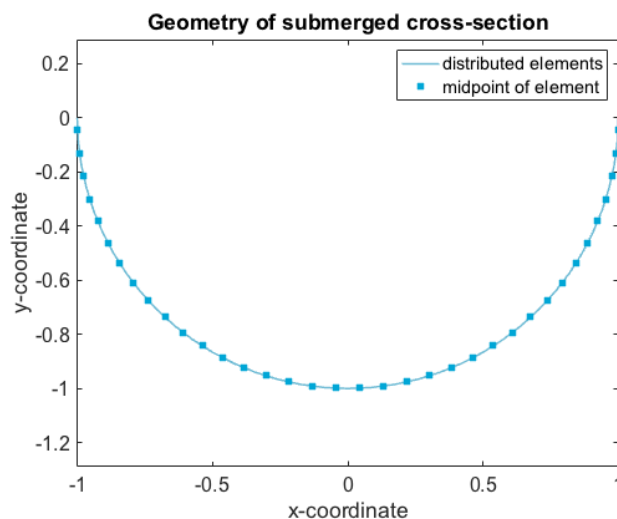


Figure D.3: Panels and their midpoints for a circular cylinder with  $NE = 18$ .

The final calculation is for the directional cosine, which is given in equation C.21 and is implemented in Matlab for the  $i$ th-panel:

```

% Calculate the directional cosines
DIRCOS(2,i) = sin(alpha(i)); % directional cosine for sway
DIRCOS(3,i) = -cos(alpha(i)); % directional cosine for heave

```

### D.3. Irregular frequencies

The resulting plots of Frank [26] and Van 't Veer [66] show some irregular frequencies. These irregular frequencies occur for surface piercing cross-sections, where the irregular frequency is the eigenfrequency of the interior wave problem. This interior wave problem is physically not interacting with the velocity potential of the fluid [74].

The values for irregular frequencies are known for rectangular cross-sections, but for any other arbitrary shape, the irregular frequencies have to be found by a set of equations where the irregular frequency is given by  $\omega_m$  [74]:

$$\omega_m = \{g \cdot k \cdot \coth(k \cdot h_e)\}^{1/2} \quad (D.1)$$

where

$$k = \frac{m \cdot \pi}{B_e}, \quad \text{for } m = 1, 2, \dots \quad (D.2)$$

The equivalent beam and draft are defined by:

$$B_e = (C_s)^{\alpha_e} \cdot B \quad \text{and} \quad h_e = \frac{S_s}{B_e} \quad (D.3)$$

where  $C_s = S_s/Bh$ ,  $S_s$  is the cross sectional area,  $B$  is the beam at the waterline and  $h$  is the draft at the midpoint of the beam. The value for  $\alpha_e$  is given by an empirical formula:  $\alpha_e = \{1 + \ln(m)\}/8$ . The value of  $m$  defines the  $m$ -th irregular frequency, where a value of 3 irregular frequencies is sufficient for a non-dimensional frequency range between 0.1 and 2.0.

In Matlab these equations are implemented in a function `irregular(Ac,W,T,m)`:

```

function [OMEGAM] = irregular(Ac,W,T,m)
% irregular: Summary of this function goes here
% Calculation method presented by X-J. WU in CADMO 86
% "A two-dimensional Source-Dipole Method for Seakeeping
% Analysis of Ships and Offshore Structures"

g = 9.81;

% Start execution
for i = 1:1:m
% Calculate the empirical correction coefficient, alpha
ALPHA = 0.125*(1 + log(i));

% Calculate the equivalent Beam (BEQUIV) and Draft (HEQUIV)
% using the cross sectional area CS
CS = Ac / (W*abs(T));
BEQUIV = W * (CS)^ALPHA;
HEQUIV = Ac / BEQUIV;

% Calculate the wave number with the equivalent Beam value
KEQUIV = i * pi / BEQUIV;

% Calculate the M-the irregular frequency
OMEGAM(i) = sqrt(g * KEQUIV * cosh(KEQUIV * HEQUIV) / sinh(KEQUIV * HEQUIV));
OMEGAM(i) = sqrt((g*i*pi()/W) * cosh(i*pi()*abs(T)/W) / sinh(i*pi()*abs(T)/W));
end

clear ALPHA CS BEQUIV HEQUIV
end

```

## D.4. Non-frequency parts of influence and potential coefficients

The equations for the kinematic boundary condition and the velocity potential have both a part that is independent of the frequency and a part that is depending on the frequency.

In the Matlab function `DEPTHS (NE, NE2, x, y, a, b, alpha)` the frequency-independent components of the kinematic boundary condition and the velocity potential are calculated.

In this function, the components of both equation are calculated parallel to eachother. The script is constructed according to the following guidelines:

1. Start loop over index  $i$ , from 1 up to NE2.
2. Set initial index  $j$ ;  $j = 1$
3. Calculate complex variables for lower limit;  $z_i - c_j$  and  $z_i - \bar{c}_j$ .
4. Calculate logarithmic functions for lower limits.
5. Start loop over index  $j$ , from 2 up to NE.
6. Calculate complex variables for upper limit;  $z_i - c_{j+1}$  and  $z_i - \bar{c}_{j+1}$ .
7. Calculate logarithmic functions for upper limits.
8. Calculate (global) equation components.
9. Update lower limits with upper limits.
10. Go to the next  $j$ .
11. Go to the next  $i$ .

According to the guidelines the components of CB (kinematic boundary condition) and CU (velocity potential) are calculated. These components and their definition of Appendix C and in Matlab, are given in Table D.2 for CB and in Table D.3 for CU.

Matlab name	Formulation (From equation C.23)	Definition Matlab model
CBM1J	$z_i - c_j = (x_i - a_j) + i \cdot (y_i - b_j)$	<code>CBM1J = complex(x(i)-a(j), y(i)-b(j))</code>
CBM1J1	$z_i - c_{j+1} = (x_i - a_{j+1}) + i \cdot (y_i - b_{j+1})$	<code>CBM1J1 = complex(x(i)-a(j+1), y(i)-b(j+1));</code>
CBM2J	$z_i - \bar{c}_j = (x_i - a_j) + i \cdot (y_i + b_j)$	<code>CBM2J = complex(x(i)-a(j), y(i)+b(j))</code>
CBM2J1	$z_i - \bar{c}_{j+1} = (x_i - a_{j+1}) + i \cdot (y_i + b_{j+1})$	<code>CBM2J1 = complex(x(i)-a(j+1), y(i)+b(j+1));</code>
CB1(i, j)	$i e^{i(\alpha_i - \alpha_j)} = -\sin(\alpha_i - \alpha_j) + i \cdot \cos(\alpha_i - \alpha_j)$	<code>SINIMJ = sin(alpha(i)-alpha(j));</code> <code>COSIMJ = cos(alpha(i)-alpha(j));</code> <code>CB1(i, j) = complex(-SINIMJ, COSIMJ);</code>
CB2(i, j)	$i e^{i(\alpha_i - \alpha_j)} \cdot (\log(z_i - c_{j+1}) - \log(z_i - c_j))$	<code>CB2U = log(CBM1J1);</code> <code>CB2L = log(CBM1J);</code> <code>CB2(i, j) = CB1(i, j) * (CB2U - CB2L);</code>
CB3(i, j)	$i e^{i(\alpha_i + \alpha_j)} = -\sin(\alpha_i + \alpha_j) + i \cdot \cos(\alpha_i + \alpha_j)$	<code>CB3(i, j) = complex(-sin(alpha(i)+alpha(j)), ...</code> <code>cos(alpha(i)+alpha(j)));</code>
CB4(i, j)	$\log(z_i - \bar{c}_{j+1}) - \log(z_i - \bar{c}_j)$	<code>CB4U = log(CBM2J1);</code> <code>CB4L = log(CBM2J);</code> <code>CB4(i, j) = CB4U - CB4L;</code>

Table D.2: Non-frequency components of kinematic boundary condition (CB) in numerical model.

An important remark has to be made about the components  $CB2(i, j)$  and  $CU2(i, j)$ , where the principal branch could results in invalid results. For the first term in the kinematic boundary condition, the principal branch is avoided by the following code:

```

if i == j
    CB2(i,j) = pi();
elseif ((sin(alpha(i)) <= 0) & ...
        (sin(alpha(j)) > 0) & ...
        (abs(b(j)) > abs(y(i))) & ...
        (abs(y(i)) >= abs(b(j+1))) & ...
        (i ≠ j))
    CB2(i,j) = CB2(i,j) - 2*pi()*imag(CB1(i,j)); % avoid branch point
end

```

For the influence of the corner points on the element itself, the following integral is solved, since  $ie^{i(\alpha_j - \alpha_j)} = i \cdot 1$  [26, 66]:

$$\begin{aligned}
 \text{CB1} &\stackrel{i=j}{=} \operatorname{Re}_I \{-i \cdot (\log(z_j - c_j) - \log(z_j - c_{j+1}))\} \\
 &\stackrel{i=j}{=} \arg(z_j - c_j) - \arg(z_j - c_{j+1}) \\
 &\stackrel{i=j}{=} (\pi + \alpha_j) - \alpha_j = \pi
 \end{aligned} \tag{D.4}$$

This relation should be checked, since the definition of an argument of a complex argument is:  $\arg(z) = \operatorname{Arg}(z) + 2n\pi$ , where  $n$  is any integer and  $-\pi < \operatorname{Arg}(z) \leq \pi$ . The first condition deals with the boundaries of  $\operatorname{Arg}(z)$ , where the result is forced to be  $\pi$ .

In equation D.4 this definition of the argument is important in the imaginary part of the logarithm. When a logarithm of a complex number should be calculated, the logarithm could be separated into a real and an imaginary part [59]:

$$\log(z) = \log|z| + i \cdot \arg(z) = \log|z| + i \cdot (\operatorname{Arg}(z) + 2n\pi) \quad \text{where } n = \pm 1, \pm 2, \dots \tag{D.5}$$

This equation shows that the complex logarithmic function is a multi-valued function. This means that the same input could give different results, which are called a different 'branch' of the same function [32]. To avoid these branches, an artificial barrier is introduced that cannot be crossed. This barrier is called a 'branch cut', which is placed along the negative y-axis in this case [59]. A branch cut results in a jump in the results over this artificial barrier. The conversion of a multi-valued (natural) logarithm into a single-valued logarithm is showed in figure D.4.

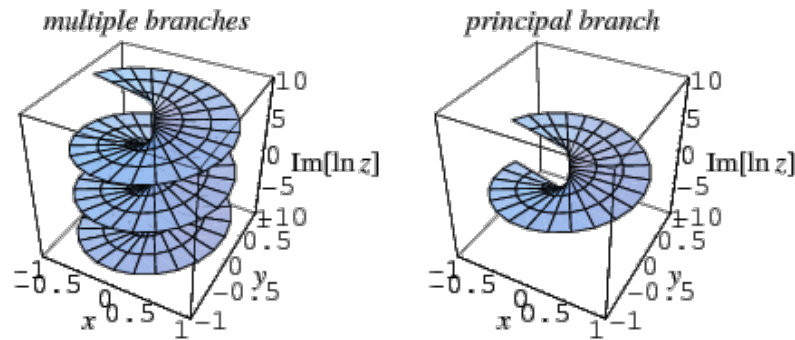


Figure D.4: Example of a multi-valued logarithm with multiple branches and a single-valued logarithm with a principal branch along the negative x-axis [71].

The first condition is added to the script to avoid the branch cut along the negative y-axis. Since the branch-cut only influences the imaginary part of the complex logarithmic function, the correction of  $i2\pi$  is multiplied with the imaginary part of CB1.

The second component of the potential function has to deal with the same issues. In this case the branch cut is avoided by the same condition, but a variable `HELP` is introduced to correct the value of `CU2(i, j)`.

```

if ((sin(alpha(i)) <= 0) & ...
    (sin(alpha(j)) > 0) & ...
    (abs(b(j)) > abs(y(i))) & ...
    (abs(y(i)) >= abs(b(j+1)))) & ...
    (i ≠ j))
    CHELP = real(pi()*complex(sin(alpha(j)),cos(alpha(j)))*(CBM1J + CBM1J1));
    CU2(i,j) = CU2(i,j) - CHELP;
end

```

Matlab name	Formulation (From equation C.19)	Definition Matlab model
CU1	$e^{-i\alpha_j} = \cos(\alpha_j) - i \cdot \sin(\alpha_j)$	CU1 = complex(cos(alpha(j)), -sin(alpha(j)));
CU2(i, j)	$e^{-i\alpha_j} \cdot ((z_i - c_{j+1}) - (z_i - c_{j+1}) \cdot \log(z_i - c_{j+1}) - (z_i - c_j) + (z_i - c_j) \cdot \log(z_i - c_j))$	CU2U = CBM1J1*CB2U - CBM1J1; CU2L = CU2L = CBM1J*CB2L - CBM1J; CU2(i, j) = CU1 * (CU2L - CU2U);
CU4(i, j)	$e^{i\alpha_j} \cdot ((z_i - \bar{c}_{j+1}) - (z_i - \bar{c}_{j+1}) \cdot \log(z_i - \bar{c}_{j+1}) - (z_i - \bar{c}_j) + (z_i - \bar{c}_j) \cdot \log(z_i - \bar{c}_j))$	CU4U = CBM2J1*CB4U - CBM2J1; CU4L = CBM2J*CB4L - CBM2J; CU4(i, j) = conj(CU1) * (CU4L - CU4U);

Table D.3: Non-frequency components of velocity potential (CU) in numerical model.

## D.5. Frequency parts of influence and potential coefficients

The frequency-dependent parts are calculated inside a loop over the frequency range, as defined in Section D.1. For every frequency the frequency-dependent components of the kinematic boundary condition and velocity potential of Equation C.23 and C.19 are calculated. These components are given for CB (kinematic boundary condition) in Table D.4 and for CU (velocity potential) in Table D.5. These components are calculated in a Matlab function called FREQUENCY1 (NE, NE2, x, y, a, b, alpha, v, CB2, CB3, CB4, CU2, CU4). Some of the frequency-independent components of CB and CU (of Tables D.2 and D.3) are used in the calculations.

Matlab name	Formulation (From equation C.23)	Definition Matlab model
Z	$Z_j = -iv \cdot (z_i - c_j)$	Z = complex(v*imag(CBM2J), -v*real(CBM2J));
[CB6L, CB7L]	<i>Function to calculate principal value integral</i>	[CB6L, CB7L] = PVint(Z);
Z	$Z_{j+1} = -iv \cdot (z_i - c_{j+1})$	Z = complex(v*imag(CBM2J1), -v*real(CBM2J1));
[CB6U, CB7U]	<i>Function to calculate principal value integral</i>	[CB6U, CB7U] = PVint(Z);
CB6(i, j)	$PV \int_0^\infty \frac{e^{-ik(z_i - \bar{c}_{j+1})}}{v - k} dk - PV \int_0^\infty \frac{e^{-ik(z_i - \bar{c}_j)}}{v - k} dk$	CB6(i, j) = CB6U - CB6L;
CB7(i, j)	$ie^{i(\alpha_i + \alpha_j)} \cdot (e^{-iv(z_i - c_{j+1})} - e^{-iv(z_i - c_j)})$	CB7(i, j) = CB3(i, j) * (CB7U - CB7L);

Table D.4: Frequency-depending components of kinematic boundary condition (CB) in numerical model.

The calculation of the Principal Value integral and the fourth terms of Equation C.19 and C.23 are executed by the function `PVint(Z)`. This function calculates the Principal Value integral and the exponent of the complex function  $-iv(z-\bar{c})=Z$ . The script of function `PVint(Z)` is given:

```
function [COF6,COF7] = PVint(Z)
%PVint Summary of this function goes here
% the PVint returns the principal value integral as defined by Abramowitz
% and Stegun and uses the matlab function expint()

% Detailed explanation goes here

% Constants
gamma = 0.5772156649;

% Calculate exponent 7
COF7 = exp(Z);

% Calculate the Exponential Integral (with epsilon .lt. 0.5d-6)
% Used in ASAP (and in table 5.6 Abramowitz & Stegun)
if (abs(real(Z)) >= 10) | (abs(imag(Z)) >= 10)
    PVZ = (0.711093/(Z+0.415775))+(0.278518/(Z+2.29428))+(0.010389/(Z+6.2900));
    E1Z = PVZ/exp(Z);

    % Calculate coefficient 6
    if imag(Z) < 0
        COF6 = COF7*(complex(0,-pi)-E1Z);
    else
        COF6 = COF7*(complex(0,+pi)-E1Z);
    end
else
    % Calculate the Exponential Integral (Matlab function)
    E1Z = expint(Z);

end

% Calculate coefficient 6
if imag(Z) < 0
%
    COF6 = COF7*(complex(gamma,+pi)+log(Z) - E1Z);
    COF6 = COF7*(complex(0,+pi) - E1Z);
else
%
    COF6 = COF7*(complex(gamma,-pi)+log(Z) - E1Z);
    COF6 = COF7*(complex(0,-pi) - E1Z);
end
end
```

Where the 'if-statement' gives an exception to the given solution of the Principal Value integral of Equation C.17. This numerical method is an approximation for the function  $e^z E_1(z)$  for large arguments of  $z$  and is given in the tables of Abramowitz and Stegun [28, 67]. The calculation of coefficient 6 includes the value of  $\delta$ , which is defined in the Equations C.17 and C.18.

Matlab name	Formulation (From equation C.19)	Definition Matlab model
CHELP	$\frac{-ie^{i\alpha_j}}{\nu}$	CHELP = complex(sin(alpha(j)), ... -cos(alpha(j)))/v;
CU5(i, j)	$\frac{-ie^{i\alpha_j}}{\nu} \cdot (\log(z_i - \bar{c}_j) - \log(z_i - \bar{c}_{j+1}))$ $+ PV \int_0^\infty \frac{e^{-ik(z_i - \bar{c}_{j+1})}}{\nu - k} dk$ $- PV \int_0^\infty \frac{e^{-ik(z_i - \bar{c}_j)}}{\nu - k} dk$	CU5(i, j) = CHELP * (CB6(i, j) - CB4(i, j));
CU6(i, j)	$\frac{-ie^{-i\alpha_j}}{\nu} \cdot (e^{-iv(z_i - c_{j+1})} - e^{-iv(z_i - c_j)})$	CU6(i, j) = CHELP * (CB7U - CB7L);

Table D.5: Frequency-dependent components of velocity potential (CU) in numerical model.

## D.6. Assembling influence and potential matrices

Due to symmetry, only one half of the submerged body is calculated for the non-frequency and frequency dependency components. For an asymmetric body, the total matrix will be calculated. To complete the matrix components of CB and CU for symmetric bodies, the image components are calculated in the reverse direction:

### Non-frequency dependent components

```

if NE ≠ NE2
  for i = NE:-1:(NE2+1)
    for j = NE:-1:1
      CB1(i, j) = ...
        -conj(CB1(NE-i+1, NE-j+1));
      CB2(i, j) = ...
        conj(CB2(NE-i+1, NE-j+1));
      CB3(i, j) = ...
        -conj(CB3(NE-i+1, NE-j+1));
      CB4(i, j) = ...
        -conj(CB4(NE-i+1, NE-j+1));
      CU2(i, j) = ...
        conj(CU2(NE-i+1, NE-j+1));
      CU4(i, j) = ...
        conj(CU4(NE-i+1, NE-j+1));
    end
  end
end

```

### Frequency dependent components

```

if NE ≠ NE2
  for i = 1:1:NE2
    for j = 1:1:NE
      CB6(NE-i+1, NE-j+1) = CB6(i, j);
      CB7(NE-i+1, NE-j+1) = CB7(i, j);
      CU5(NE-i+1, NE-j+1) = CU5(i, j);
      CU6(NE-i+1, NE-j+1) = CU6(i, j);
    end
  end
end

```

Now all the components of CB and CU are calculated and their matrices are completed with the image segments, the total matrices will be composed. In the composition of the matrices CB and CU, still the upper part of the matrix<sup>1</sup> is calculated (for symmetric bodies) to make sure that the matrix is symmetric.

```

for i = 1:1:NE2
    for j = 1:1:NE
        % Build global coefficient
        CB(i,j) = complex(real(CB2(i,j) - CB3(i,j)*CB4(i,j) + 2*CB3(i,j)*CB6(i,j))/ ...
            (2*pi), -real(CB7(i,j)));

        % Build global coefficient
        CU(i,j) = complex(real(CU2(i,j) - CU4(i,j) + 2*CU5(i,j))/(2*pi), -real(CU6(i,j)));
    end
end
end

```

To compose the matrix A of Equation C.24, a new matrix is introduced to combine matrices based on the mode of oscillation. In this case the even modes are sway ( $m = 2$ ) and roll ( $m = 4$ ), and the odd mode is heave (with  $m = 3$ ). For a symmetric submerged body, these matrices of the kinematic boundary condition and velocity potential for both even and odd modes are defined as:

```

for i = 1:1:NE2
    for j = 1:1:NE
        INFBO(i,j) = CB(i,j);
        INFUO(i,j) = CU(i,j);
        INFBE(i,j) = CB(i,j);
        INFUE(i,j) = CU(i,j);
        INFBO(NE-i+1,NE-j+1) = CB(i,j);
        INFUO(NE-i+1,NE-j+1) = CU(i,j);
        INFBE(NE-i+1,NE-j+1) = CB(i,j);
        INFUE(NE-i+1,NE-j+1) = CU(i,j);
    end
end
end

```

## D.7. Calculate source strengths

Now the matrices for each mode for the kinematic boundary condition are defined, the source strength will be solved by the matrix multiplication of Equation C.24. The code is written separately for the modes sway and heave, where matrix A is built and array B is composed as described in Equation C.25:

```

% Build A matrix
for m = 2:1:3
    if m == 2 % for sway
        for i = 1:1:NE
            for j = 1:1:NE
                A(i,j) = INFBE(i,j);
            end
            % Build b vector (radiation problem) and solve the problem
            B(i) = complex(0, -Am*DIRCOS(2,i)*om); % - in time-convention of Frank
        end
        [SNGULR,CV,DET,A] = decomp(NE,A,EPS);
        SOURCE(m,:) = mldivide(A,B');
    end
end

```

<sup>1</sup>The code for the image segments is still included in the code, to make sure that other calculations are able to be calculated as well. But for the composition of the matrices CB and CU it was not necessary to include these components for the image part of the submerged body.

```

else % for heave
    for i = 1:1:NE
        for j = 1:1:NE
            A(i,j) = INFBO(i,j);
        end
        % Build b vector (radiation problem) and solve the problem
        B(i) = complex(0,-Am*DIRCOS(3,i)*om); % - in time-convention of Frank
    end
% [SNGULR,CV,DET,A] = decomp(NE,A,EPS);
SOURCE(m,:) = mldivide(A,B'); % was - (zelf toegevoegd)
end
end
end

```

where  $SOURCE(m, :) = mldivide(A, B')$ ; performs the matrix division in both modes of oscillation and gives the source strengths  $Q_j$  of the equations in Appendix C.

## D.8. Calculate pressure distribution

The source strengths  $Q_j$  are directly implemented in the pressure-calculation, which is given in Equation C.26. For the pressure calculation a division is made in mode of oscillation, as mentioned in Section D.6. The pressure is calculated in this part of the script:

```

% Calculate the complex pressure distribution for the radiation problem (PRSS)
% First, calculate the velocity potential
for m = 2:1:3
    for i = 1:1:NE2
        PRSS(m,i) = complex(0,0);
        for j = 1:1:NE
            if m == 3
                PRSS(m,i) = PRSS(m,i) + SOURCE(m,j)*INFUO(i,j);
            else
                PRSS(m,i) = PRSS(m,i) + SOURCE(m,j)*INFUE(i,j);
            end
        end
    end

    % Calculate the pressure
    PRESS(m,i) = complex(rho*om*imag(PRSS(m,i)), rho*om*real(PRSS(m,i)));
end
end
end

```

## D.9. Determine hydrodynamic coefficients

The pressure-distribution over the panels of the submerged body is the starting point of the hydrodynamic coefficient calculation. In Appendix C these calculations are explained by the force, but this step is skipped in the numerical model. As an addition to the theory, the cross-terms between different modes are introduced. Since the model is only validated for sway ( $m = 2$ ) and heave ( $m = 3$ ), the applied oscillations are only in these directions. The directions of the applied oscillations are denoted by index  $fm$ , where the index  $m$  denotes the resulting mode of the body. In the Matlab model, the calculation of the hydrodynamic coefficients is therefore given as:

```

% Calculate the Added Mass and Damping for heave
% Initialise Added Mass and Damping
for fm = 2:1:3
    for m = 2:1:3
        ADDM(fm,m) = 0;
        DAMP(fm,m) = 0;
        ADDMCOF(fm,m) = 0;
        DAMPCOF(fm,m) = 0;

        if (fm == 2 & m == 3)
            ADDM(fm,m) = 0;
            DAMP(fm,m) = 0;
            ADDMCOF(fm,m) = 0;
            DAMPCOF(fm,m) = 0;
        elseif (fm == 3 & m == 3)
            ADDM(fm,m) = 0;
            DAMP(fm,m) = 0;
            ADDMCOF(fm,m) = 0;
            DAMPCOF(fm,m) = 0;
        else
            ADDM(fm,m) = 0;
            DAMP(fm,m) = 0;
            ADDMCOF(fm,m) = 0;
            DAMPCOF(fm,m) = 0;
            for i = 1:1:NE2
                ADDM(fm,m) = ADDM(fm,m) - real(PRESS(m,i))*s(i)*DIRCOS(m,i);
                DAMP(fm,m) = DAMP(fm,m) + imag(PRESS(m,i))*s(i)*DIRCOS(m,i);
            end

            if IDSYM == 1
                ADDM(fm,m) = 2*ADDM(fm,m) / (Am*om*om);
                DAMP(fm,m) = 2*DAMP(fm,m) / (Am*om);
            else
                ADDM(fm,m) = ADDM(fm,m) / (Am*om*om);
                DAMP(fm,m) = DAMP(fm,m) / (Am*om);
            end

            SCALEA = rho*Ac; % scale for added mass (according to Vugts)
            SCALEB = SCALEA*sqrt((2*g)/W); % scale for fluid damping (according to Vugts)

            M(fm,m,o) = ADDM(fm,m); % [kg] Added mass
            N(fm,m,o) = DAMP(fm,m); % [kg/s] Fluid damping

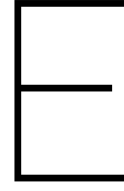
            ADDMCOF(fm,m,o) = ADDM(fm,m)/SCALEA; % scaling of added mass coefficient
            DAMPCOF(fm,m,o) = DAMP(fm,m)/SCALEB; % scaling of fluid damping coefficient
        end
    end
end

```

where the  $ADDMCOF(fm, m, o)$  is the added mass coefficient for mode  $m$  resulting from forced oscillation in direction  $fm$  at a particular frequency denoted by index  $o$ . The same holds for the fluid damping coefficient, denoted by  $DAMPCOF(fm, m, o)$ .

Since the motions heave and sway are not coupled by symmetry, the values of  $a_{23} = a_{32} = 0$  and  $b_{23} = b_{32} = 0$  [37].

Finally, the added mass and fluid damping coefficients will be non-dimensionalised by either Vugts, Frank or Van 't Veer. The results of this model are the non-dimensional results according to Vugts, which are given in Table C.2.



# Bulging cylinder

This Appendix starts with the implementation of phase 1 (as defined in Appendix B. In Subsection E.2.1 previous research involving bulge WEC's is compared, which will be concluded in Subsection E.2.2. In Subsection E.2.3 the assumptions and boundary conditions of an advanced bulging WEC are constituted.

## E.1. Simple distensible cylinder

The bulging cylinder in the most simple way is a pulsating cylinder with a prescribed bulging frequency  $\omega_b$ . The cylinder is expanding and contracting over one period. This results in a time-dependent radius<sup>1</sup>:

$$\begin{aligned}
 R(t) &= R_s (1 + \varepsilon_0 \cdot \cos(\omega_b t)) \\
 &= R_s + R_s \cdot \varepsilon_0 \cdot \cos(\omega_b t) \\
 &= \text{Re}_j \left\{ R_s + R_s \cdot \varepsilon_0 \cdot e^{-j\omega_b t} \right\}
 \end{aligned}
 \tag{E.1}$$

where  $\varepsilon_0$  is the maximum strain of the pulsating cylinder, which is expanding and contracting with frequency  $\omega_b$ .  $R_s$  is the undeformed radius of the cylinder. To define the deformations of the tube in an earth-fixed coordinate system, the coordinates of the FCFM are transformed according to Figure E.1.

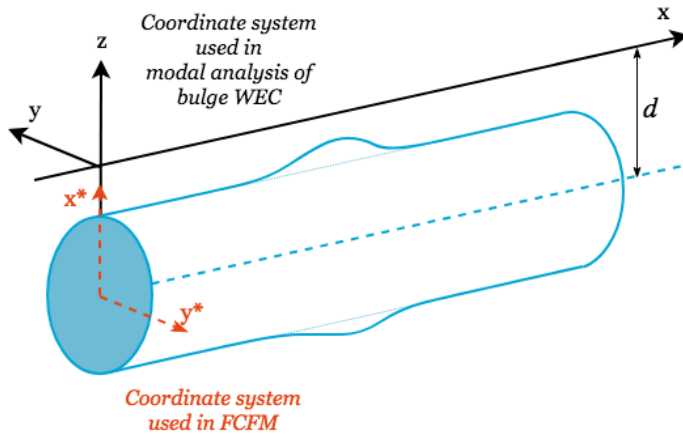


Figure E.1: Coordinate transformation between FCFM (of Appendix C and D) and bulging motion in 3D (for Appendix E and F)

To satisfy physics of the bulging cylinder, the kinematic boundary condition should be adapted for the simple distensible cylinder. The kinematic boundary condition of Equation C.20 will be transformed (from Equation

<sup>1</sup>In Appendix B the time-dependent radius and strain are given by a sin-function. Due to the methodology of Frank [26], the bulging oscillation is transformed into a cos-function. Since the bulging oscillation is an assumption to model a bulge wave energy converter, the phase-difference of 90 degrees is not that important.

B.5) into [60]:

$$\begin{aligned}
 \vec{n} \cdot \nabla \Phi &= \operatorname{Re}_I \left\{ \sum_{j=1}^N Q_j (\vec{n} \cdot \nabla) \int_{C_j} G(z, c) ds \cdot e^{-j\omega t} \right\} = \frac{\partial R}{\partial t} \\
 &= \operatorname{Re}_j \left\{ \frac{\partial}{\partial t} \left( R_s + R_s \cdot \varepsilon_0 \cdot e^{-j\omega_b t} \right) \right\} \\
 &= \operatorname{Re}_j \left\{ -j \cdot \omega_b \cdot R_s \cdot \varepsilon_0 \cdot e^{-j\omega_b t} \right\}
 \end{aligned} \tag{E.2}$$

which is adapted in the kinematic boundary condition, to find the source strengths. Since the bulging distensible cylinder is not moving in either the sway or heave direction, but in the normal direction of each panel, the value of  $n_i^{(B)} = 1$ . The observed motion is the bulging motion, which result in the following adaptations to the Matlab model:

- A bulge wave energy converter is operating beneath the free surface, where the heave and sway motion are verified from a depth of  $d/R = 1.25$  and lower and therefore a depth of  $d/R_s = 1.25$  is chosen. This results in a different geometry and therefore some adaptations in the geometry characteristics, like the submerged area ( $S_s = \pi \cdot R_s^2$ ) and the submersion depth ( $d = -1.25R$ ).
- The radiation pressure is defined in a principal direction, so in x- or y-direction. In sway the pressure in x-direction is multiplied by the directional cosines in x-directions and for heave the pressure and directional cosines in the y-directions are multiplied. For both motions, the radiation pressure has over one half of the contour a negative contribution. The vector combination of the surge- and heave motion results in the normal vector to each single element along the contour. This is shown Figure E.2. Since the directional cosines are the length of the normals for bulging, the pressures over all elements of the contour contribute with the same sign. In reality, some panels counteract with each other and some pressure contribution will vanish due to this special symmetry within the bulging motion. The pressure contributions are therefore calculated for the heave ( $m = 3$ , in z-direction) and sway motion ( $m = 2$ , in y-direction), where these two motions are combined in the same way as the directional cosines are combined by vector analysis.

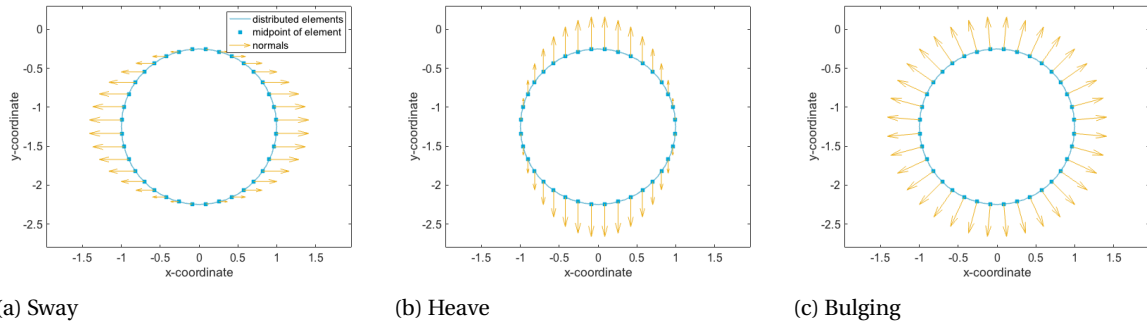
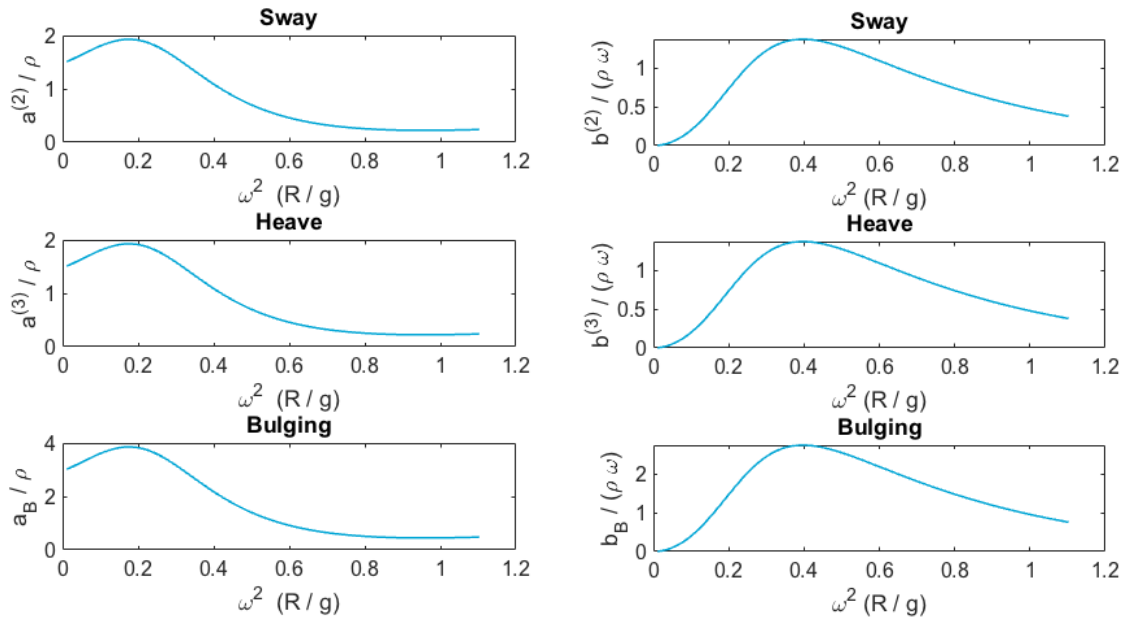


Figure E.2: Directional cosines for E.2a sway, E.2b heave and E.2c bulging.

The results of a simple distensible cylinder submerged at  $d/R = 1.25$  are shown in Figure E.3. The lowest graphs in this figure are representing the bulging modes, which are a combination of the sway and heave motions.

The results of Figure E.3a and E.3b could not be validated or verified directly. The only way to check the results is based on a graph given by Fathi, Lee and Newman [24]. This graph (see Figure E.4a) is based on a mode shape of a 'surge-pressure' mode, which can be interpreted as a bulging mode. Since this figure represents two different modes, the values are related to the modal analysis (which will be described in Appendix F), but the shape of the hydrodynamic coefficients shows analogy of with the results of the bulging motion. The bulging motion as calculated by the adapted FCFM is plotted against the period of oscillation in Figure E.4b. Since the geometry characteristics of the cylinder are not known as used by Fathi et al. [24], the magnitudes of the motions are not directly comparable. The magnitudes of the dotted lines in Figure E.4b, which represent the second bending mode coefficients, are a lot smaller than the magnitude of the first bulging mode (denoted by a solid line). On the other hand, the ratio between the peak values of added mass and damping for the

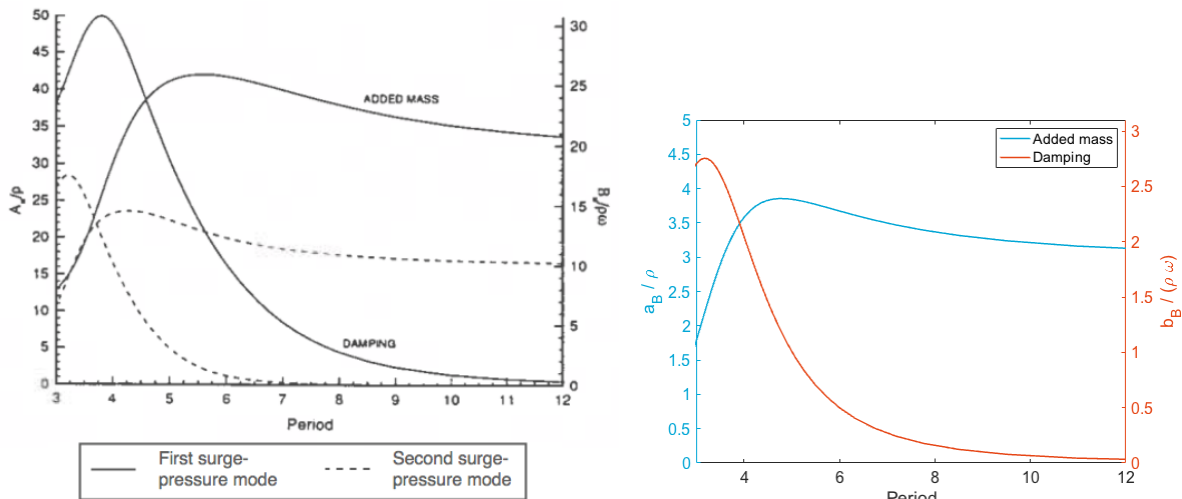


(a) Added mass coefficient

(b) Fluid damping coefficient

Figure E.3: Hydrodynamic coefficients of a cylinder submerged at  $d/R = 1.25$  for heave, sway and bulge.

individual mode shapes corresponds between both figures. Conclusions about the validity of the FCFM for bulging in a modal analysis will be drawn in Appendix F, but the first comparison looks promising.



(a) Results Fathi et. al [24]

(b) Results FCFM at  $d/R = 1.25$ .

Figure E.4: Hydrodynamic coefficients of a cylinder submerged at  $d/R = 1.25$  for heave, sway and bulge.

A more direct verification method can be found in the work of Ursell and Dean [64]. In Ursells paper, Dean states that a submerged cylinder that gives pulsations is one of the applications of the theory that Ursell initiated. Short notes are given as an application of the analytical tool to calculate surface waves [64]. This method is not easy to implement at the moment, so further investigation into this work is recommended to verify the results of bulging cylinder in a more direct way.

## E.2. Fluid-filled bulging cylinder operating under waves

Due to the pressure differences resulting from incoming waves, the distensible material deforms locally. These local deformations cause a bulge wave, driven by the pressure difference over the tube wall. The travelling bulge is the driving source of energy, where the elastic energy in the wall will be converted into power by either a Power Take-off (PTO) at the tube's stern or by Electro Active Polymers (EAP) that are generating power by the material itself [8, 15].

### E.2.1. Literature review

This section is organised in the following way. Both types of bulge wave energy converters are described, including the main advantages and drawbacks of the systems and the theory developed for its applications. As small note will be made on the experimental tests of Gerrard and the applicability of his work as a validation method as mentioned in Appendix B. The comparison of literature is concluded in a methodology description (in Subsection E.2.2 for the phase 2 and 3 of Appendix B. The choices and assumptions corresponding to this methodology that will be presented in Subsection E.2.3.

#### Anaconda WEC

In 2006 Farley and Rainey published their first notes about a 'bulge-wave' device for wave energy conversion. They referred to the Lancaster flexible bag device to be a precursor of their wave energy converter and to the dragone as a system with common features [14, 21]. In the case of a wave energy device, the distensible rubber tube will be filled with fluid and is oriented in head waves. A regular incident wave of amplitude  $\zeta_I$  is used as input, where the incident wave is described with wavenumber  $\nu$  and velocity  $c$ :

$$\zeta = \zeta_I \cdot \sin(\nu(x - c \cdot t)) \quad (\text{E.3})$$

Some assumptions are made to simplify the system. The device is assumed to be infinitely long and the bulge wave equilibrium is considered as a problem in steady flow. The fluid velocity inside the tube is described by the axial velocity, since the other velocity components are negligible small. The cross-sectional area is therefore compressing and extracting by the internal velocity. The Bernoulli equation for a steady flow in combination with Lighthills' definition of the distensibility of the cross section [44], gives a simple result for the pressure inside the tube. The incident and bulge wave are assumed to have no phasedifference and the cross section is expected to be transformed into an ellipse with the long axis pointed upwards in a wave crest. Following the wave, the cross-section will be transformed into an ellipse with long axis oriented horizontally in a wave trough. The power transferred by this initial design is expected to be a multiplication of the volume flow rate and the pressure. This first simple formulations are checked by assuming simple material characteristics, where some effects are neglected. The material is chosen to prevent the influence of hysteresis losses in the material. In this feasibility study some mathematical and physical topics are furthermore addressed to be important in future research on a bulge wave device [21].

A more investigated design of a distensible tube with internal tube waves, is described in a 2011 patent. The invention assigned to this application is principally the distensibility of the elastic tube as a device to extract wave energy. The bulge wave speed in the tube with elastic walls matches the velocity of the ocean waves [22].

Chaplin et al. shared their promising ideas in 2012 about the Anaconda in two papers describing both the WEC theory and the experiments. In these papers the resonance between the water wave and the bulge wave speeds is described. When both velocities are close to each other, a small excitation of the incoming wave can produce a large bulging wave. The hysteresis losses are still unknown, so these losses are implemented as a percentage of the total capture width (which definition is given in Equation A.17). Model tests are carried out to compare the calculated values to the experimental values. Some tests are carried out in still water, where small bulge waves are launched by a step input of small amplitude. Two types of capture widths are calculated; one is based on the internal pressures and the other is based on measurements of incident, reflected and transmitted waves. In these estimates, the end boundary conditions are included and the hysteresis losses and capture widths are calculated from the resulting hoop stress ( $\sigma_h$ ) in the tubes wall [12]. Furthermore, the set up and performance of the Power Take-off is sketched and the feasibility in terms of economics is examined.

The theory described in one of the papers includes more calculations on the elastic material and its behaviour. Hysteresis losses are included in the material, since the force in the material is assumed to be proportional to the strain and the rate of strain. This model for the material properties is called a Kelvin-Voigt

model, where the strain of such an visco-elastic material is given in Equation A.8. The bulging wave is evaluated in a still water case and when the tube will be excited by incoming waves. The differential equation prescribing the bulging wave including loss in the rubber (denoted by loss factor  $\beta$ ) is given as:

$$\frac{\partial^2 p_b}{\partial t^2} - \beta \frac{\partial^3 p_b}{\partial t^3} = \frac{1}{D\rho} \frac{\partial^2}{\partial x^2} \{p_b + p_w\} \quad (\text{E.4})$$

The radiation damping is already mentioned as a significant source of energy loss, but is not yet included in the simple calculations. A pressure amplification factor gives the ratio between the amplitude of the incoming wave and the bulge wave amplitude. A phase shift is observed between the incoming wave and the bulge wave of  $90^\circ$  at resonance. This means that the bulge wave is on its maximum size when the incoming wave is rising fastest. One main drawback of rubber as the tube's material is found by experiments. Aneurysms are formed beyond a critical pressure where the balance between wall tension and radius becomes unstable. Such an aneurysm is a bulge that is inconsistent over the radius. Reduction of the rubber percentage in the material is a possibility to prevent aneurysms and could be more cost efficient than a full rubber tube. The cost efficiency as well as the fatigue lifetime of a rubber tube are examined. The dynamic fatigue lifetime is coupled to the minimum strain, where the rubber is optimally stressed. In real life the stress level will become low from time to time and the rubber will be relaxed, which will decrease the lifetime of the rubber. Detailed calculations should be done to calculate the accurate lifetime of the rubber by including the fluctuating loads by the wave climate [23].

Experiments on the Anaconda WEC are carried out at the University of Southampton in 2012. A tube of 6.815 m length with a diameter of 0.215 m. The top of the bulge tube is placed 40 mm below the water surface and the rubber walls have a thickness of 1 mm. The tank is 60 m long, 3.7 m wide and has a water depth of 1.87 m in this experiments. To avoid aneurysms, inelastic fabric strips are glued longitudinally on the external surface of the tube. An exert pressure is applied of 0.350 m above the external free surface as shown in Figure E.5 in the pressure reading [14].

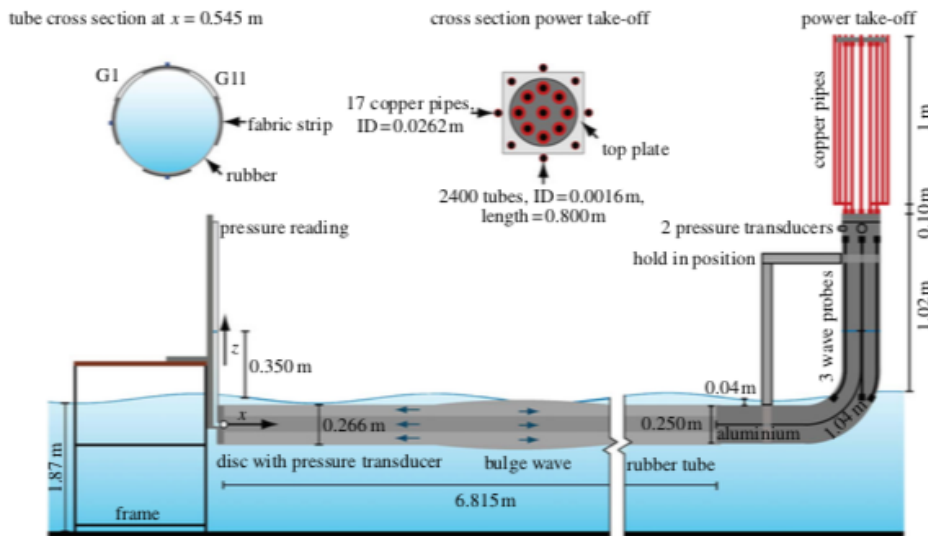


Figure E.5: Experimental setup used by Chaplin et al. for the Anaconda WEC [14].

Different measurements are identified, including the amplification of particle velocities and pressures over the length of the tube. A maximum amplification of 2.8 is found. The motion inside the tube should be expressed by three components of uniform amplitudes: the forward travelling bulge wave speed of  $\omega/v$  (for the incoming wave) and  $\omega/v_b$  (for the bulge wave) and the backward travelling wave at speed  $\omega/v_b$ . Their pressure amplitudes are given by  $|p_w^+|$ ,  $|p_b^+|$  and  $|p_b^-|$ , which are found by the estimated interfered values of the pressures inside the tube based on a least-square method. Reasonable results are found by comparison of this method with a formula based on the one-dimensional theory. For the hysteresis losses, a loss angle  $\delta = 9^\circ$  is used to compute results to compare to the experimental values [14]. This loss angle is related to the loss factor of Equation E.4 by  $\delta = \arctan(\beta\omega)$  [15, 23]. The agreement between this theoretical and experimental values is surprisingly good, where the tube is assumed to be straight and horizontal, and the diffracted and radiated

waves are neglected. Some other effects, such as a partial inelastic parts of the tube, longitudinal tension and the presence of the surrounding water are included in the theory. The PTO used in the experiments was adjustable by its impedance. Several measurements are carried out to tune the PTO with respect to the one-dimensional theory. The energy losses are increased by a few percents to include losses due to diffraction and radiation wave effects [14].

In 2011 Babarit and Ferrant investigated the statement of Chaplin et al. about neglecting the radiated and diffracted waves. A three-dimensional numerical seakeeping codes is adapted to cope with radial deformation of a submerged body, which is used to validate this statement [6]. The software of this boundary element software is based on linear potential theory, where the boundary value problem is solved in the time-domain [57]. The tube is discretised to a number of sections of equal length in this model, where the radial deformation is assumed to be uniform on each segment. Due to a step function which is defined for each flat panel, a potential is found for the elementary problem. By this potential, the mean pressures over the surface of each segment is found, including the added mass and damping terms. A second potential is derived for the bulge radiation problem, which is influencing the mean pressure, added mass and damping on the segments (over time). The mean hydrodynamic pressure measured on a section due to the diffraction of waves by the bulge is included in pressure term  $\bar{p}_{\gamma i}$  and the pressure due to the incoming waves is given as  $\bar{p}_{0i}$  on section  $i$ . Several plots are made where the total excitation pressure and radiation pressure are plotted over time. Two conclusions can be drawn from this study: the total excitation pressure grows along the tube and radiation is dominating the pressures from the middle of the tube up to the end of the tube. This means that radiation can not be neglected for positions further along the tube [6].

### SBM S3

The first document indicating a bulge wave energy device with energy transfer through the application of Electro Active Polymers (EAP) goes back to 2013, where Babarit et al. describe the numerical and experimental modeling of the S3 [7]. This S3 is a tube filled with pressurised water. The tube is placed directly beneath the free surface. An incident wave causes deformations of the tube and the waves will be progress in the free surface and inside the fluid-filled tube. The wave inside the tube is called a bulge and is initiated by a pressure difference between the inner and outer flow surrounding the tube.

An numerical model is developed to optimise the system and to define the dimensions of the system. The tube of length  $L$  is constructed from an elastic material with density  $\rho_{tube}$ . At equilibrium the radius of the tube is given as  $r_s$  at a depth of submersion  $z_s$  in Figure E.6<sup>2</sup>. This illustrates the set-up of the S3 submerged in waves. The thickness of the elastic wall is given by  $h_s$ , and the tube mass is defined as  $m_{tube} = 2\rho_{tube}\pi r_s h_s L$ .

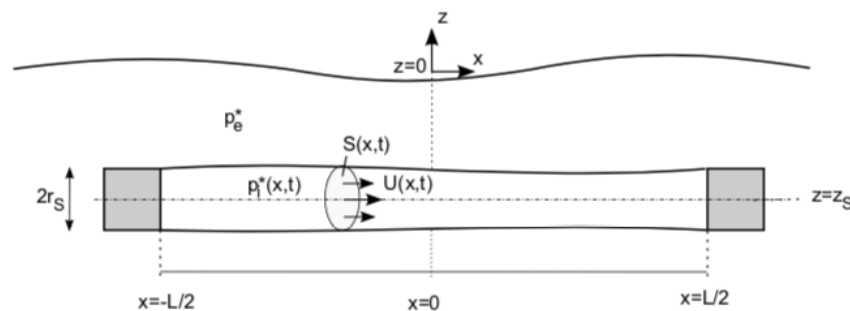


Figure E.6: Wave energy converter S3 submerged in waves [7, 8]

The model of Babarit et al. includes several assumptions [7, 8]:

1. The deformation of the tube is supposed to be homogeneous in radial direction. Therefore, the deformation only depends on the horizontal coordinate  $x$  and time  $t$ .
2. Along the axis of the tube, the tube is assumed to be undeformable. The horizontal movement of the tube can be identified as a rigid body motion (surge).

<sup>2</sup>At equilibrium the inner fluid and still water pressures are observed.

3. Both ends of the tube are closed by a rigid sealing. These sealings are the point where the system will be moored to the seabed.
4. The dynamic deformations of the system are assumed to be very small, so linear theory can be applied to the model.
5. Due to the previous assumption, the fluid velocities in the directions perpendicular to the axis of the tube are assumed to be small compared to  $u$ , given by  $v \approx w \ll u$ .
6. The pressure is assumed to be constant on each axial section, given by  $p_i = p_i(x, t)$ , which is composed of a (hydro)static and dynamic pressure terms.

In the numerical model of the wave energy device several aspects have to be included. Babarit defined three main components of the WEC:

- Inner fluid problem
- Outer fluid problem
- Structural problem, including the motion of the tube and its wall.

The governing equations of each of these submodels will deviate since the boundary conditions and assumptions of the S3 are different from the Anaconda's. Both of the models have a no-flow boundary condition at the bow of the tube, but the flow conditions differ at the stern of the tube. The Anaconda has a PTO at its stern, which gives a relationship between pressure and flow leaving and entering the tube. The stern boundary in the S3 is a no-flow condition. The numerical theory of the S3 is including longitudinal tension due to the Poisson effect in isotropic materials, while the theory of Farley et al. does not include this effect. The total system of the Anaconda is fixed, so it is not able to move horizontally, whereas the S3 is able to move horizontally. In the case of the Anaconda WEC, the model requires a calibration of the distensibility and losses by experimental data. Since these values depend on dimensions, it is not possible to predict the performance of the WEC based on tests carried out on model scale [8]. Another difference between the two models is the character of the material. In the models developed for the Anaconda WEC, the material is assumed to be visco-elastic as mentioned earlier. The material of the S3 WEC is visco-hyperelastic, which includes an elastic behaviour as prescribed by the Yeoh model. This model includes material parameters, which are found by a least square fitting of the Yeoh model on the experimental values [8, 23].

In their research document, Barbarit et al. refer to the similarities between the flexible wave energy converters and arteries, transferring the blood. A considerable amount of literature has been published on the fluid mechanics in arteries. These studies are interesting, but there are some significant differences, like the absence of the outer fluid, the tethering of the tubes, and the different geometrical characteristics of the distensible tube [8].

### Inner fluid problem

Since the fluid inside the tube is inviscid and incompressible combined with the assumption of the dominance of the axial velocity, neglecting the non-linear terms and the absence of other external forces, the momentum equation reduces to [15]:

$$\rho \frac{\partial u}{\partial t} = -\frac{\partial p_i}{\partial x} \quad (\text{E.5})$$

When the flow is assumed to be constant over the section, the continuity equation can be rearranged [8, 15]:

$$\frac{\partial(\rho S)}{\partial t} + \frac{\partial}{\partial x}(\rho S u) = 0 \quad \Rightarrow \quad \frac{\partial S}{\partial t} = -S_s \frac{\partial u}{\partial x} \quad (\text{E.6})$$

where  $S_s$  is the undisturbed cross-sectional area and  $p_i$  is the pressure inside the duct, given by  $p = p_b + p_w$  [15]. In the report of Babarit et al. the equation of momentum equation includes an extra effect, which is a viscous damping term related to wall friction with viscous damping coefficient  $B_r$  [8]:

$$\frac{\partial u}{\partial t} = -\frac{1}{\rho} \frac{\partial p_i}{\partial x} - \frac{B_r}{S_s} u \quad (\text{E.7})$$

### Outer fluid problem

The outer fluid problem is described by the linear potential theory, with the same assumptions as described

previously in Section C.1. This implies that the fluid can be described by a velocity potential which is composed of uncoupled components. These components are the incident wave potential, diffracted wave potential and the radiated wave potential [8]:

$$\Phi = \Phi_I + \Phi_D + \Phi_R \quad (\text{E.8})$$

These potential components can be treated as separate problems, where the diffraction and radiation potentials are solutions of the boundary value problems as described in Table E.1.

Diffraction problem	in $\Omega$	Radiation problem
$\Delta\Phi_D = 0$		$\Delta\Phi_R = 0$
$\frac{\partial\Phi_D}{\partial n} = -\frac{\partial\Phi_I}{\partial n}$	at sea bottom $S_{bottom}$	$\frac{\partial\Phi_D}{\partial n} = 0$
$\frac{\partial^2\Phi_D}{\partial t^2} + g \cdot \frac{\partial\Phi_D}{\partial n} = 0$	at free surface $S_{FS}$	$\frac{\partial^2\Phi_R}{\partial t^2} + g \cdot \frac{\partial\Phi_R}{\partial n} = 0$
$\frac{\partial\Phi_D}{\partial n} = -\vec{\nabla}\Phi_I \cdot \vec{n}$	on wet body surface $S_B$	$\frac{\partial\Phi_R}{\partial n} = -\vec{V} \cdot \vec{n}$

Table E.1: Boundary value problems for the diffracted and radiated wave problem in linear potential theory [8].

where  $\Phi_W$  is the incident wave potential, which will be prescribed in most of the cases. Once all of these components of the velocity potential are obtained, the dynamic pressure can be calculated for the outer pressure field. Babarit et al. divided this dynamic component in an excitation pressure  $p_{ex} = -\rho \left( \frac{\partial\Phi_W}{\partial t} + \frac{\partial\Phi_D}{\partial t} \right)$  and a radiation pressure  $p_{rad} = -\rho \left( \frac{\partial\Phi_R}{\partial t} \right)$ . The excitation pressure is a function of the incident and diffracted waves and the radiation pressure caused by the surge and bulge motions of the tube. The outer pressure  $p_e^*$  including the dynamic part ( $p_e$ ) and hydrostatic part is given as [8]:

$$p_e^* = \overbrace{p_{ex} - p_{rad}}^{p_e} - \rho g z \quad (\text{E.9})$$

### Structural problem

The governing equation in the structural problem is the linearised wall equation. A few assumptions are made in this linearised wall equation for a small piece of the tube wall. The tube mass is assumed to be small, therefore inertia effects will be neglected. The deformations are small, which complies with assumption 4 as mentioned before. The tube is thin-walled, which means that wall thickness  $h$  is small compared to radius  $R$  ( $h \ll R$ ). The tube is a straight horizontal cylinder at rest [8]. Babarit et al. found out that the deformations behaves non-linear with respect to the hoop stress  $\sigma_\theta$ .

Investigation into the forces working on a small piece of the elastic wall results in the linearised wall equation [8, 14, 23, 60]:

$$\begin{aligned}
 p_i &= \bar{p}_e - \frac{T_s}{4\pi S_s} \frac{\partial^2 S}{\partial x^2} + \frac{1}{DS} (S_s - S) + \frac{\rho}{S_s} \eta \dot{S} \\
 &= \underbrace{\bar{p}_e}_{\text{contour averaged outer pressure}} - \underbrace{\frac{T_s}{4\pi S_s} \frac{\partial^2 S}{\partial x^2}}_{\text{effect of longitudinal tension}} + \underbrace{\frac{1}{DS} (\delta S - \beta \dot{S})}_{\text{bulge pressure defined by [14]}}
 \end{aligned} \quad (\text{E.10})$$

where on the second line a comparison is made with the theory of Chaplin, Farley et al. They did not include the effect of longitudinal tension, but is mentioned to be significant for short bulge waves with high longitudinal wall tension [14].

The second part of the structural problem is the equation of motion in surge-direction. Since the fixed length of the tube in longitudinal direction is assumed, the tube is only allowed to move horizontally by a rigid body motion. Analysis of a free body diagram including the elastic part of the tube and both towhead forces at the bow and stern of the tube gives an equation of motion [8]:

$$M\ddot{x} = -2K_m x + (\Delta p_i - \Delta \bar{p}_e) S_s \quad (\text{E.11})$$

where  $M = m_{\text{tube}} + 2 \cdot M_{\text{towhead}}$  and  $K_m$  is the mooring stiffness coefficient. The  $\Delta p_i$  and  $\Delta \bar{p}_e$  are the internal and averaged outer pressure differences over the tubes length [7, 8].

The second part of the report written by Babarit et al. describes the mode shapes of the bulge wave along the tube. Two main assumptions are made to simplify these calculations; the bulge wave is defined in a still water environment ( $\bar{p}_e = 0$ ) and damping is neglected for the inner fluid and material behaviour ( $B_r = 0$  and  $\eta = 0 \rightarrow \beta = 0$ ). Moreover, the radiation effects are neglected to be able to solve the eigen modes analytically. These assumption are combined with the linearised wall equation, and result in a wave equation. This wave equation written for auxiliary variable  $\chi(x, t)$ , which time-derivative represents the inner flow velocity. The wave equation is defined as [8], where the grey terms are neglected (inner fluid damping and material damping). The blue term is included for the hydro-elastic response of the tube, but this term will be excluded in the first calculations for a still water environment:

$$\begin{aligned} \frac{\partial^2 \chi}{\partial t^2} - \frac{1}{\rho D} \frac{\partial^2 \chi}{\partial x^2} + \frac{1}{\rho D} \frac{1}{K_0^2} \frac{\partial^4 \chi}{\partial x^4} &= \underbrace{-\frac{1}{\rho} \frac{\partial \bar{p}_e}{\partial x}}_{=0} + \eta \underbrace{\frac{\partial^2 \dot{\chi}}{\partial x^2}}_{=0} + \underbrace{\frac{B_r}{S_s} \dot{\chi}}_{=0} \\ \frac{\partial^2 \chi}{\partial t^2} - \frac{1}{\rho D} \frac{\partial^2 \chi}{\partial x^2} + \frac{1}{\rho D} \frac{1}{K_0^2} \frac{\partial^4 \chi}{\partial x^4} &= 0 \end{aligned} \quad (\text{E.12})$$

Standard techniques as described in the report of Babarit et al. define the first 6 eigenmodes of the bulging tube (as shown in Figure E.7)<sup>3</sup>.

In Figure E.7 the natural periods of the bulging modes are included, where an increase in modal frequency results in a decreasing spatial period. Two types of modal shapes are investigated, which behave like a sine or cosine function of the spatial period ( $2L/l$ ). These bulging modes occur for a tube with boundary conditions like the S3, where the second type of bulging modes will not occur for fixed structures like the Anaconda WEC [7, 8].

Finally, Equation E.12 will be solved with neglecting damping and the incident wave. The previous mode shape functions are used as  $\chi_m$ , and are inserted in a time-dependent linear combination of these mode shapes. Combination of the equation of motion (Equation E.11) and the linearised wall equation (Equation E.10) results in a solution for the total hydrodynamic pressure. The radiation pressure distribution is found by solving the boundary value problem, which will be solved by a frequency-domain boundary Element method (BEM) solver like WAMIT or NEMOH [8]. The total hydrodynamic pressure is given as Equation E.13 for an incident wave of unit amplitude [8]:

$$\bar{p}_e(x, \omega) = \bar{p}_{ex}(x, \omega) + \sum_{m=1}^{\infty} (-A_m(x, \omega) \ddot{c}_m - B_m(x, \omega) \dot{c}_m) \quad (\text{E.13})$$

where  $\ddot{c}$  and  $\dot{c}$  are the deformation acceleration and velocity of the tube [8].

### Experimental tests

One of the papers mentioned in Appendix B for validation is the paper of Gerrard [29]. Experiments carried out on a fluid-filled deformable tube are described in this paper. The experiments are arranged to the theory developed by Womersley in 1955 [73]. This theory contains an infinitely long tube with a pulsatile flow in the tube, where two waves are present: (1) a pulsative wave which causes principally radial wall motions and (2) wall motions that are principally longitudinal. Two main drawbacks of this theory are the infinity of the tube, while in reality (and in the experiment) a finite tube will be used and the absence of the outer fluid in the theory. Since Gerrard also omitted the outer fluid, the influence of the driving incident wave is not included [29]. A reference is made to the comparison of linearized wave propagation models for arterial blood flow analysis written by Cox [17]. He compared several methods based on boundary assumptions for three subsystems: the fluid, the motion and the tube. Probably, one of the theories mentioned in this overview could be interesting to use for validation of the numerical model which will be developed.

Gerrard adapted the theory of Womersley for a finite cylinder with a relative high wall thickness/radius ratio. A value of approximately 0.3 can not be identified as a thin-walled anymore, while the theory of Womersley is designed for thin-walled elastic tubes. The oscillating flow inside the tube is driven by a piston moving

<sup>3</sup>These standard techniques are also described in Appendix F for new assumptions and boundary conditions, as described in Subsection E.2.3.

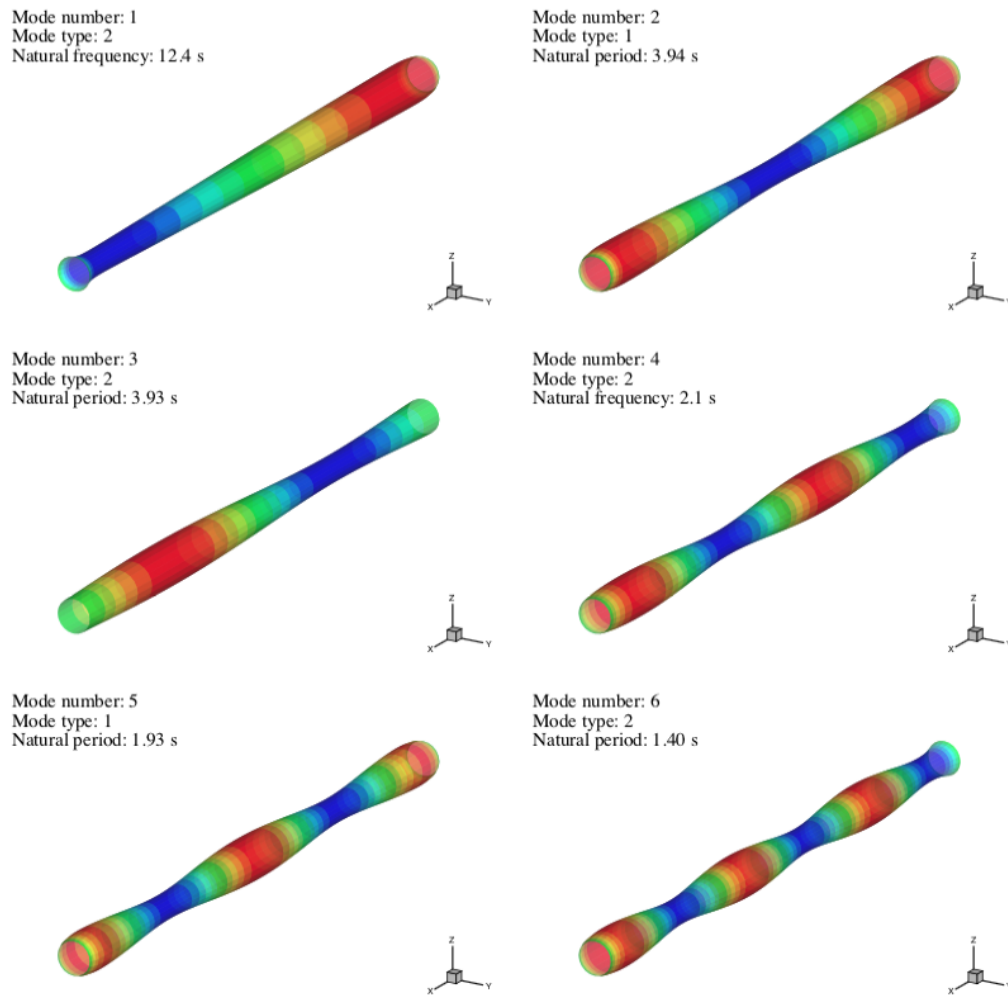


Figure E.7: First six eigenmodes of a tube of  $L = 10$  m,  $r_s = 0.274$  m,  $h_s = 0.01$  m and submergence  $z_s = -0.265$  m as found by Babarit et al. [8].

in an entrance length longer than one wavelength. This entrance length can not be included in the theory of Womersley, but is required for the experiments. The other end of the tube is closed, where the tubes are long enough to state that influence of the reflected wave is not significant anymore. The layout of the tube includes springs to support the tube with minimal longitudinal constraints, except for the fixed ends of the tube which are fixed. In addition to the supported measurements, experiments are carried out for tethered tubes where the longitudinal wall motion is absent. A complex Young's modulus is added to the theory which represents the viscoelasticity of the material [29]. The ratio between the real and imaginary parts of the Young's modulus is used as an input for the Womersley theory, with typical values of latex between 0.02 and 0.04. The results obtained by Gerrard are given for specific frequencies, dimensions and transmission factors of tethered tube [29].

The most recent work on a distensible tube wave energy converter is carried out by Smith in 2016 [60]. He used the concept of the Anaconda WEC to obtain a three-dimensional mathematical model to deal with the interaction between the incident gravity wave, radiated waves and bulge waves. The model is based on conservation of mass and momentum, where the backward travelling wave inside the tube will be neglected. The power take off at the end of the tube will not be included in the model, since all the information is travelling from the bow of the tube towards the stern. The wave spectrum of the sea is replaced by one single frequency, where a linear gravity wave is assumed. The mathematical problem exist of two parts, a periodic steady state which will give the solutions over large distances and a transient solution which implies the variations over

the length of the tube. For the steady state solution, three subsystems are obtained: the incident wave, the radiated wave and a bulge pressure. The transient solution investigates the radiated wave, bulge pressure and a bow boundary condition. The final solution consists of the incident wave potential and the potentials obtained for the periodic steady state and transient solutions. Pressures found by these potentials are validated with the experiments of Chaplin et al. [14, 60]. As a result of the derived potentials and pressures, the capture of energy could be analysed as well, which will result in a capture width (from Equation A.17). The obtained graphs of the capture width can be compared to the experiments of Chaplin et al. [14, 60].

### Longitudinal bending

Surprisingly, most studies in the field of a bulge wave energy converter have not dealt with bending of the tube to follow the wave profile. This effect is visible in nearly every illustration of the Anaconda wave energy converter (like on the cover) and the SBM S3 wave energy converter. Since the steepness of the incoming wave is small, which is a result of a gravity wave, the body will follow the waves. Smith states that the vertical translation of the tube due to passing gravity waves is not of primary concern, so he neglected this effect to simplify the problem [60]. In 2007 Chaplin et al. described the different ways of viewing the mechanism of the Anaconda, one of these mechanisms is the rubber tube to float directly beneath the free surface following the wave profile. The motions of the tube, rigid body motion and bulging motions are combined with the pressure due to waves and the hydrostatic pressure. A lot of terms do not extract power from the waves, as a result of time-averaged motion or by symmetry reasons [12]. Chaplin et al. state that the combination of a rigid-body velocity and bulging gives a maximum available power when phase angles between the rigid-body velocity and bulging motion are chosen suitable. The principle of extracting power from the ocean is claimed to originate from the varying buoyancy. This means that when the tube goes up, it bulges out and the waves have to do more work in lifting it. When it is going down, it does the opposite, so overall the tube extracts power from the waves [12].

Where Chaplin et al. state that the effects of rigid-body velocity combined with the bulging motion is the key factor in the principle of operation, the effect of rigid body motion is neglected by Smith [12, 60]. The assumption of the tube following the incoming wave is researched by Floor Spaargaren in her graduation research. She researched the response amplitude operator (RAO) of the SBM S3 as a function of wave periods. She states that for waves with a wave period shorter than 1.5 s, the heave RAO is less than 0.5 which means that the tube is not following the waves anymore. These results are found for a 10 m long flexible tube with an inflated diameter of 0.55 m [62].

Newman has described the wave effects on deformable bodies. In a paper, he highlights the difficulty to determine the 'natural' mode shapes of a hydroelastic problem, because the mode shapes are affected by the hydrodynamic pressure field and they can not be specified in advance [53]. Three options are given sorted by descending order in complexity. The superposition of mathematical mode shapes is the first option, where the mode shapes are sufficiently general and they comply with the physical motion. For a slender ship this process is described by Bishop and Price, where a more simply application is given for a uniform beam. A simpler method to define the hydroelastic modes of a tube can be found by orthogonal polynomials, but they do not match the boundary conditions and models the physics correctly. The third method is the most complex method. Newman suggested to define the body as  $N$  separate bodies which all have 6 degrees of motion. When the separate bodies are deformable themselves, even more than  $6N_{mode}$  modes of the global body are found [53]. This means that the interaction between waves and an elastic tube is complex to examine and should be simplified to reduce the complexity.

### E.2.2. Methodology of bulging WEC

The previous pages are used to investigate the knowledge about bulge wave energy converters. The work of Farley, Rainey and Chaplin [12–14, 21–23] is developed according to experiments. Therefore, the validity of their argumentation and formulae is questionable, since references are missing in their work. Results found for the Anaconda WEC serve as a reference guide in the development of a numerical model that describes the hydro-elastic response of a bulge WEC in regular waves.

The work of Babarit et al. [8] will be used for the bulging motion of the tube. The boundary conditions will be adapted, to simplify the model and the FCFM method will be used to add radiation loads to the model. Longitudinal tensions will be excluded in the first version of the model, but it is included for later versions. As described by Lighthill [44], the longitudinal tension can also be included in the definition of the distensibility of the tube, which could be a possibility for this model. Differential Equation E.12 is used as basis for this research, where the hydro-elasticity is of main interest. The steps in the method of Babarit et al. [8] are clear,

and adaptations are relatively easy to implement.

The model includes bending, where superposition of modes is used as a method to model the deformable tube in waves, which is based on the research of Newman [53], Fathi et al. [24] and Bishop and Price [9].

In both deformation modes, bending and bulging, the diffraction effects are neglected. Other boundary conditions and assumptions for the model are described in Subsection E.2.3

### E.2.3. Assumptions and boundary conditions

Since the Frank Close Fit method is a relatively fast and independent of cross-sectional shapes, this FCF method will be extended to deal with the hydro-elastic behaviour of a bulging wave energy converter. The assumptions and boundary conditions will be defined in five parts:

- The incident wave
- Material properties of the tube
- The bulging wave
- Bending of the entire tube
- The radiated and diffracted waves

In these components of the research, the radiated and incident wave components will be evaluated in a two-dimensional coordinate system similar to the theory of Frank (as shown in Figure E.1). The other components will be evaluated in a earth-fixed coordinate system. The assumptions and boundary for each component of the model are described in the following five paragraphs.

#### The incident wave

The incident wave is assumed to be a regular gravity wave. This implies that the wavelength is long compared to the waveheight. The fluid outside the tube is furthermore assumed to be incompressible, irrotational and inviscid. The incoming wave will be described by an incident wave potential  $\Phi_W$  [41]:

$$\Phi_W = \frac{\zeta_I \cdot g}{\omega} \frac{\cosh(v(x+h))}{\cosh(vh)} \cos(\omega t - v z) \quad (\text{E.14})$$

$$\zeta = \zeta_I \cdot \sin(\omega t - v z) \quad (\text{E.15})$$

where the dispersion relation should be provided as [60]:

$$\frac{g v}{\omega} \tanh(h) = 1 \quad (\text{E.16})$$

where  $h$  denotes the depth of the fluid domain. Since the FCFM is validated for oscillations in deep fluid, the Equations E.14 and E.16 will be simplified as well for deep fluids.

The pressure due to the incident wave will be given by the linearized Cauchy-Lagrange integral [60].

#### Material properties of the tube

The core material of the tube will be rubber, a material that is understood properly, and which material characteristics are available. The type of rubber will be chosen related to research used for validation and verification of the model. The material is assumed to be purely elastic, since the values of a visco-elastic material are estimated by previous research and are used as a fitting parameter in the work of Babarit et al. [8] for example. In the first version of the model, the influence of longitudinal stress will be neglected. The longitudinal tension is included in the differential equation (which is the second terms of Equation E.12) and is used in higher versions of the model to improve the hydro-elastic response of the tube in waves. The longitudinal stress will be important in a tube of a fixed length, which is assumed in this model.

Aneurisms in the material are beside the scope of this research. Investigation into prevention of aneurisms is studied by several authors, where solutions for the problem are presented [23].

#### The bulging wave

For the bulging wave we assume the fluid velocity to be dominant in the  $z$ -direction, where a axi-symmetric flow can be assumed inside the tube. This means that the momentum and continuity equation reduce to Equation E.5 and E.6 without the effects of longitudinal tension. Therefore deformations of the tube due to the bulging are in only the radial direction and the cross-section remains circular. The radius of the tube will

increase and decrease as a result of the bulging. The bulging deformations itself are assumed to be small related to the tubes radius and even smaller compared to the tubes length. The tubes wall is thin, where it thickness is small with respect to the radius of the tube. The tubes mass is assumed to be small, so that inertia effects can be neglected in the wall equation [8]. In the wave equation (Equation E.12) the inertia is included by a rearrangement of the mass terms. The fluid inside the tube is assumed to be incompressible and irrotational. The pressure acting on the wall is a combination of the incident wave pressure ( $p_W$ ) and the pressure due to the radiation of waves ( $p_R^{(m)}$ ), where  $m = 3$  denotes the bending motion and  $m = 4$  is used for the bulging motion. The pressure acting on the wall is coupled to the deformation of the cross-section by the differential equation as defined by Babarit et al. (in Equation E.12).

The bulging of the tube over the length of the tube will assume to be linear as well. This means that dividing the tubes length into  $N$  segments, like a strip theory method. For each segment the deformation is assumed to be constant. Mode shapes will be observed and mode superposition is used to define the total deformation of the tube.

The tube is assumed to be fixed at the bow and stern, where the ends have a fixed area  $S_0$ . These boundary conditions could influence the bending modes of the tube as well as the influence of the longitudinal tension.

### Bending of the entire tube

As mentioned in the literature review of Section E.2.1, the bending of the tube is neglected in most research reports. In this report, the bending of the tube is assumed to follow the waves, which means that the shape of the tube can be described by a linear wave with the same wavenumber and frequency as the incident wave. Following of the waves is assumed to be valid for a response amplitude operator (RAO)  $> 0.5$ , as mentioned by Spaargaren. This RAO value is coupled to the wave periods of the incident wave coupled to the system. This effect is found for large wavelengths [62]. The range of observed frequencies will be adapted to these results.

Since the statement of Chaplin et al. about the interaction between the rigid-body velocity and bulging cylinder is not founded by clear formulations and references, this interaction is assumed to be uncoupled. The rigid-body velocities along the tube will vary, but are related to each other by the incident wave the tube follows. Similar to the extrapolation of the bulge wave over the tube length, the influence of the bending over the tube will be calculated by a matrix. This matrix will relate the longitudinal coordinate of the cross-section to the frequency of the incident wave.

### The radiated and diffracted wave

As mentioned by the bending of the tube, the bulging motion and rigid body are assumed to be uncoupled. Since both can be described by linear theory, a superposition method is used to find the pressure of both radiated wave profiles. This summation of the pressure due to radiated waves is given as:

$$p_{rad} = p_{r,b} + p_{r,rb} \quad (E.17)$$

where the radiation due to bulging is denoted by the subscript  $r,b$  and the radiation due to the rigid-body velocity/bending by  $r,rb$ .

Diffracted waves will be neglected in this research since the effects for a slender tube operating in head waves will be small. Furthermore, these diffraction effects will be located at the bow and stern of the body, which are typical three-dimensional effects. Since the numerical method is principally two-dimensional, the implementation of diffraction would increase the complexity of the model.

### Validation and verification

Validation of the numerical model is not possible with one paper, but it should be a combination of several resources. The bending model could be verified with a model as defined by Fathi, Newman and Lee [24]. These results do not include specific information about the geometrical values, but the general response of a tube can be found by these results. In the research of Fathi et al. citeFaltinsen1994, two 'surge-pressure' modes are observed, which can be interpreted as 'bulging' modes. These two modes and the corresponding incident and radiated wave load can be verified up to a certain level.

The work of Babarit et al. [8] is the second source of verification and validation. Since this research is the basis of the modal analysis of 'bulging', the results can be compared in detail. This research does not include bending, which has to be verified with the results of Fathi et al.[24].

Probably the experiments of Chaplin et al. [14] could give more insight into the efficiency of a bulging WEC operating in waves. The dimensions of the Anaconda WEC differ from the bulge WEC as observed in the

model, which makes it difficult to make a valid comparison between the results of Chaplin et al. [14] and the numerical model.

### E.3. Conclusions

In this section two secondary questions are considered, which are formulated in Section A.2:

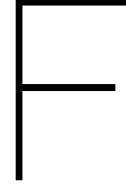
1. *Which assumptions need to be made to describe a bulge wave energy converter by 2D potential theory?*

For the bulging mode, the kinematic boundary condition is rewritten for the normals of the contours elements. The directional cosines in the FCFM are adapted into the normals to the elements pointed into the surrounding fluid. Symmetrical tools, such as described in Appendix D, have to be sidestepped. A vector combination of the heave and sway oscillations represents the bulging mode and therefore the bulging radiation pressures are also a vector combination of the heave and sway radiation coefficients. The bending modes of the bulge WEC in still water, are represented by the heave motion of each element along the tube.

2. *How can Frank's close-fit method be adapted to deal with deformable bodies in still water?*

In this Appendix, several theories are examined and a final methodology is presented in Subsection E.2.2. This methodology is based on the numerical method as defined by Babarit et al. [8], with some adaptation. Viscous effects due the wall's material and inner fluid are neglected as well as diffraction effects, which are assumed to be small. Bending of the model is included, since the tube is assumed to deform along the longitudinal axis as well.

This Appendix provides some simple adaptations to the Frank close-fit method and literature relating to modal analysis of a bulge WEC operating in waves. The Appendix that follows moves on to the implementation of the FCFM in the modal analysis of the bulge WEC in regular waves.



# Modal analysis of Bulge WEC

The modal analysis of the Bulge WEC is subdivided into a purely bending and a purely bulging analysis. In Section E.1 the bending of the beam is determined by an Euler beam model. The bulging modal analysis is described in Section E.2, where the model description of Babarit [8] is used.

## E.1. Pure bending

For the bending modes of the bulge wave energy converter, the method of slender beams (Euler beam model) is used to determine the bending modes. The normal mode method is used to define the deflection due to the fluctuating load on the beam. This method is described in the reader of course MT3402 [35] and used in this section to define the response of the beam to incident waves of amplitude  $A_I$  and wave frequency  $\omega_I$ .

### Dry bending mode

The Equation of Motion (EoM) of a slender (cylindrical) beam without a surrounding fluid is given as [35, 53, 55]:

$$m(x) \frac{\partial^2 w}{\partial t^2} + \frac{\partial^2}{\partial x^2} \left( EI(x) \frac{\partial^2 w}{\partial x^2} \right) = p(x, t) \quad (\text{E.1})$$

where  $m(x) = m$  is assumed to be constant since the beam has a homogeneous mass distribution along the length and a constant cross-sectional area. This implies directly that the area moment of inertia  $I(x) = I$ , which is given for a cylindrical cross-section as  $I_{circ} = \frac{\pi}{4} (r_{out}^4 - r_{in}^4)$ . The external load due to the incoming wave is given by the function  $p(x, t)$ , which will be specified in a particular solution. The total solution will be composed of a homogeneous solution (where  $p(x, t) = 0$ ) and a particular solution, where  $p(x, t)$  is a function of space and time.

### Homogeneous solution

For a homogeneous beam, the eigenmodes and dry eigenfrequencies will be defined by the homogeneous solution for the Equation of Motion:

$$\frac{\partial^2 w}{\partial t^2} + \frac{EI}{m} \frac{\partial^2 w}{\partial x^2} = 0 \quad (\text{E.2})$$

We assume the deflection to be a function of space and time, described by  $w(x, t) = W(x)T(t)$  where  $T(t) = e^{-i\omega t}$ . This function inserted into Equation E.2 which gives the equation of the vibrating beam:

$$\frac{d^4 W(x)}{dx^4} - k^4 \cdot W(x) = 0 \quad (\text{E.3})$$

where  $k^4 = \frac{m\omega^2}{EI}$ . The space dependent function is assumed to be of the form  $W(x) = \tilde{W} \cdot e^{nx}$ , which after substitution results in:

$$(n^4 - k^4) \cdot e^{nx} = 0 \quad (\text{E.4})$$

Four values for  $n$  are found and are substituted into the Equation for the vibration mode:

$$\begin{aligned} n_1 = k \quad n_2 = -k \quad n_3 = jk \quad n_4 = -jk \\ W(x) = C_1 \cdot \sin kx + C_2 \cdot \cos kx + C_3 \cdot \sinh kx + C_4 \cdot \cosh kx \end{aligned} \quad (E5)$$

The values of the constants  $C_1$  until  $C_4$  will be defined by the boundary conditions for a free-free beam, which is a beam where both ends are free to move. These boundary conditions are given at the bow and stern of the beam ( $x = 0$  and  $x = L$ ). At both ends the bending moment ( $M_{bend}$ ) and shear forces ( $V_{shear}$ ) are equal to zero. At the bow, the boundary conditions result in:

$$\begin{aligned} \frac{1}{k^2} \frac{\partial^2 W}{\partial x^2} = M_{bend}(x=0) = 0 = -C_2 + C_4 \rightarrow C_4 = C_2 \\ \frac{1}{k^3} \frac{\partial^3 W}{\partial x^3} = V_{shear}(x=0) = 0 = -C_1 + C_3 \rightarrow C_3 = C_1 \end{aligned} \quad (E6)$$

At the stern, the boundary conditions give the following system of Equations:

$$\begin{aligned} \frac{1}{k^2} \frac{\partial^2 W}{\partial x^2} = M_{bend}(x=L) = C_1 (-\sin kL + \sinh kL) + C_2 (-\cos kL + \cosh kL) = 0 \\ \frac{1}{k^3} \frac{\partial^3 W}{\partial x^3} = Q_{shear}(x=L) = C_1 (-\cos kL + \cosh kL) + C_2 (\sin kL + \sinh kL) = 0 \end{aligned} \quad (E7)$$

which is found to be valid for the characteristic value problem<sup>1</sup>  $\cos kL \cosh kL = 1$ . The first values for  $kL$  are found by this characteristic value problem:

$$\begin{aligned} k_0 \cdot L = 0 \quad (\text{represents the rigid body mode}) \\ k_1 \cdot L \approx \pm 4.73 \rightarrow \omega_2 = (\pm 4.73)^2 \cdot \sqrt{\frac{EI}{m \cdot L^4}} \\ k_2 \cdot L \approx \pm 7.85 \rightarrow \omega_3 = (\pm 7.85)^2 \cdot \sqrt{\frac{EI}{m \cdot L^4}} \\ k_3 \cdot L \approx \pm 11.0 \rightarrow \omega_4 = (\pm 11.0)^2 \cdot \sqrt{\frac{EI}{m \cdot L^4}} \\ k_4 \cdot L \approx \pm 14.1 \rightarrow \omega_5 = (\pm 14.1)^2 \cdot \sqrt{\frac{EI}{m \cdot L^4}} \end{aligned} \quad (E8)$$

For each of the eigenfrequencies a mode shape function is given [55]:

$$\begin{aligned} W_n(x) = C_n [\sin k_n x + \sinh k_n x + \alpha_n (\cos k_n x + \cosh k_n x)] \\ \text{where } \alpha_n = \left( \frac{\sin k_n L - \sinh k_n L}{\cosh k_n L - \cos k_n L} \right) \text{ for } n = 1, 2, \dots, N \end{aligned} \quad (E9)$$

The first 5 (normalized) eigenmodes are presented in Figure F2 as a function of length. The mode shapes are normalised and they are orthogonal with respect to each other. These five eigenmodes are chosen with respect to the coupled eigenfrequencies which are calculated by the characteristic equation of Equation F8. These eigenfrequencies, also called natural frequencies, have to be in the range between 1 and 8 Hz.

<sup>1</sup>The characteristic value function is determined by the determinant of the system of equations in a matrix form. The determinant of the square matrix should be equal to zero, where the values of the coefficients are not described.

### Particular solution

Since the eigenfrequencies and mode shapes are defined, the forced oscillation can be evaluated. For the particular solution, the load  $p(x, t)$  is included in Equation E1. A combination of mode shapes is used in the normal mode method, where the function  $y(x, t)$  is a summation of two functions of space and time [35]:

$$w(x, t) = \sum_{n=1}^{\infty} q_n(t) W_n(x) \quad (\text{E10})$$

where  $W_n(x)$  is the normalised eigenmode and  $q_n$  represents the normal coordinates depending on time. Due to orthogonal properties of the normalised eigenmodes, we get the equation of motion [35]:

$$m\ddot{q}_n + EI \cdot k_n^A q_n = \int_{x=0}^L \eta_n \cdot p(x, t) dx \quad (\text{E11})$$

To continue with this Equation of Motion,  $p(x, t)$  should be described by a combination of two separate time- and space-dependent functions:  $p(x, t) = P(x) \cdot T(t)$ , where  $T(t) = e^{-i\omega t}$  and function  $q_n(t) = \zeta_n \cdot e^{-i(\omega t + \theta)}$ . The right-hand-side of Equation E11 can be calculated as [35, 55]:

$$\int_{x=0}^L \eta_n \cdot P(x) dx = \Gamma_n \quad (\text{E12})$$

The Equation of Motion simplifies to:

$$\ddot{q}_n + \frac{EI}{m} \cdot k_n^A q_n = \frac{1}{m} \Gamma_n T(t) \quad (\text{E13})$$

where  $k_n^A = \frac{m}{EI} \cdot \omega_n^2$ . Therefore Equation E13 reduces to:

$$-\omega^2 \zeta_n + \omega_n^2 \zeta_n = \frac{1}{m} \Gamma_n \Rightarrow \zeta_n = \frac{1}{1 - \left(\frac{\omega^2}{\omega_n^2}\right)} \cdot \frac{\Gamma_n}{m\omega_n^2} \quad (\text{E14})$$

where  $\zeta_n$  could be a complex number due to the phase difference as given in the definition of  $q_n(t)$ .

### Hydro-elastic bending mode

Since the bulge wave energy converter is surrounded by fluid and excited by an incoming wave, the coupled modes between the outer fluid, structure and wall equation has to be observed. The problem is still a two-dimensional water-wave problem, where bending will be evaluated as a vibration mode. Bending of the beam will be solved by the Euler-Bernoulli beam theory, where the load is described as the pressure resulting from potential theory describing the surrounding fluid:

$$\begin{aligned} m \frac{\partial^2 w}{\partial t^2} + EI \frac{\partial^2 w}{\partial x^2} &= F_{wa} \\ &= \int_{C_0} -p \cdot \vec{n} dC \\ &= \int_{C_0} \rho \frac{\partial \Phi(x, z, t)}{\partial t} \cdot \vec{n} dC \end{aligned} \quad (\text{E15})$$

where  $\Phi(x, z, t)$  is the time- and space-dependent potential consisting of:

$$\begin{aligned} \Phi(x, z, t) &= \text{Re} \left\{ \phi(x, z) \cdot e^{-i\omega t} \right\} \\ &= \text{Re} \left\{ (\phi_W(x, z) + \phi_R(x, z) + \phi_D(x, z)) \cdot e^{-i\omega t} \right\} \end{aligned} \quad (\text{E16})$$

which are the time-independent wave ( $\phi_W$ ), radiation ( $\phi_R$ ) and diffraction ( $\phi_D$ ) potential.

Since the bulge WEC is operating in the region of incoming waves where diffraction force is assumed to be not significant, the differential equation reduces to:

$$\begin{aligned} m \frac{\partial^2 w}{\partial t^2} + EI \frac{\partial^2 w}{\partial x^2} &= F_{FK} + F_R^{(4)} \\ &= \int_{S_0} p_i \cdot \vec{n} dS + F_R^{(4)}(x, \omega) \end{aligned} \quad (\text{E17})$$

where  $F_{FK}$  is the Froude-Krilov force due to the incoming waves and  $F_R^{(4)}$  is the radiation force for the bending mode (denoted by  $m=4$ ). The pressure due to the incoming wave  $p_W$  integrated along the tube's contour is known as the Froude-Krilov force component and is defined as:

$$\begin{aligned} p_{W,i} &= -\rho \frac{\partial \Phi_i}{\partial t} \\ &= -\rho \frac{\partial}{\partial t} \left( \frac{\zeta_I g}{\omega} e^{kz} \cdot e^{ikx} \cdot e^{-i\omega t} \right) \\ &= i\rho \zeta_I g e^{kz} e^{ikx} e^{-i\omega t} \end{aligned} \quad (\text{F.18})$$

where the pressure of the incoming wave depends on the  $x$ -position along the beam, the depth of each panel over the cross-sectional contour and the frequency. The incident wave pressure ( $p_{W,i}$ ) is averaged over the cross-sectional contour by the geometry description of the FCFM. The time-independent incident wave pressure of Equation F.18) is rewritten into:

$$\bar{p}_W(x, t) = i\rho \zeta_I g e^{ikx} \cdot e^{-i\omega t} \int_{C_0} e^{kz} \cdot n dC \quad (\text{F.19})$$

The integral of Equation F.19 is defined by the contour-averaging iteration implemented in the FCFM, which returns a constant for a certain cross-sectional area.

The generalised excitation force is defined as the integral of the contour-averaged incident wave over the (deformed) length of the tube [10, 69]:

$$F_{FK,n} = -i\rho g \zeta_I \int_L W_n \cdot e^{ikx} dx \cdot \int_{C_0} e^{kz} n_n dC \cdot e^{-i\omega t} \quad (\text{F.20})$$

Which is the solution of the integral in Equation F.12, without the time-dependent factor  $e^{-i\omega t}$ . The  $W_n$  is giving the normal direction in the longitudinal direction, where  $n_n$  gives the directional cosine over the cross-sectional contour. The radiation force of Equation F.17,  $F_R^{(4)}$  is the radiation force calculated in the FCFM for bending, as given in Equation C.28. This radiation force is a combination of the Added mass and Damping coefficient matrices with the acceleration and velocity amplitudes of the motions. Implementation of Equation F.18 and the radiation force into Equation F.17 looks the same as the differential equation for a particular solution. The same routine is used for the particular solution (of Equation F.11) and will result in:

$$m \sum_{n=1}^N \ddot{q}_n W_n + EI \cdot k_n^4 \sum_{n=1}^N q_n W_n = \bar{p}_i(x, t) - \sum_{n=1}^N A_n(\omega_n) \ddot{q}_n - \sum_{n=1}^N B_n(\omega_n) \dot{q}_n \quad (\text{F.21})$$

Equation F.21 can be transformed into a system of equations by the orthogonal properties of the eigenmodes. Multiplication of all of the individual components of Equation F.21 with mode shape  $W_m$  and integration over the length of the tube will result in:

$$\begin{aligned} m \sum_{n=1}^N \int_{x=0}^L \ddot{q}_n W_n W_m \cdot dx + EI \cdot k_n^4 \sum_{n=1}^N \int_{x=0}^L q_n W_n W_m \cdot dx &= \int_{x=0}^L \bar{p}_i(x, t) \cdot W_m dx \\ - \sum_{n=1}^N \int_{x=0}^L A_n(\omega_n) \ddot{q}_n W_m \cdot dx - \sum_{n=1}^N \int_{x=0}^L B_n(\omega_n) \dot{q}_n W_m \cdot dx & \end{aligned} \quad (\text{F.22})$$

where for the dry modes (and also wet modes)<sup>2</sup>, the orthogonal relationship holds:

$$\int_{x=0}^L W_n W_m \cdot dx = \begin{cases} 1 & \text{if } n = m \\ 0 & \text{if } n \neq m \end{cases} \quad (\text{F.23})$$

This will be implemented into the system of Equations which will be written in a matrix format:

$$M_{nm} \ddot{q}_n + A_{nm}(\omega) \dot{q}_n + B_{nm}(\omega) q_n = F_{FK,n} \quad (\text{F.24})$$

<sup>2</sup>Since the 'wet' modes are not coupled, these mode shapes are exactly the same as the 'dry' mode shapes and they are still orthogonal. The difference between the 'dry' and 'wet' mode shapes is the natural frequency that excite the mode shapes.

where  $K_{nn} = EI \cdot k_n^4$  and  $(F_{w,FK})_m$  is the Froude-Kriloff force due to the incoming wave for every mode  $m$ . The matrices  $M_{nm}$  and  $K_{nm}$  are diagonal matrices, since the different modes are not coupled (and the orthogonal properties hold for these matrices). Diagonal matrix coefficients are also indicated by  $M_{nn}$  and  $K_{nn}$ , since the subscripts denote the index of the matrix elements.

### Homogeneous solution

The 'wet' natural frequency will be defined for an undamped system, which means that the radiation damping matrix  $B_{nn}$  will be excluded from the equation and the force due to the incoming wave  $X_m$  is set to zero:

$$(M_{nm} + A_{nm}(\omega)) \ddot{q}_n + K_{nm} q_n = 0 \quad (\text{F.25})$$

Since  $q_n$  is a harmonic equation, the system of Equations will be a function of  $\varphi_n$ , which is the eigenvector of the eigenvalue problem [48, 50, 55]:

$$[K_{nm} - (\omega_n^{wet})^2 \cdot (M_{nm} + A_{nm}(\omega_n^{wet}))] \varphi_n = 0 \quad (\text{F.26})$$

which is a non-linear equation because of the frequency-dependence of the added mass matrix. To solve this issue, we will use an iterative process to define the values of  $\omega_n^{wet}$  and the eigenvector  $\varphi_n$ . The iterative process is shown in Figure F.1. The added mass of the system is included, but the off-diagonal terms in the added mass matrix  $A_{nm}$  are not included. This implies that the different modes of vibration are not coupled to each other and the modes still stay the same<sup>3</sup>. The matrices  $M_{nm}$  and  $K_{nm}$  will be the same in each iteration step for uncoupled modes, so these matrices are calculated in the begin of the routine. Since the added mass and radiation damping are related to the eigenfrequency of the system, these values should be defined in each iteration step. These matrices are calculated for every iteration [9, 50]:

$$(A_{nm})^{(i-1)} = \int_{x=0}^L a^{(3)} \left( (\omega_n^{wet})^{(i-1)} \right) \cdot (W_n^{wet})^{(i-1)} \cdot dx$$

$$(B_{nm})^{(i-1)} = \int_{x=0}^L b^{(3)} \left( (\omega_n^{wet})^{(i-1)} \right) \cdot (W_n^{wet})^{(i-1)} \cdot dx$$

and

$$M_{nm} = M_{nm}^{str} = \begin{bmatrix} m & 0 & \cdots & 0 \\ 0 & m & \cdots & 0 \\ \vdots & \vdots & \ddots & \vdots \\ 0 & 0 & \cdots & m \end{bmatrix} \quad \text{and} \quad K_{nm} = K_{nm}^{str} = EI \cdot \begin{bmatrix} k_1^4 & 0 & \cdots & 0 \\ 0 & k_2^4 & \cdots & 0 \\ \vdots & \vdots & \ddots & \vdots \\ 0 & 0 & \cdots & k_{Nmode}^4 \end{bmatrix}$$

The next step is the determination of the updated 'wet' eigenfrequencies and eigenvectors. These values are found by the Matlab-function  $[(\varphi_n)^{(i)}, ((\omega_n^{wet})^{(i)})^2] = \text{eig}(\text{inv}(M_{tot}) * K_{tot}, \varphi)$ , where the function gives the normalised eigenvectors for  $\varphi_n$ . The following steps are described in Figure F.1, where the criteria for convergence is set to  $\varepsilon = 1 \cdot 10^{-12}$ . As a result of this iteration, the values for the 'wet' eigenfrequencies and eigenmodes are found. Note that the 'wet' eigenmodes are exactly the same as the 'dry' eigenmodes since there is no coupling between the hydrodynamic coefficients of the bending modes. The wet modes are presented in Figure F.2 and the 'dry' and 'wet' eigenfrequencies of the modes are presented in Table F.1.

### Particular solution

Since the resulting mode shapes are found, the last step is the definition of the modal coordinates ( $\zeta_n$ ), which can be identified by the linear system of Equations [48, 50]:

$$\sum_{m=1}^N [-\omega^2 (M_{nm} + A_{nm}) - i\omega B_{nm} + K_{nm}] \zeta_n = F_{FK,n}(\omega) \quad (\text{F.27})$$

where the force contribution is given in Equation F.20. The solution is found by Equation F.27. For each

<sup>3</sup>Since the off-diagonal terms of added mass are not included, the modes are still orthogonal, where we see that the 'wet' eigenmodes are the same as the 'dry' eigenmodes. The eigenvector  $\varphi_n$  denotes the contribution of each dry mode shape, which is in this case one zero, completed with zeros. Since the matrix  $A_{nm}$  (and therefore  $B_{nm}$ ) are uncoupled and orthogonal, these matrices are diagonal matrices.

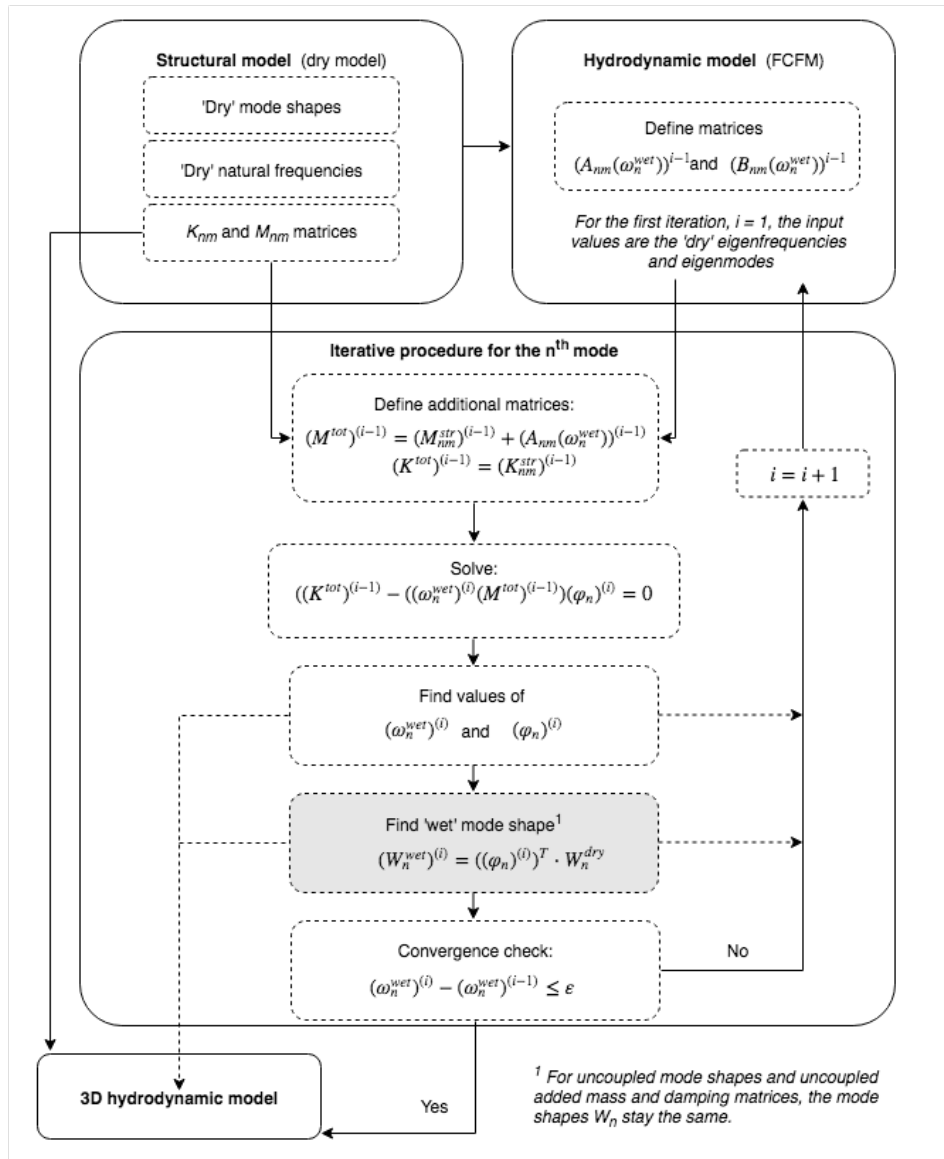


Figure E.1: Scheme of the iteration procedure and its coupling to the FCFM for the bending model. The value for the convergence test is set to  $\varepsilon = 1 \cdot 10^{-12}$ .

(Adapted from Loukogeorgaki et al., Fig. 4 [48])

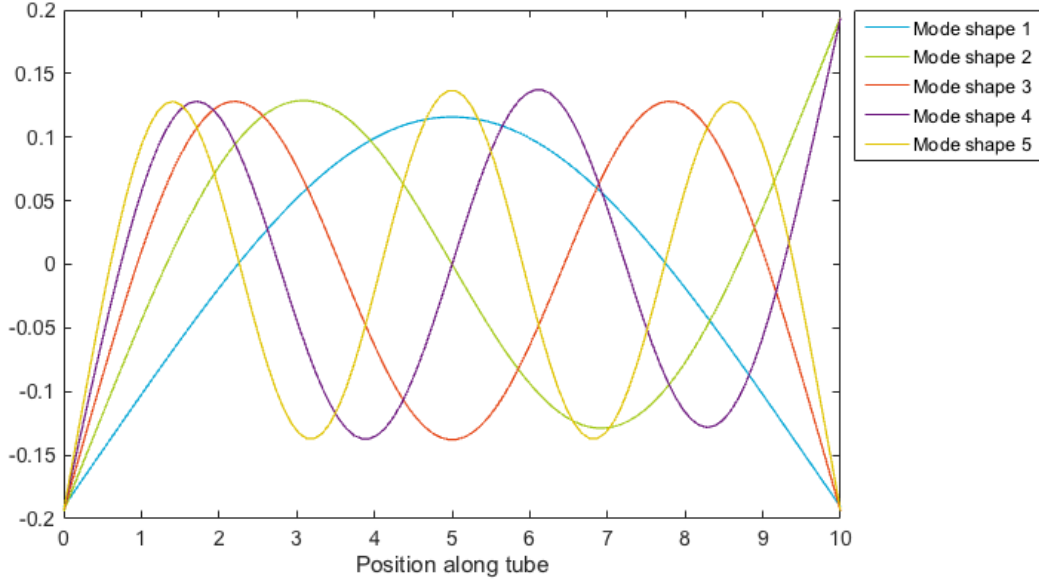


Figure E.2: First 5 normalized 'wet' eigenmodes of bending mode.

Mode	'Dry' eigenfrequency $\omega_n^{dry}$ (Hz)	'Wet' eigenfrequency $\omega_n^{wet}$ (Hz)
1	0.522	0.453
2	1.440	1.230
3	2.283	2.351
4	4.667	4.372
5	6.971	6.755

Table E.1: 'Dry' and 'wet' eigenfrequencies of the 5 bending modes of a bulge WEC with dimension given in Table F.2.

frequency of the incoming wave, the modal coordinates are determined according to [35, 58]:

$$\begin{aligned}
 (-i\omega)^2 \cdot (M_{nm} + A_{nm}) \cdot \zeta_n \cdot e^{-i\omega t} + (-i\omega) \cdot B_{nm} \cdot \zeta_n \cdot e^{-i\omega t} + K_{nm} \cdot \zeta_n \cdot e^{-i\omega t} &= F_{FK,n} \cdot e^{-i\omega t} \\
 (-i\omega)^2 \cdot \zeta_n \cdot e^{-i\omega t} + (-i\omega) \cdot \frac{B_{nm}}{M_{nm} + A_{nm}} \cdot \zeta_n \cdot e^{-i\omega t} + \frac{K_{nm}}{M_{nm} + A_{nm}} \cdot \zeta_n \cdot e^{-i\omega t} &= \frac{F_{FK,n}}{M_{nm} + A_{nm}} \cdot e^{-i\omega t} \\
 -\omega^2 \cdot \zeta_n - i \cdot \frac{B_{nm}\omega}{M_{nm} + A_{nm}} \cdot \zeta_n + \omega_m^2 \cdot \zeta_n &= \frac{F_n}{M_{nm} + A_{nm}} \\
 \left( -\omega^2 - \frac{iB_{nm}\omega}{M_{nm} + A_{nm}} + \omega_n^2 \right) \zeta_n &= \frac{F_{FK,n}}{M_{nm} + A_{nm}} \\
 \Rightarrow \zeta_n &= \frac{F_{FK,n}}{M_{nm} + A_{nm}} \cdot \left( -\omega^2 - \frac{iB_{nm}\omega}{M_{nm} + A_{nm}} + \omega_n^2 \right)^{-1} \tag{E.28}
 \end{aligned}$$

The modal coordinates are determined for the first four mode shapes in Figure E.9. In the results the modal coordinates and other coefficients of Equations F.28 are defined.

The result of the modal coordinates originates from the normal mode method. This method is developed for systems without damping, where a little amount of damping can be added as shown in Equation F.27. For a larger amount of damping or a non-uniform distribution damping, the normal mode method is questionable to use for a hydro-elastic response of a system [35].

## F.2. Pure bulging

This section does concern the pure bulging mode, which means that the cross-sectional area along the beam is deformed. The total deformation of the beam is assumed to be a linear combination of the pure bending modes and the pure bulging modes. This section starts with identifying the 'dry' bulging modes, where in the following sections the 'wet' bulging modes are provided representing the hydro-elasticity in this modal analysis.

### Dry bulging mode

The differential equation resulting from the simplified continuity and momentum equation without external loads, is given by [8] without the influence of the longitudinal stress terms:

$$\frac{\partial^2 R}{\partial t^2} - \frac{1}{\rho D} \frac{\partial^2 R}{\partial x^2} = p(x, t) \quad (\text{E.29})$$

Where  $D$  is the distensibility of the tube and  $\rho$  is the density of the surrounding fluid. As mentioned in the previous section F.1, the solution of the differential equation will be composed of an homogeneous and particular solution. As first, the homogeneous solution will be obtained to find the dry eigenfrequencies and dry mode shapes. This will be found by the following equation:

$$\frac{\partial^2 R}{\partial t^2} - \frac{1}{\rho D} \frac{\partial^2 R}{\partial x^2} = 0 \quad (\text{E.30})$$

Since the solutions of this equation will be of the form  $R(x, t) = X(x)e^{-i\omega t}$ , Equation E.30 results in:

$$\begin{aligned} -\omega^2 X(x) - \frac{1}{\rho D} \frac{\partial^2 X(x)}{\partial x^2} &= 0 \\ c^2 X(x) + \frac{\partial^2 X(x)}{\partial x^2} &= 0 \end{aligned} \quad (\text{E.31})$$

where  $c^2 = \omega^2 \cdot \rho D$ . With a function like  $X(x) = \tilde{X}e^{nx}$  for the time-dependent function, this equation becomes:

$$\begin{aligned} (c^2 + n^2) \cdot \tilde{X}e^{nx} &= 0 \\ n_1 = ic \quad n_2 = -ic \end{aligned} \quad (\text{E.32})$$

This will result in a solution for  $X(x)$  of the general form:

$$X(x) = C_1 \cdot \sinh cx + C_2 \cdot \cosh cx \quad (\text{E.33})$$

Two boundary conditions are applied to the bulging structure where the beam is fixed at both ends of the tube, so the radius is fixed at both ends. This results in the boundary conditions given for the bow and stern:

$$\begin{aligned} Y(x=0) = C_2 = 0 &\rightarrow C_2 = 0 \\ Y(X=L) = C_1 \cdot \sinh cL = 0 &\rightarrow cL = i \cdot n\pi \end{aligned} \quad (\text{E.34})$$

The first 4 eigenmodes are found to be the solution of the second equation of Equation E.34:

$$\begin{aligned} c_1 \cdot L = 0 &\quad (\text{represents the rigid body mode}) \\ c_2 \cdot L \approx 3.14i &\rightarrow \omega_2 = \sqrt{\frac{(c_2 \cdot L)^2}{\rho D \cdot L^2}} = \sqrt{\frac{-9.87}{\rho D \cdot L^2}} \\ c_3 \cdot L \approx 6.28i &\rightarrow \omega_3 = \sqrt{\frac{(c_3 \cdot L)^2}{\rho D \cdot L^2}} \\ c_4 \cdot L \approx 9.42i &\rightarrow \omega_4 = \sqrt{\frac{(c_4 \cdot L)^2}{\rho D \cdot L^2}} \\ c_5 \cdot L \approx 12.57i &\rightarrow \omega_5 = \sqrt{\frac{(c_5 \cdot L)^2}{\rho D \cdot L^2}} \end{aligned} \quad (\text{E.35})$$

Since these solutions are not physical, the assumptions made in the beginning of this section should be revised.

### Dry bulging mode including longitudinal tension

Babarit defined a wave equation for a system without damping (of tube's material and viscous damping of inner fluid) and with an outer fluid being at rest. This wave equation for the 'dry' bulging mode depends on additional variable  $\chi$ , where the wave equation without external force is given as: [8]:

$$\frac{\partial^2 \chi}{\partial t^2} - \frac{1}{\rho D} \frac{\partial^2 \chi}{\partial x^2} + \frac{1}{\rho D} \frac{T_s D}{\pi} \frac{\partial^4 \chi}{\partial x^4} = 0 \quad (\text{E36})$$

where  $T_s$  is the static longitudinal tension inside the tube due to the static pressure inside the tube and the mooring pretension. The value of this tension is given as [8]  $T_s = F_{a,s} + p_{i,ss} S_s$ , where  $F_{a,s}$  is the prescribed mooring pretension,  $p_{i,s}$  is the static pressure inside the tube and  $S_s$  is the static cross-sectional area of the tube.

The solutions for  $\chi(x, t)$ <sup>4</sup> should be of the form [8]:

$$\chi(x, t) = \sum_{n=1}^{\infty} X_n(x) c_n(t) \quad (\text{E37})$$

where the time-dependent part  $c_n$  is of the form  $c_n = \xi_n \cdot e^{-i\omega t}$ . The substitution of Equation E37 into Equation E35 will result in:

$$-\omega^2 + \frac{1}{\rho D} \gamma^2 + \frac{T_s}{\rho \pi} \gamma^4 = 0 \quad (\text{E38})$$

Solution of this equation results in four components in our general solutions of the wave equation [8]:

$$\begin{aligned} \gamma_1^2 &= \frac{2\pi}{DT_s} \left( \sqrt{1 + \frac{T_s \rho D^2 \omega^2}{\pi}} - 1 \right) \\ \gamma_2^2 &= -\frac{2\pi}{DT_s} \left( \sqrt{1 + \frac{T_s \rho D^2 \omega^2}{\pi}} + 1 \right) \end{aligned}$$

from which

$$\gamma_1 = \pm k, \quad \gamma_2 = \pm iK \quad (\text{E39})$$

$$X(x) = A_1 e^{ikx} + A_2 e^{-ikx} + B_1 e^{Kx} + B_2 e^{-Kx} \quad (\text{E40})$$

The four constants  $A_1$ ,  $A_2$ ,  $B_1$  and  $B_2$  will be defined by the boundary conditions. To transform this solution of  $X(x)$  into trigonometric functions, we will replace the origin of the coordinate system into the middle of the cylinder. This means that the bow of the tube is placed at  $x = -L/2$  and the stern at  $x = +L/2$ . The first boundary condition implies the velocity of the inner fluid velocity is zero, which is due to the closed ends of the tube and the fixed position of the tube in the waves [8]. This boundary condition results in:

$$X(x = -L/2) = A_1 e^{-\frac{ikL}{2}} + A_2 e^{\frac{ikL}{2}} + B_1 e^{-\frac{KL}{2}} + B_2 e^{\frac{KL}{2}} = 0 \quad (\text{E41})$$

$$X(x = +L/2) = A_1 e^{\frac{ikL}{2}} + A_2 e^{-\frac{ikL}{2}} + B_1 e^{\frac{KL}{2}} + B_2 e^{-\frac{KL}{2}} = 0 \quad (\text{E42})$$

Two manipulations (addition and subtraction of Equations E41 and E42) gives us two trigonometric functions

<sup>4</sup>The variable  $\chi(x, t)$  is a variable representing the generalised fluid velocity inside the tube, where generalised means that the velocity is constant over the cross-section. The definition of  $\chi$  is not mentioned in the work of Babarit [8], but the boundary conditions show an analogy with the generalised fluid velocity  $U$ .

[8]:

$$\begin{aligned} X(x = -\frac{L}{2}) + X(x = +\frac{L}{2}) &= A_1 \left( e^{-\frac{ikL}{2}} + e^{\frac{+ikL}{2}} \right) + A_2 \left( e^{-\frac{ikL}{2}} + e^{\frac{+ikL}{2}} \right) + B_1 \left( e^{-\frac{KL}{2}} + e^{\frac{+KL}{2}} \right) + B_2 \left( e^{-\frac{KL}{2}} + e^{\frac{+KL}{2}} \right) \\ &= (A_2 + A_1) \cdot \left( e^{-\frac{ikL}{2}} + e^{\frac{+ikL}{2}} \right) + (B_2 + B_1) \cdot \left( e^{-\frac{KL}{2}} + e^{\frac{+KL}{2}} \right) = 0 \\ &(A_2 + A_1) \cos \frac{kL}{2} + (B_2 + B_1) \cosh \frac{kL}{2} = 0 \end{aligned} \quad (F43)$$

$$\begin{aligned} X(x = -\frac{L}{2}) - X(x = +\frac{L}{2}) &= A_1 \left( e^{-\frac{ikL}{2}} - e^{\frac{+ikL}{2}} \right) + A_2 \left( e^{-\frac{ikL}{2}} - e^{\frac{+ikL}{2}} \right) + B_1 \left( e^{-\frac{KL}{2}} - e^{\frac{+KL}{2}} \right) + B_2 \left( e^{-\frac{KL}{2}} - e^{\frac{+KL}{2}} \right) \\ &= (A_2 - A_1) \cdot \left( e^{-\frac{ikL}{2}} + e^{\frac{+ikL}{2}} \right) + (B_2 B_1) \cdot \left( e^{-\frac{KL}{2}} + e^{\frac{+KL}{2}} \right) = 0 \\ &i(A_2 - A_1) \sin \frac{kL}{2} + (B_2 - B_1) \sinh \frac{kL}{2} = 0 \end{aligned} \quad (F44)$$

Since the tube cannot deform at both ends of the tube, the additional boundary conditions at the bow and stern are [8]:

$$\frac{\partial}{\partial x} X \left( x = -\frac{L}{2} \right) = ikA_1 e^{-\frac{ikL}{2}} - ikA_2 e^{\frac{ikL}{2}} + KB_1 e^{-\frac{KL}{2}} - KB_2 e^{\frac{KL}{2}} = 0 \quad (F45)$$

$$\frac{\partial}{\partial x} X \left( x = +\frac{L}{2} \right) = ikA_1 e^{\frac{ikL}{2}} - ikA_2 e^{-\frac{ikL}{2}} + KB_1 e^{\frac{KL}{2}} - KB_2 e^{-\frac{KL}{2}} = 0 \quad (F46)$$

The same two manipulations result in two additions equations including some trigonometric functions to solve  $X(x)$  with respect to the given boundary conditions [8].

$$\begin{aligned} \frac{\partial}{\partial x} X \left( x = \frac{L}{2} \right) + \frac{\partial}{\partial x} X \left( x = +\frac{L}{2} \right) &= ikA_1 \left( e^{-\frac{ikL}{2}} + e^{\frac{+ikL}{2}} \right) - ikA_2 \left( e^{-\frac{ikL}{2}} + e^{\frac{+ikL}{2}} \right) + KB_1 \left( e^{-\frac{KL}{2}} + e^{\frac{+KL}{2}} \right) - KB_2 \left( e^{-\frac{KL}{2}} + e^{\frac{+KL}{2}} \right) \\ &= ik(A_2 - A_1) \cdot \left( e^{-\frac{ikL}{2}} + e^{\frac{+ikL}{2}} \right) + K(B_2 - B_1) \cdot \left( e^{-\frac{KL}{2}} + e^{\frac{+KL}{2}} \right) = 0 \\ &ik(A_2 - A_1) \cos \frac{kL}{2} + K(B_2 - B_1) \cosh \frac{kL}{2} = 0 \end{aligned} \quad (F47)$$

$$\begin{aligned} \frac{\partial}{\partial x} X \left( x = \frac{L}{2} \right) - \frac{\partial}{\partial x} X \left( x = +\frac{L}{2} \right) &= ikA_1 \left( e^{-\frac{ikL}{2}} - e^{\frac{+ikL}{2}} \right) - ikA_2 \left( e^{-\frac{ikL}{2}} - e^{\frac{+ikL}{2}} \right) + KB_1 \left( e^{-\frac{KL}{2}} - e^{\frac{+KL}{2}} \right) - KB_2 \left( e^{-\frac{KL}{2}} - e^{\frac{+KL}{2}} \right) \\ &= ik(A_2 + A_1) \cdot \left( e^{-\frac{ikL}{2}} - e^{\frac{+ikL}{2}} \right) + K(B_2 + B_1) \cdot \left( e^{-\frac{KL}{2}} - e^{\frac{+KL}{2}} \right) = 0 \\ &-k(A_2 - A_1) \sin \frac{kL}{2} + K(B_2 - B_1) \sinh \frac{kL}{2} = 0 \end{aligned} \quad (F48)$$

And since we have four undetermined coefficients, the function could be solved by the four obtained Equations (F43, F44, F47 and F48). These equations are translated into two matrix Equations [8]:

$$\begin{bmatrix} \cos \frac{kL}{2} & \cosh \frac{KL}{2} \\ -k \sin \frac{kL}{2} & K \sinh \frac{KL}{2} \end{bmatrix} \begin{bmatrix} A_2 + A_1 \\ B_2 + B_1 \end{bmatrix} = \begin{bmatrix} 0 \\ 0 \end{bmatrix} \quad (F49)$$

$$\begin{bmatrix} i \sin \frac{kL}{2} & \sinh \frac{KL}{2} \\ ik \cos \frac{kL}{2} & K \cosh \frac{KL}{2} \end{bmatrix} \begin{bmatrix} A_2 - A_1 \\ B_2 - B_1 \end{bmatrix} = \begin{bmatrix} 0 \\ 0 \end{bmatrix} \quad (F50)$$

The solution of  $X_n(x)$  is found for a combination of values  $k_n$ ,  $K_n$  and  $\omega_n$  obtained from the following set of equations [8]:

$$(S1) \begin{cases} k_n \cdot \tanh \frac{K_n L}{2} - K_n \cdot \tan \frac{k_n L}{2} = 0 \\ A_1 = -A_2 \\ B_1 = -B_2 \\ k_n^2 = \frac{2\pi}{DT_S} \left( \sqrt{1 + \frac{T_S \rho D^2 \omega_n^2}{\pi}} - 1 \right) \\ K_n^2 = \frac{2\pi}{DT_S} \left( \sqrt{1 + \frac{T_S \rho D^2 \omega_n^2}{\pi}} + 1 \right) \\ \omega_n^2 = \frac{k_n^4 T_S}{4\pi \rho} + \frac{k_n^2}{D \rho} = \frac{K_n^4 T_S}{4\pi \rho} + \frac{K_n^2}{D \rho} \end{cases} \quad (F51)$$

where the first formula is found by the determinant of the rectangular matrix of Equation F50. A second same characteristic equation is found by the determinant of the rectangular matrix of Equation F49 and the

associated set of Equations:

$$(S2) \begin{cases} K_n \cdot \tanh \frac{K_n L}{2} + k_n \cdot \tan \frac{k_n L}{2} = 0 \\ A_1 = A_2 \\ B_1 = B_2 \\ k_n^2 = \frac{2\pi}{DT_S} \left( \sqrt{1 + \frac{T_S \rho D^2 \omega_n^2}{\pi}} - 1 \right) \\ K_n^2 = \frac{2\pi}{DT_S} \left( \sqrt{1 + \frac{T_S \rho D^2 \omega_n^2}{\pi}} + 1 \right) \\ \omega_n^2 = \frac{k_n^4 T_S}{4\pi \rho} + \frac{k_n^2}{D\rho} = \frac{K_n^4 T_S}{4\pi \rho} + \frac{K_n^2}{D\rho} \end{cases} \quad (E52)$$

As a solution of these systems of equations, two solutions for  $\chi_n$  are found [8]:

$$X_n^{(1)}(x) = \tanh \left( \frac{K_n^{(1)} L}{2} \right) \frac{\sin \left( k_n^{(1)} x \right)}{\cos \left( k_n^{(1)} L/2 \right)} - \tan \left( \frac{k_n^{(1)} L}{2} \right) \frac{\sinh \left( K_n^{(1)} x \right)}{\cosh \left( K_n^{(1)} L/2 \right)} \quad (E53)$$

$$X_n^{(2)}(x) = K_n^{(2)} \tanh \left( \frac{K_n^{(2)} L}{2} \right) \frac{\cos \left( k_n^{(2)} x \right)}{\cos \left( k_n^{(2)} L/2 \right)} + k_n^{(2)} \tan \left( \frac{k_n^{(2)} L}{2} \right) \frac{\cosh \left( K_n^{(2)} x \right)}{\cosh \left( K_n^{(2)} L/2 \right)} \quad (E54)$$

where the boundary conditions for  $x = +L/2$  are inserted to find the ratio between the values of  $A_1$  and  $B_1$ . For set 1, the velocity boundary condition is used to find this ratio. In Equation E54 the values  $K_n^{(2)}$  and  $k_n^{(2)}$  return in the mode shape, as a results of the ratio of  $A_1$  and  $B_1$  defined by set 2. The first six mode shapes in Figure E3 are the results of the Equations E53 and E54. Modes 1, 3, 4 and 6 are a solution of E54 with the values of  $K_n^{(2)}$  and  $k_n^{(2)}$ . The resulting modes (2 and 5) are described by Equation E53,  $K_n^{(1)}$  and  $k_n^{(1)}$ . The first six eigenfrequencies are observed, since the corresponding natural frequencies are in the observed range of frequencies;  $0.2 < \omega \leq 8.0$ .

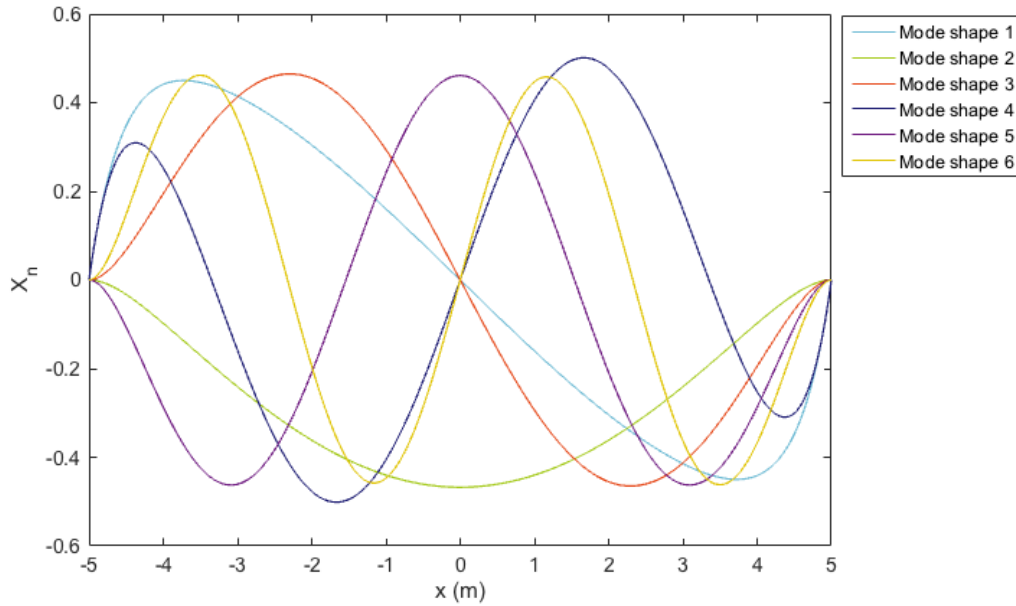


Figure E3: Mode shapes of the first six eigenmodes.

The first six mode shapes defined by Babarit's expressions are plotted in Figure E3. These mode shapes should be the solution of the Equations E41, E42, E45 and E46, representing the boundary conditions of this bulging system. These boundary conditions, could be tested with respect to the mode shapes of Figure E3. The first two boundary conditions imply that both ends of the tube can not deform, so this means  $X(x = \pm \frac{L}{2}) = 0$ . The last two boundary condition imply that the internal fluid velocity is equal to zero, which is indicated by

$\frac{\partial X}{\partial x}(x = \pm \frac{L}{2}) = 0$  and is observed from the mode shapes of type 1 and 2 by the Equations E53 and E54:

$$\frac{\partial X_n^{(1)}(x)}{\partial x} = k_n^{(1)} \tanh\left(\frac{K_n^{(1)} L}{2}\right) \frac{\cos(k_n^{(1)} x)}{\cos(k_n^{(1)} L/2)} - K_n^{(1)} \tan\left(\frac{k_n^{(1)} L}{2}\right) \frac{\cosh(K_n^{(1)} x)}{\cosh(K_n^{(1)} L/2)} \quad (\text{E.55})$$

$$\frac{\partial X_n^{(2)}(x)}{\partial x} = -k_n^{(2)} \cdot K_n^{(2)} \tanh\left(\frac{K_n^{(2)} L}{2}\right) \frac{\cos(k_n^{(2)} x)}{\cos(k_n^{(2)} L/2)} + K_n^{(2)} \cdot k_n^{(2)} \tan\left(\frac{k_n^{(2)} L}{2}\right) \frac{\cosh(K_n^{(2)} x)}{\cosh(K_n^{(2)} L/2)} \quad (\text{E.56})$$

These derivatives are plotted against the mode shapes, which is shown in Figure E4. The blue line is representing the mode shape and the green line the derivative of the mode shape with respect to  $x$ .

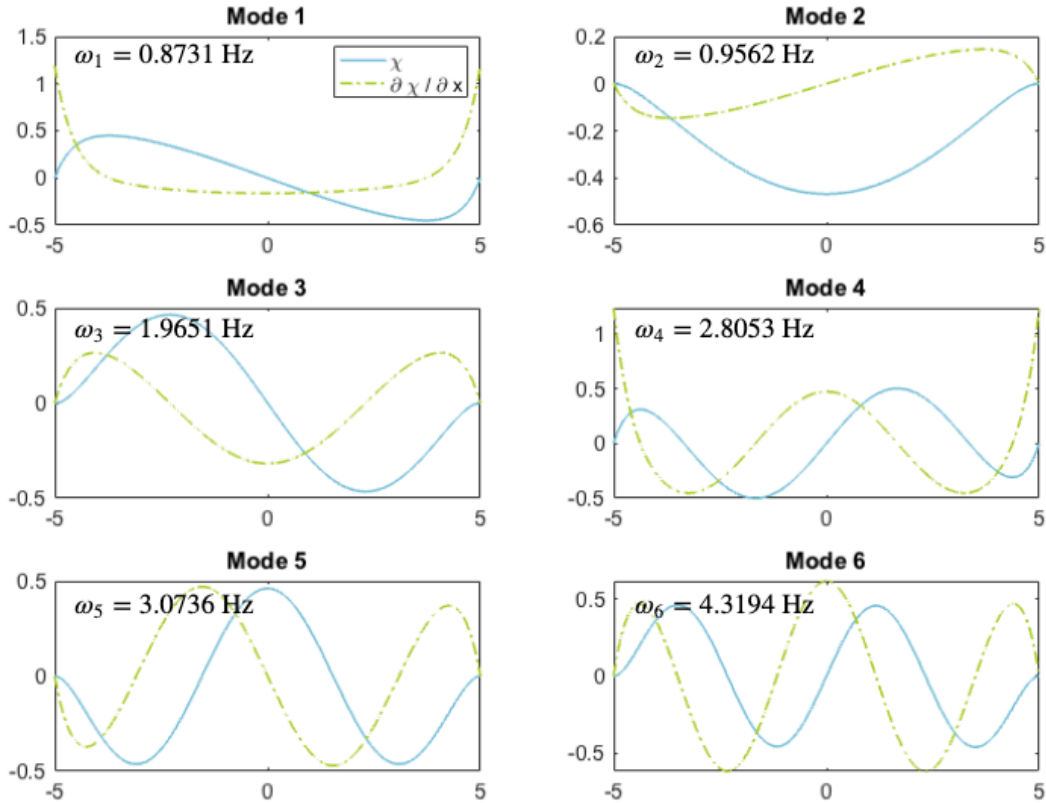


Figure E4: Dry mode shapes and derivatives of the bulging mode shapes.

Surprisingly, the first and fourth mode shapes do not match the boundary conditions, but these are the same mode shapes as defined by Babarit [8]. These mode shapes are observed for 'numerical eigenfrequencies', which are solution of the first equations of the Sets of Equations E51 and E52. These solutions are due to numerics, where asymptotes values are not skipped, and frequencies are found that is not physical correct. The characteristic equations of both sets of equations include a tan and tanh function, which results in one or more asymptotes where the values at lower limit go to minus infinity and at the upper limit to plus infinity. In a numerical model these two points will be connected by a line element, which crossed the  $x$ -axis (representing the frequency  $\omega$ ) and is therefore an additional zero-crossing value. The other zero-crossing values define the values of the eigenfrequencies, but these numerical eigenfrequencies should be removed to observe only physically valid eigenfrequencies. For the bulging modes of the observed tube with tube dimensions of Table E2 the Characteristic equations are given in Figure E5. The values of the 'numerical eigenfrequencies' are found in both types of mode shapes, and will be both removed to end with only valid eigenfrequencies. One important mark has to be made about the resulting 'dry' mode shapes of the bulging cylinder. Since the modes are either asymmetric (Mode 1, 3 and 5) or symmetric (Mode 2, 4 and 6), the mode is representing the section averaged flow velocity [8]. The deformation of the cross-sectional area is related to the derivative of

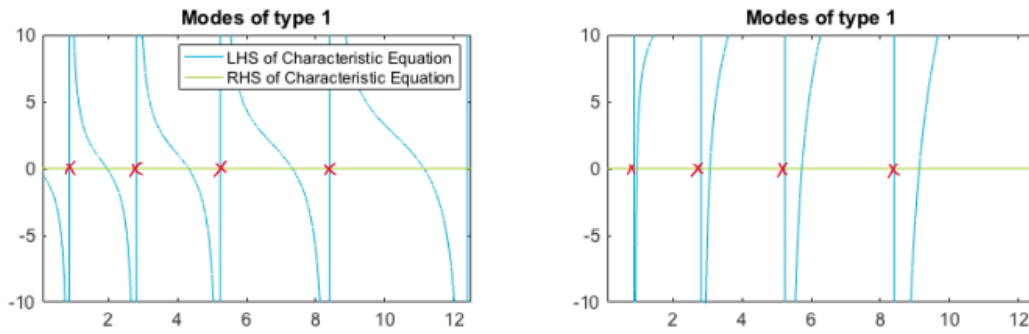


Figure E5: Characteristic equations of set 1 (Equation E51) and set 2 (Equation E52) including the numerical eigenfrequencies (given by red crosses).

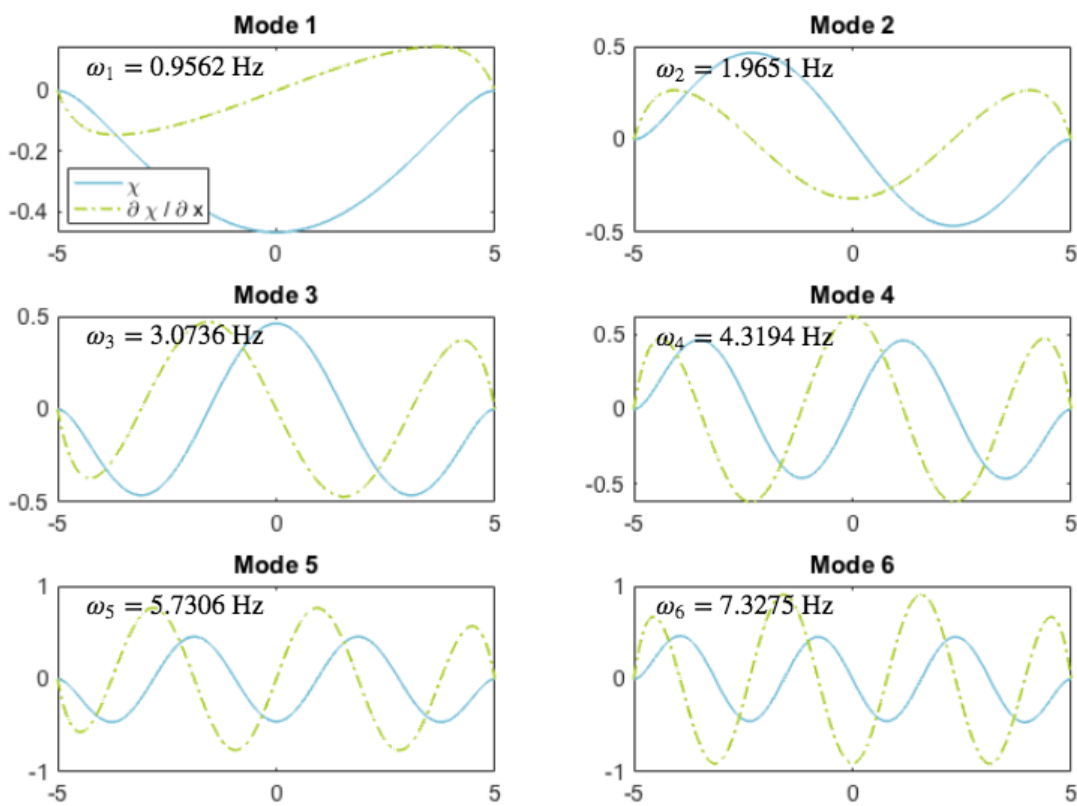


Figure E6: Dry mode shapes and derivatives of the mode shapes without the 'numerical eigenfrequencies' of bulging.

the mode shape with respect to  $x$ , denoted by  $\partial\chi/\partial x$  (and also  $\partial X/\partial x$ ), and provides conservation of volume:

$$S - S_S = -S_S \frac{\partial X}{\partial x} \tag{E57}$$

Where  $S_S$  is the cross-sectional area of the pre-tensioned tube by the inner fluid. The conservation of mass could be interpreted as a conservation of volume, by integration of the cross-sectional area along the tube's length. This check could be done by taking the area below the curves representing  $\partial X/\partial x$  in Figure E6. The integral under this curve is representing the change in total area, which should be equal to zero. The values found by a numerical integration are given in Table E3, where the values of mode 2, 4 and 5 are significant.

Name	Symbol	Unit	Mode	$\int_{-L/2}^{+L/2} \frac{\partial \chi}{\partial x} dx$
Length	$L$	10 m		
Radius	$R_s$	0.274 m		
Wall thickness	$h_s$	0.01 m		
Submersion depth	$d$	-1.25 m	1	2.2195e-15
Tube mass	$M_{tube}$	91.7 kg	2	-7.2979e-04
Mooring pretension	$F_{as}$	443.4 N	3	-1.8987e-15
Static pressure	$p_s$	77.7 kPa	4	-0.0019
Distensibility	$D$	$1.29 \cdot 10^3$ Pa <sup>-1</sup>	5	-3.9048e-15
Young's modulus	$E$	$0.0020 \cdot 10^9$ Pa	6	-0.0036

Table F2: Geometry and material properties for numerical calculations on elastic-hydrodynamic motions [8].

Table F3: Check for conservation of mass of first six mode shapes for 100 panels along the tube's length.

The results of continuity test will decrease for an increase of panels in x-direction, where we could state that the deviations of the results of the conservation of volume-test are due to numerical integration inaccuracies.

### Hydro-elastic bulging mode

The response of the bulge WEC should be analysed with the interaction of the surrounding fluid in terms of radiated and incident pressures. This hydro-elasticity is evaluated in a similar way to the hydro-elastic analysis of the bulge modes, but some differences will be described in the following paragraphs. The differential equation of the problem including the surrounding fluid is given as [8]:

$$\frac{\partial^2 \chi}{\partial t^2} - \frac{1}{\rho D} \frac{\partial^2 \chi}{\partial x^2} + \frac{1}{\rho D} \frac{T_s D}{\pi} \frac{\partial^4 \chi}{\partial x^4} = -\frac{1}{\rho} \frac{\partial \bar{p}_e}{\partial x} \quad (\text{E58})$$

which is the same as Equation E.12 without the terms for damping of the tubes material and the inner fluid, which will be neglected in this modal analysis. The modal superposition is used, where  $\chi(x, t) = \sum_{n=1}^{N_{mode}} X_n(x) \cdot c_n(t)$ . Since the contour averaged pressure is the sum of the incident wave pressure ( $\bar{p}_W$ ) and the radiation pressure  $\bar{p}_R^{(4)}$ , the contour averaged pressure is given by [8]:

$$\bar{p}_e(x, \omega) = \bar{p}_W(x) \cdot e^{-i\omega t} + \sum_{n=1}^N (-A_{nm}(\omega) \dot{c}_n - B_{nm}(\omega)) \dot{c}_n \quad (\text{E59})$$

Implementation of Equation E59 and the modal superposition of  $\chi(x, t)$  into the differential equation of E58, results in:

$$\sum_{n=1}^{N_{mode}} \ddot{c}_n X_n - \frac{1}{\rho D} \sum_{n=1}^{\infty} c_n \frac{\partial^2 X_n}{\partial x^2} + \frac{1}{\rho D} \frac{T_s D}{\pi} \sum_{n=1}^{\infty} c_n \frac{\partial^4 X_n}{\partial x^4} = -\frac{1}{\rho} \frac{\partial \bar{p}_W}{\partial x} \cdot e^{-i\omega t} + \sum_{n=1}^{N_{mode}} (-A_n(x, \omega) \dot{c}_n - B_n(x, \omega)) \dot{c}_n \quad (\text{E60})$$

A multiplication of this function with mode shape  $X_m$  and integration over the length of the beam will result in a more simplified system of equations, where the orthogonal properties of the modeshapes are the key point [8].

$$\begin{aligned} & \sum_{n=1}^{N_{mode}} \left( \ddot{c}_n \int_{-L/2}^{L/2} X_n X_m dx - \frac{1}{\rho D} c_n \int_{-L/2}^{L/2} \frac{\partial^2 X_n}{\partial x^2} X_m dx + \frac{1}{\rho D} \frac{1}{K_0^2} c_n \int_{-L/2}^{L/2} \frac{\partial^4 X_n}{\partial x^4} X_m dx \right) \\ & = -\frac{1}{\rho} \int_{-L/2}^{L/2} \frac{\partial \bar{p}_i}{\partial x} X_m dx - \frac{1}{\rho} \sum_{n=1}^{N_{mode}} \dot{c}_n \int_{-L/2}^{L/2} A_n(\omega) \frac{\partial X_m}{\partial x} dx - \frac{1}{\rho} \sum_{n=1}^{\infty} \dot{c}_n \int_{-L/2}^{L/2} B_n(\omega) \frac{\partial X_m}{\partial x} dx \end{aligned} \quad (\text{E61})$$

$$= \sum_{n=1}^{N_{mode}} (1 + A_{nm}^*) \ddot{c}_n + B_{nm}^* \dot{c}_n + K_{nm} c_n = F_{FK,m}^* \quad (\text{E62})$$

where the coefficients  $A_{nm}^*$ ,  $B_{nm}^*$ ,  $K_{nm}$  and  $F_{FK,m}^*$  are given as [8]:

$$\begin{aligned}
K_{nm} &= \frac{1}{\rho D} \left( \int_{-L/2}^{L/2} \frac{\partial^2 X_n}{\partial x^2} W_m dx + \frac{1}{K_0^2} \int_{-L/2}^{L/2} \frac{\partial^4 X_n}{\partial x^4} X_m dx \right) \\
A_{nm}^* &= \frac{1}{\rho} \int_{-L/2}^{L/2} A_n(\omega) \frac{\partial X_m}{\partial x} dx \\
B_{nm}^* &= \frac{1}{\rho} \int_{-L/2}^{L/2} B_n(\omega) \frac{\partial X_m}{\partial x} dx \\
F_{FK,m}^* &= \frac{1}{\rho} \cdot -i\rho g \zeta_I \cdot e^{-i\omega t} \int_{-L/2}^{L/2} e^{ivx} \cdot \frac{\partial X_m}{\partial x} dx \cdot \int_{C_0} e^{vz} n_n dC
\end{aligned} \tag{E63}$$

Where the coefficients are denoted by an \* are related to the change in cross-sectional area. Babarit defined the mathematical operator \* for a arbitrary function as [8]:

$$f^* = \frac{1}{\rho} \int_{-L/2}^{L/2} f(x) \frac{\partial X_m}{\partial x} dx - \Delta f(x) X_m|_{L/2} \tag{E64}$$

where the second term is in this case always zero, since the boundary conditions state that  $X(x = \pm L/2) = 0$ . Therefore these terms are neglected in Equation E59, E61 and E62.

### Homogeneous solution

The homogeneous solution of the hydro-elastic bulging mode is a reduced form of Equation E61, where the incident wave pressure and radiation damping are neglected. For mode shape  $n$  the homogeneous solution has to solve:

$$(1 + A_{nm}^*) \ddot{c}_n + K_{nm} c_n = 0 \tag{E65}$$

When we assume  $c_n = \xi_n \cdot e^{-i\omega t}$ , the following eigenvalue problem arises:

$$\left[ K_{nm} - (\omega_n^{wet})^2 \cdot (1 + A_{nm}^*) \right] \xi_n \cdot e^{-i\omega t} = 0 \tag{E66}$$

which looks the same as Equation E26, where we replace some values for the matrix coefficients;  $M_{nm} = 1$  and  $A_{nm} = A_{nm}^*$ . The iteration scheme is used with the different matrix coefficients, and as a result the 'wet' natural frequencies are found. For an iteration criteria of  $\varepsilon = 1 \cdot 10^{-12}$ , the 'dry' and 'wet' natural frequencies of the first 6 modes are assembled in Table E4.

Mode	'Dry' eigenfrequency	'Wet' eigenfrequency
$n$	$\omega_n^{dry}$ (Hz)	$\omega_n^{wet}$ (Hz)
1	0.9562	0.9252
2	1.9651	1.8276
3	3.0736	2.7521
4	4.3194	4.0294
5	5.7306	5.5933
6	7.3275	7.0468

Table E4: 'Dry' and 'wet' eigenfrequencies of the bulging modes of a bulge WEC with dimension given in Table E2.

Since the off-diagonal terms of the  $A_{nm}^*$ ,  $B_{nm}^*$  and  $K_{nm}$  matrices are equal to zero, in other words there is no coupling between the bulging modes, the mode shapes of the 'wet' bulging are exactly the same as the 'dry' bulging mode shapes (which are given in Figure E6).

### Particular solution

The particular solution of the mode shape can be determined by Equation E62 with the matrix coefficients from E63. We assume the modal coordinates as a function of  $c_n(t) = \xi_n \cdot e^{-i\omega t}$  (in stead of  $c_n(t) = \xi_n \cdot e^{-i(\omega t + \theta)}$ ),

so Equation E62 is rewritten into:

$$\begin{aligned}
-\omega^2(1 + A_{nm}^*)\xi_n \cdot e^{-i\omega t} - i\omega B_{nm}^*\xi_n \cdot e^{-i\omega t} + K_{nm}\xi_n \cdot e^{-i\omega t} &= F_{FK,m}(\omega)^* \cdot e^{-i\omega t} \\
-\omega^2\xi_n \cdot e^{-i\omega t} - i\frac{B_{nm}^*\omega}{1 + A_{nm}^*}\xi_n \cdot e^{-i\omega t} + \frac{K_{nm}}{1 + A_{nm}^*}\xi_n \cdot e^{-i\omega t} &= \frac{F_{FK,n}(\omega)^*}{1 + A_{nm}^*} \cdot e^{-i\omega t} \\
\left(-\omega^2 - i\frac{B_{nm}^*\omega}{1 + A_{nm}^*} + \omega_n^2\right)\xi_n &= \frac{F_{FK,m}(\omega)^*}{1 + A_{nm}^*} \\
\Rightarrow \xi_n &= \frac{F_{FK,m}(\omega)^*}{1 + A_{nm}^*} \cdot \left(-\omega^2 - i\frac{B_{nm}^*\omega}{1 + A_{nm}^*} + \omega_n^2\right)^{-1}
\end{aligned} \tag{E67}$$

The resulting modal coordinates for each mode are given in Figure E14. These modal coordinates are the real values of  $\xi_n$ <sup>5</sup>.

## E.3. Results

### Bending

The results for bending are partly given in the previous sections, for example the mode shapes that are shown in Figure E2. The radiation coefficients are defined for each mode shape, which is shown Figure E7. The red and purple dots represent the values of  $A_{nm}$  and  $B_{nm}$  as defined in the iterative process of Figure E1. The geometry characteristics that are used as input of the model are given in Table E2.

For every bending mode shape a generalised excitation force is defined for the incident wave by Equation E20. These excitation forces are presented in Figure E8. In these graphs a vertical line is added which indicates the wavelength of the mode shape. For example the first mode shape shows resemblance with the first half of a sine, where the wavelength of the total sine is approximate  $2 \cdot L$ . In the graph in the upper left of Figure E8 this wavelength is indicated.

As a result of the hydrodynamic coefficients  $A_{nm}$  and  $B_{nm}$  and excitation force  $F_{FK,n}$  the modal coordinates are defined for each mode shape and wave frequency. The modal coordinates  $\zeta_n$  are plotted in Figure E9. This graphs are representing the response amplitude operator (RAO) of every bending mode shape, since the amplitude of the incoming wave is equal to 1.

<sup>5</sup>The imaginary part of  $\xi_n$  is known as the phase difference of  $c_n = \xi_n e^{-i(\omega t + \theta)}$ . Since the  $\theta$  is not calculated in the calculation of  $\xi_n$ , the value of  $\xi_n$  is complex.

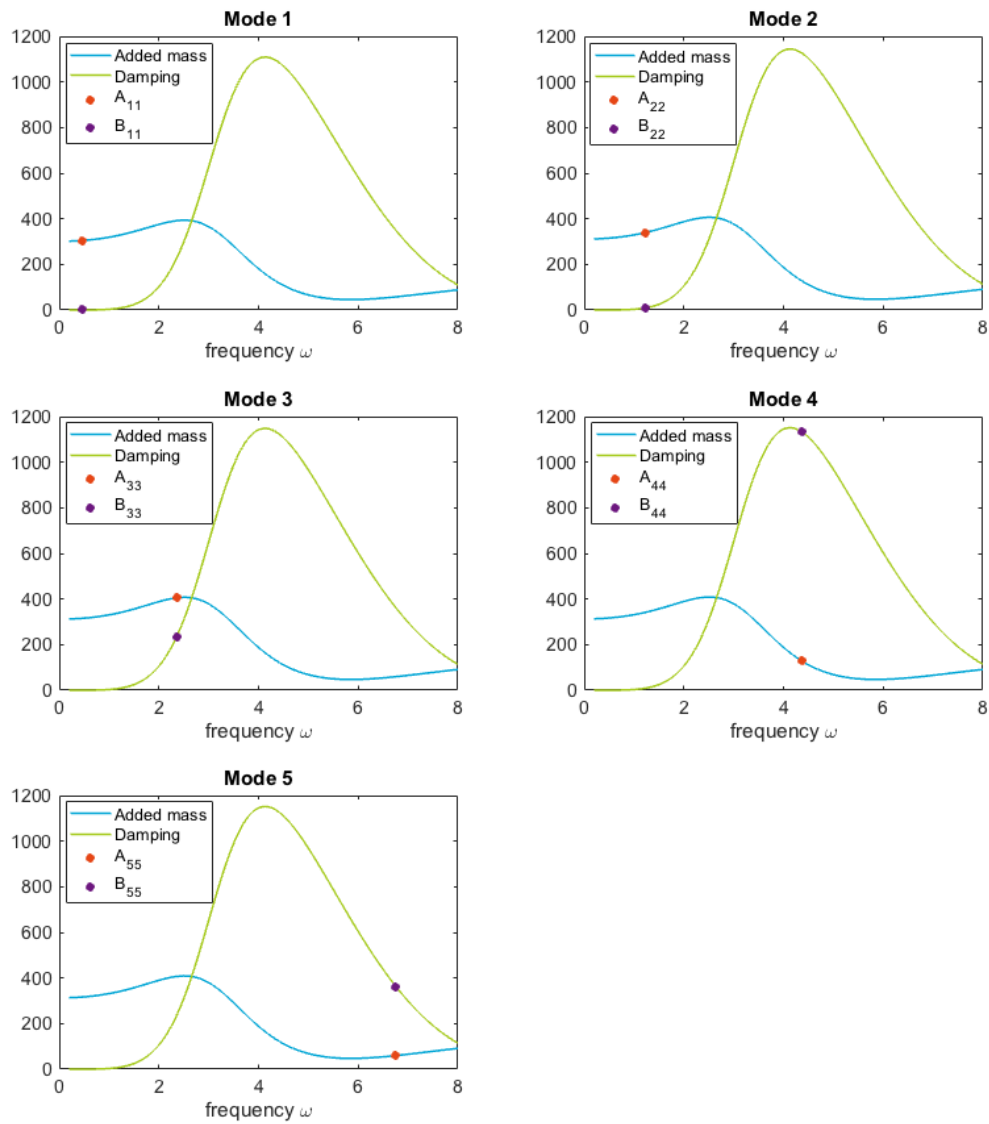


Figure E7: Hydrodynamic coefficients for the first 5 bending mode shapes.

As the last result, the deformation rate of the tube is plotted in Figure E10. The deformation rate  $\delta\lambda = \sum_{n=1}^{N_{mode}} \zeta_n \eta_n(x) \cdot e^{-i\omega t}$  gives the deflection of the tube for a fixed position along the tube due to a certain frequency.

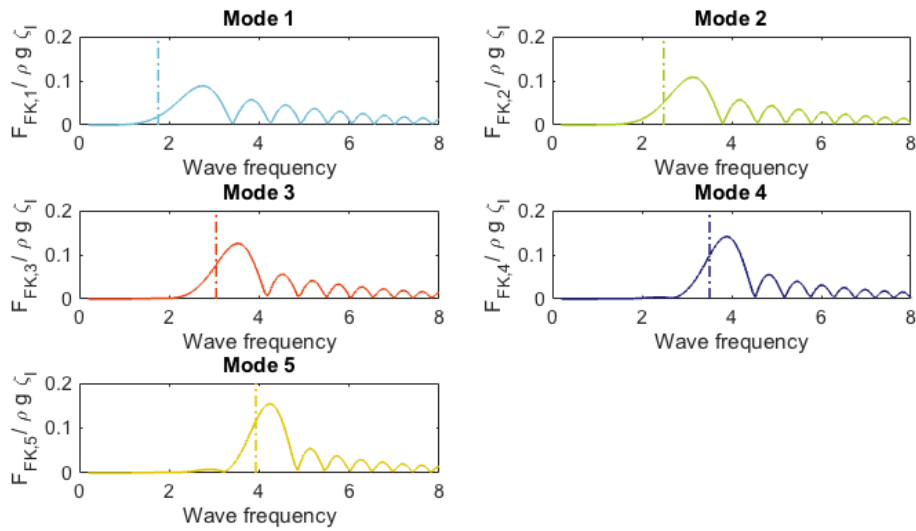


Figure E8: Excitation pressure for the first 5 bending mode shapes.

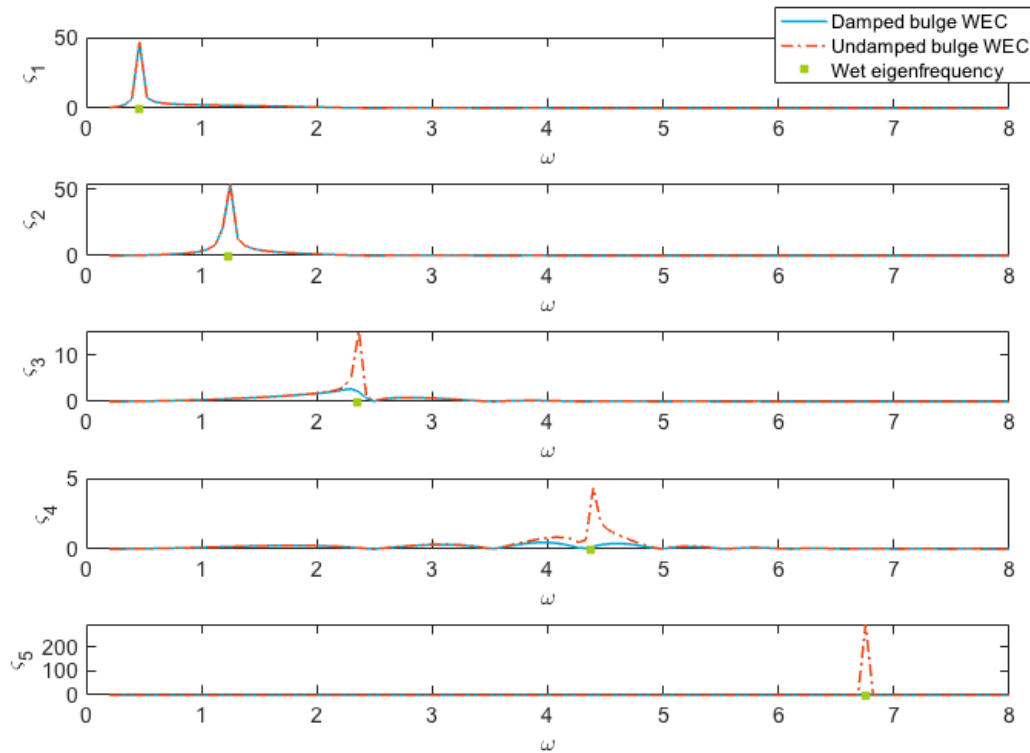


Figure E9: Modal coordinates for the first 5 bending mode shapes.

### Bulging

The results of the pure bulging case are given in this section. The first results, the bulging mode shapes, are already given in Figure F.6, where the boundary conditions are fulfilled. Since the frequency range is defined by incoming waves with a period between 1 and 5 seconds, the fifth and sixth modes are outside the observed frequency range. The first 4 bulging eigenmodes are shown in Figure F.11.

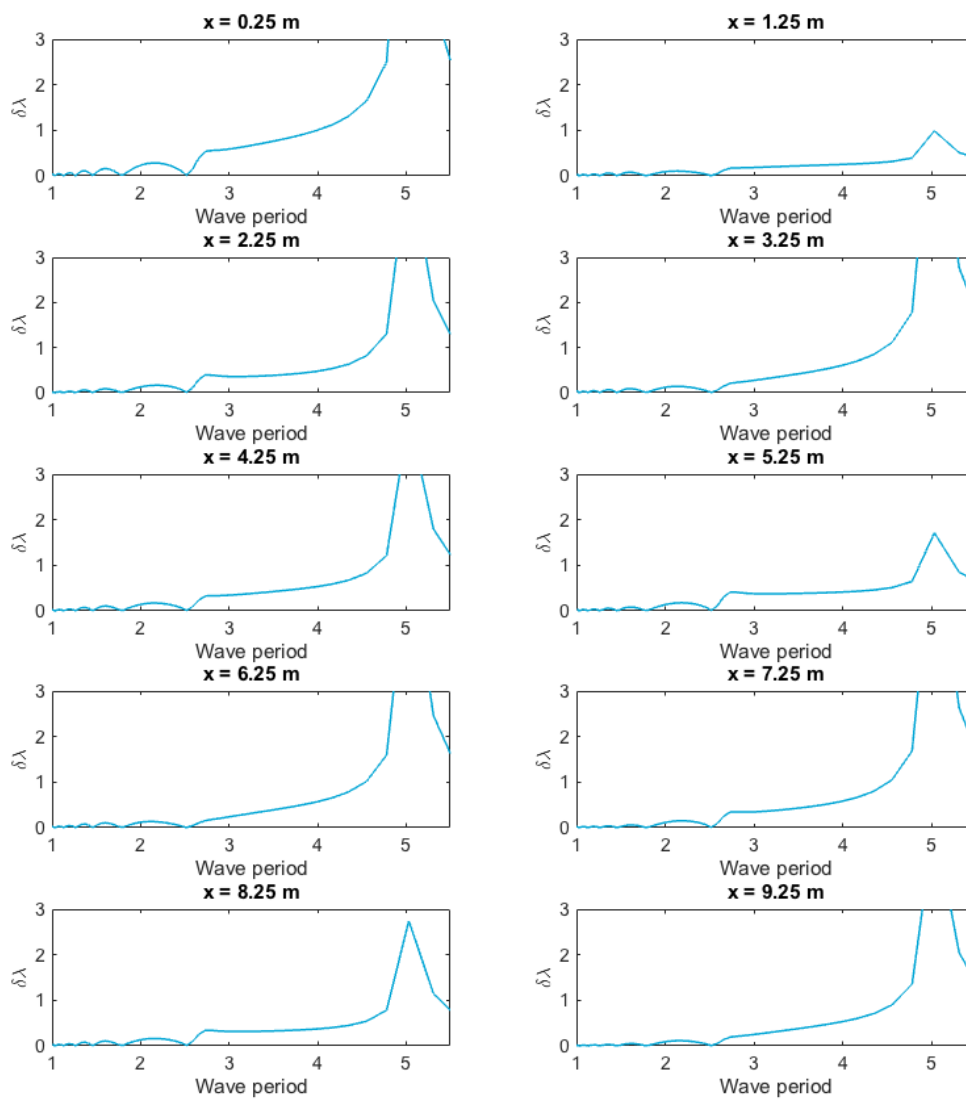


Figure E.10: Deformation of the tube at 10 positions along the tube.

For each mode shape the hydrodynamic coefficients  $A_{nm}$  and  $B_{nm}$  are plotted in Figure E.12. In these plots the values of the added mass and damping coefficients is increasing for an increasing eigenfrequency, which will be due to the influence of the particular mode shape. The values of  $A_{nm}$  and  $B_{nm}$  that are used in the iterative process are highlighted by the red and purple points in the graphs.

To solve the equation of motion, a generalised excitation force is calculated by Equation E.63. The values of the excitation force per mode shape is plotted in Figure E.13. In these plots, the vertical line is representing the wavelength of the trigonometric function corresponding to the mode shape. These values are close the excitation peak of every mode shape, where small deviations are caused by difference between a purely trigonometric function and the mode shape. In the higher frequency range, local maxima are found as well. These peaks are caused by every multiple of the modes wavelength.

As a result of Equation E.67 the modal coordinates for the first 4 bulging modes are plotted in Figure E.14. For the third and fourth mode, differences between the damped and undamped modal coordinates are significant around the eigenfrequencies. The values of the damping coefficients of the third and fourth mode

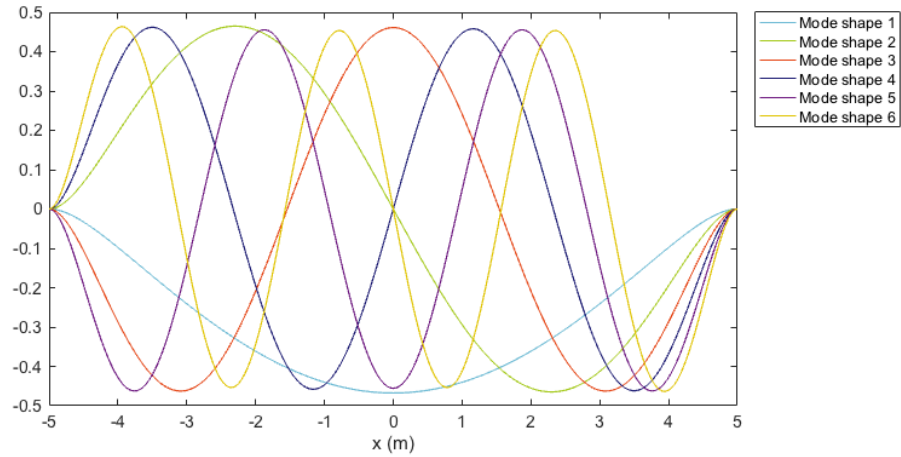


Figure E.11: First 6 mode shapes of the bulging tube.

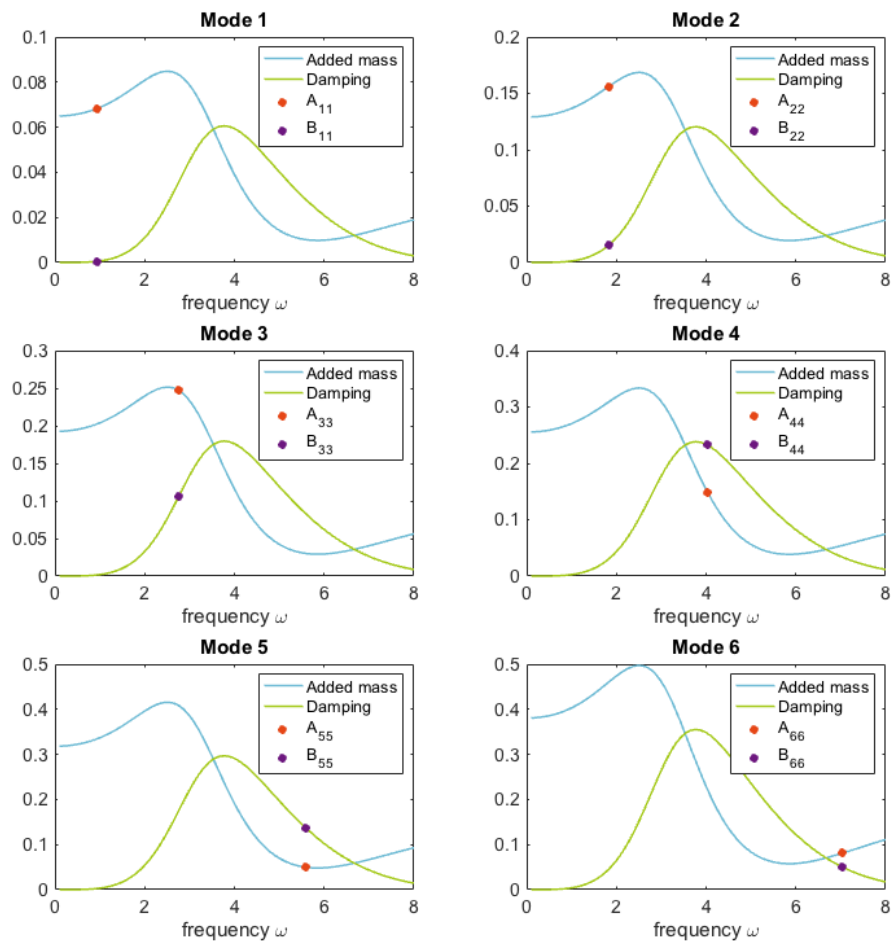


Figure E.12: Hydrodynamic coefficients for the first 6 bulging mode shapes.

are significantly higher than the same coefficients from the first two modes, as shown in Figure F.12.

The final results of the modal analysis is the deformation of the tube due to the first 4 bulging modes. This

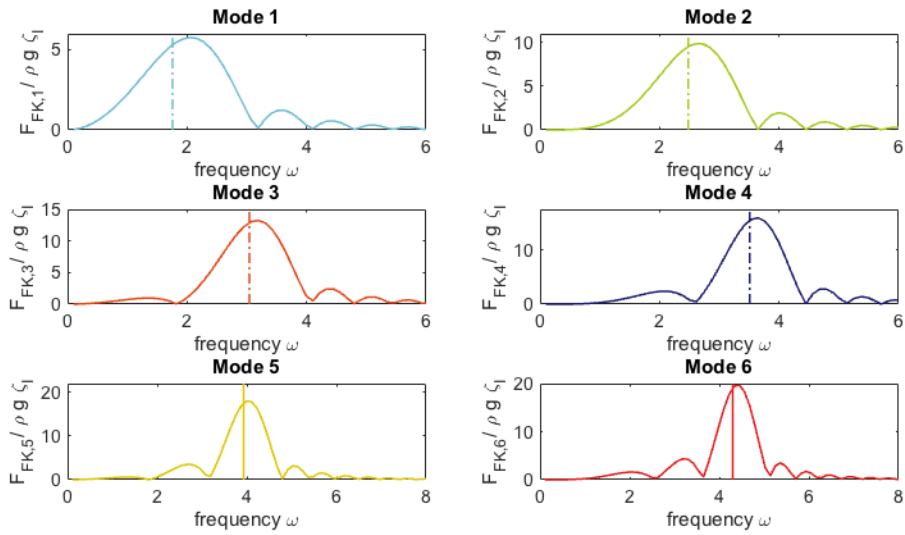


Figure E.13: Excitation pressure for the first 6 bulging mode shapes.

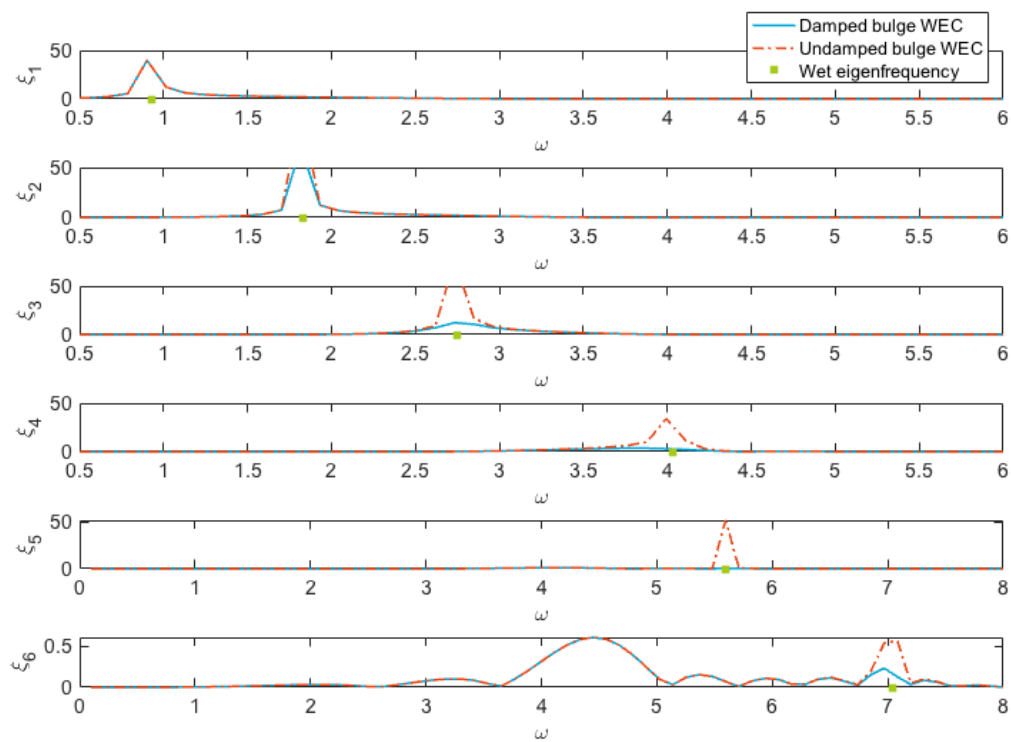


Figure E.14: Modal coordinates for the first 6 bulging mode shapes.

deformation is defined for bulging as  $\delta\lambda = \frac{S}{S_S} - 1$ , which is the change in radius of the tube. This deformation rate is shown in Figure E.15 for 10 positions along the tube. The red points are the experimental values used by Babarit [8] to validate their numerical model.

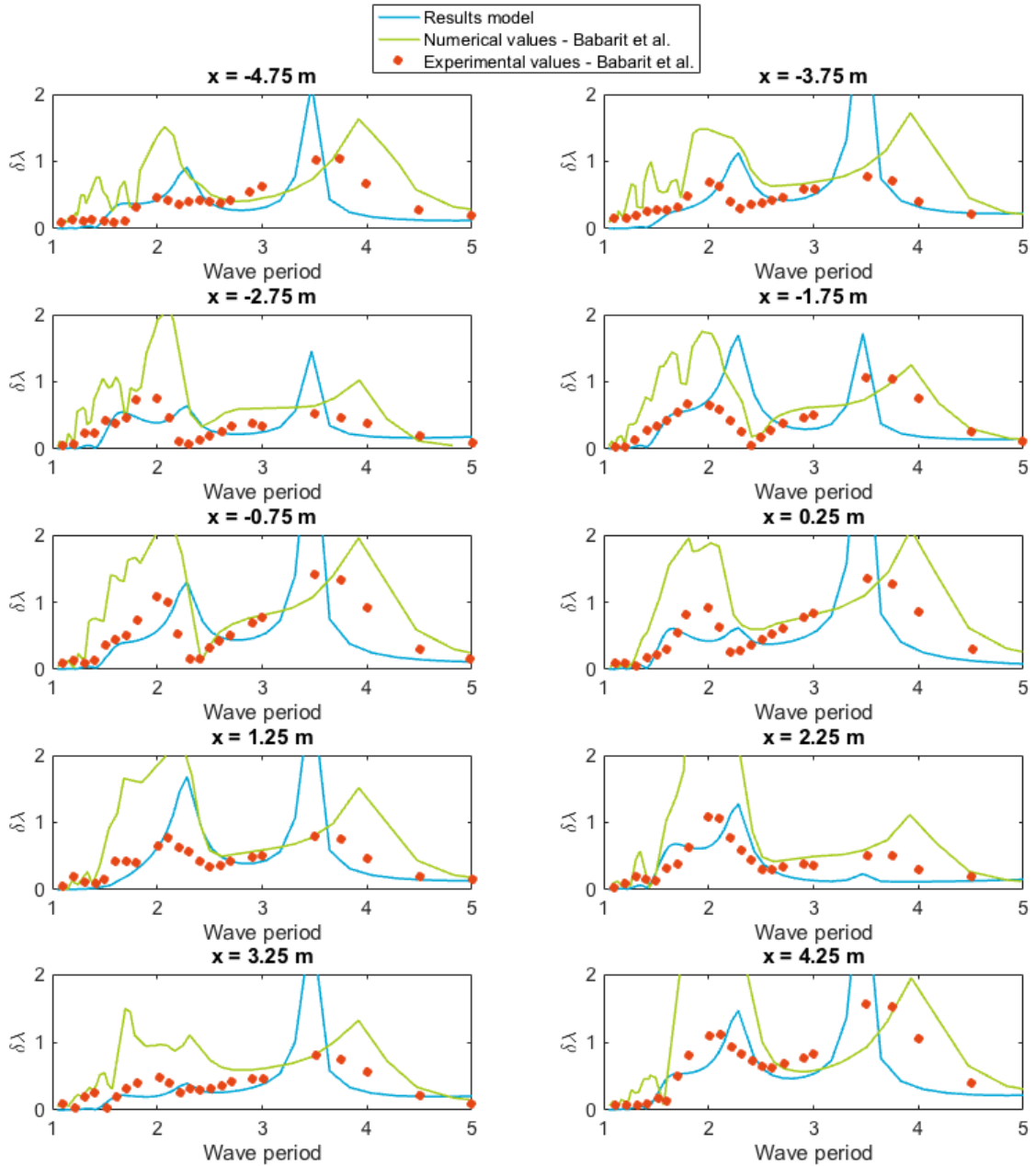


Figure F.15: Deformation of the tube at 10 positions along the tube for bulging. The blue line represents the FCFM results, the green are the numerical results of Babarit et al. and the red dots represent the experimental values found by Babarit et al. [8].

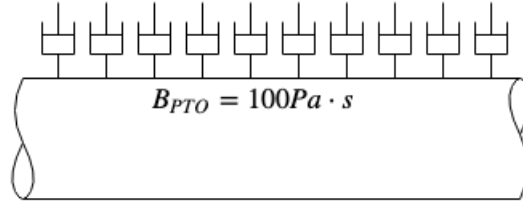
### WEC efficiency

As described in Appendix A, the performance of a WEC is defined by an efficiency  $\eta_{wec}$ . This efficiency is the ratio between the power absorbed by the WEC and the mean energy per meter crest width in the sea with wave amplitude  $\zeta_I$ . For bending and bulging different configurations of the power take-off (PTO) are observed. In Figure F.16 three configurations are presented.

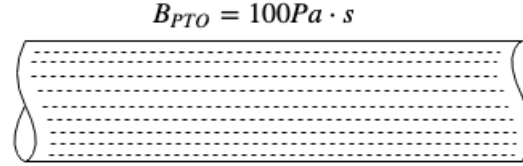
The first configuration is a simple example where the absorbed power is calculated by a multiplication of the damping force and the deformation velocity and is averaged over one wave period[19],

$$\tilde{P} = \overline{F \cdot U} \quad (\text{F.68})$$

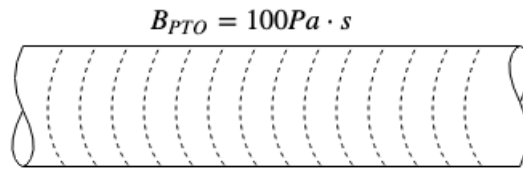
where  $F$  is the force (acting on the body) and  $U = \partial \delta \lambda / \partial t$  is the deformation velocity. The force that is absorbed by the wave energy converter, is equal to the force due to damping  $F_{PTO}$  and  $F_{rad,B}$ , which is defined



(a) Simple approach for bending and bulging.



(b) EAP in longitudinal direction for bending.



(c) EAP in circumferential direction for bending.

Figure F.16: Mode shapes of a bending tube.

for bending and bulging:

$$\begin{aligned}
 F &= F_{abs}^{(3)} = \sum_{n=1}^5 \int_L (B_{PTO} + b^{(3)}(\omega)) W_n \dot{q}_n(t) \cdot dx \\
 F &= F_{abs}^{(4)} = \sum_{n=1}^6 \int_L \left( B_{PTO} + \frac{h_s S_s b^{(4)}(\omega)}{\rho R_s} \right) \cdot \frac{\partial X_n}{\partial x} \dot{c}_n(t) dx
 \end{aligned} \tag{E69}$$

The velocity  $U$  is also defined for both motions:

$$\begin{aligned}
 U &= U^{(3)}(x, t) = \frac{\partial w(x, t)}{\partial t} = \sum_{m=1}^5 W_m(x) \dot{q}_m(t) \\
 U &= U^{(3)}(x, t) = \frac{\partial}{\partial t} \frac{\partial \chi(x, t)}{\partial x} = \sum_{m=1}^6 \frac{\partial X_m}{\partial x} \dot{c}_m(t)
 \end{aligned} \tag{E70}$$

The absorbed power is averaged over one wave period, which is calculated by:

$$\begin{aligned}
 \bar{P}^{(3)}(\omega, T) &= \frac{1}{T} \int_T \sum_{n=1}^5 \sum_{m=1}^5 \int_L (B_{PTO} + b^{(3)}(\omega)) \dot{q}_n(t) W_n(x) W_m(x) \dot{q}_m(t) \cdot dx \cdot dt \\
 \bar{P}^{(4)}(\omega, T) &= \frac{1}{T} \int_T \sum_{n=1}^6 \sum_{m=1}^6 \int_L \left( B_{PTO} + \frac{h_s S_s b^{(4)}(\omega)}{\rho R_s} \right) \cdot \frac{\partial X_n(x)}{\partial x} \dot{c}_n(t) \frac{\partial X_m(x)}{\partial x} \dot{c}_m(t) \cdot dx \cdot dt
 \end{aligned} \tag{E71}$$

where the time-dependent bending and bulging velocities  $\dot{q}_n$  and  $\dot{c}_n$  are given as,

$$\begin{aligned}
 q_n(t) &= \zeta_n(x, \omega) \cdot e^{-i\omega t} \quad \rightarrow \quad \dot{q}_n(t) = -i\omega \cdot \zeta_n(x, \omega) \cdot e^{-i\omega t} \\
 c_n(t) &= \xi_n(x, \omega) \cdot e^{-i\omega t} \quad \rightarrow \quad \dot{c}_n(t) = -i\omega \cdot \xi_n(x, \omega) \cdot e^{-i\omega t}
 \end{aligned} \tag{E72}$$

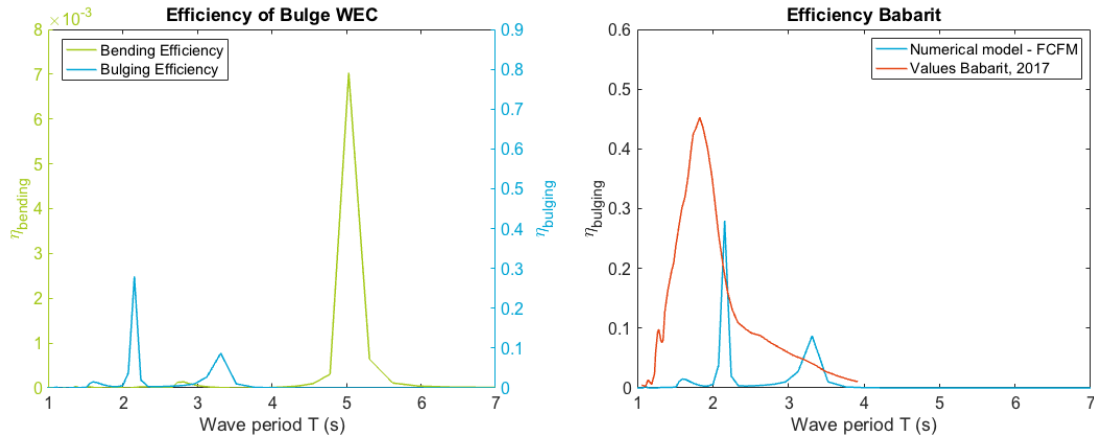
Rearrangement of Equation E.70 results in a mean absorbed power:

$$\begin{aligned}\tilde{P}^{(3)}(\omega, T) &= \text{Re} \left\{ \frac{1}{T} \int_T \omega^2 (B_{PTO} + b^{(3)}(\omega)) \sum_{n=1}^5 \sum_{m=1}^5 \int_L W_n(x) W_m(x) \cdot \zeta_n(x, \omega) \zeta_m(x, \omega) dx \cdot e^{-2i\omega t} dt \right\} \\ \tilde{P}^{(4)}(\omega, T) &= \text{Re} \left\{ \frac{1}{T} \int_T \omega^2 \left( B_{PTO} + \frac{h_s S_s b^{(4)}(\omega)}{\rho R_s} \right) \sum_{n=1}^6 \sum_{m=1}^6 \int_L \frac{\partial X_n(x)}{\partial x} \frac{\partial X_m(x)}{\partial x} \cdot \xi_n(x, \omega) \xi_m(x, \omega) dx \cdot e^{-2i\omega t} dt \right\}\end{aligned}\quad (\text{E.73})$$

The efficiency of the wave energy converter is defined by the ratio between the mean absorbed wave power of the WEC ( $P_{wec} = \tilde{P}$ ) and the mean wave energy per meter crest width of amplitude  $\zeta_I$ :

$$\eta_{wec} = \frac{P_{wec}/L}{J_W} \quad (\text{E.74})$$

where  $L$  denotes the length of the WEC and  $J_W = \rho g^2 \zeta_I^2 / 4\omega$  is the mean wave energy of a wave of 1 m width [72]. The efficiency of the bulge WEC is shown in Figure E.17a where the solid blue line represents the WEC energy due to bulging and the orange line represents the bending WEC efficiency.



(a) Numerical model with FCFM

(b) Comparison with bulging efficiency with [8]

Figure E.17: WEC efficiency calculated by Equation E.74 in subfigure E.17a and validation of bulging WEC efficiency of [8] in subfigure E.17a

In Figure E.17b, the result of the capture width of Babarit et al. [8] is plotted, who observed only bulging in their model. The capture width (CW) is non-dimensionalised as  $CW/L$ , which has the same definition as  $\eta_{bulging}$ . A comparison between the WEC efficiency for bending and bulging (in Figure E.17 results in a dominance of energy conversion due to bulging. The magnitude of energy conversion due to bulging is approximately 40 times larger than the energy conversion due to bending. The values of bulging are also compared to the total absorbed power as calculated by Babarit et al. for an damping value of  $B_{PTO} = 100 Pa \cdot s$ . The red line in Figure E.17b shows the result of Babarit et al., where different boundary conditions of the WEC are analysed. For the FCFM results, a value of  $B_{PTO} = 100 Pa \cdot s$  is used, but the local peaks differ from the values obtained by Babarit et al. The difference in boundary conditions and the difference in observed mode shapes and eigenfrequencies of each mode are a limitation of this comparison. Validation of these results is therefore difficult.

Since the SBM S3 (which is observed by Babarit et al.) converts energy of the WEC by Electro Active Polymer (EAP) rings (as shown the configuration of Figure E.16c) the values are also different for these configurations.

Electro Active Polymers convert energy due to stress in the wall, which should be adjusted to convert bending energy of the WEC. A new configuration (of Figure E.16b) is suggested to extract energy from the bending tube. Electro Active polymers are aligned in the longitudinal direction of the tube, where deformations are converted into an electrical potential. The power extracted in this approach is estimated by the elastic strain energy due to a bending moment. The elastic strain energy due to a bending moment in a beam

is defined by [31]:

$$U = \int_0^L \frac{M_{bend}^2(x)}{2EI} dx \quad (E.75)$$

where  $U$  is the elastic strain energy,  $bend(x)$  is the bending moment,  $E$  is the Young's modulus and  $I$  represents the area moment of inertia. Since the bending moment is related to the deformations by  $M(x) = EI \frac{\partial^2 w(x,t)}{\partial x^2}$ , the elastic strain energy is rewritten into:

$$U = \int_0^L \frac{EI}{2} \sum_{n=1}^N \left( \frac{\partial^2 W_n(x)}{\partial x^2} \cdot q_n(t) \right)^2 \cdot dx \quad (E.76)$$

The elastic strain is related to the PTO damping coefficient ( $B_{PTO}$ ) in the equation of motion for bending. This equation (Equation E.27) is rewritten into:

$$\sum_{m=1}^N [-\omega^2 (M_{nm} + A_{nm}) - i\omega (B_{nm} + B_{PTO}) + K_{nm}] \zeta_n = F_{FK,n}(\omega) \quad (E.77)$$

where the mechanical or PTO damping coefficient  $B_{PTO}$  is combined with the radiation damping, which is related to the absorbed energy of the WEC from the waves. Since power is inserted into Equation E.74 to define the WEC efficiency  $\eta_{WEC}$ , the strain energy is converted into power by

$$\tilde{P}(\omega) = \frac{\bar{U}}{T} = \text{Re} \left\{ \frac{EI}{2T^2} \int_T \sum_{n=1}^5 \sum_{m=1}^5 \int_0^L \frac{\partial^2 W_n(x)}{\partial x^2} \cdot \zeta_n \cdot \frac{\partial^2 W_m(x)}{\partial x^2} \cdot \zeta_m \cdot dx \cdot e^{-2i\omega t} \cdot dt \right\} \quad (E.78)$$

The values of  $\zeta_n$  and  $\zeta_m$  are found by the solution of Equation E.77. In Figure E.18 the results of the WEC efficiency for a PTO damping coefficient  $B_{PTO} = 50 \text{ Pa} \cdot \text{s}$  and  $B_{PTO} = 100 \text{ Pa} \cdot \text{s}$  are plotted. This figure confirms that more power is absorbed and the efficiency is increased for a higher PTO damping coefficient. The order of absorbed energy due to bending corresponds to the WEC efficiency in Figure E.17a. The difference between these two graphs is of a factor two, which is due to the configuration of the PTO. Validation in the form of experiments should give more insight into the right estimate of the absorbed power of a WEC.

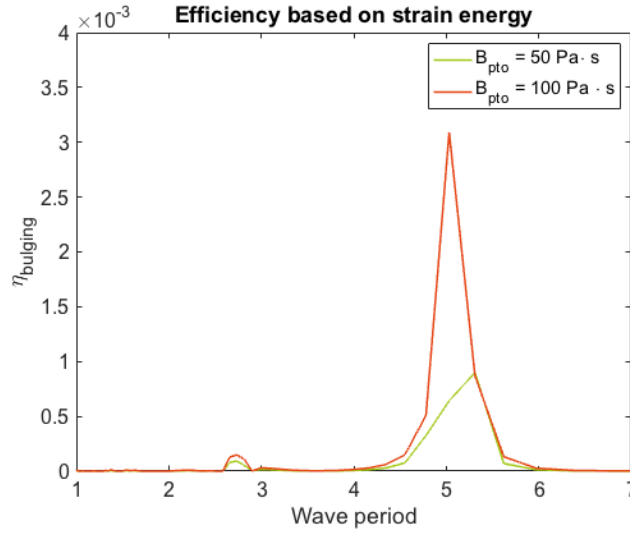


Figure E.18: WEC efficiency based on Equation E.78.

## E.4. Validation and verification

The results found in the previous section are validated and verified partly with experiments and recent research. Since the results found by Fathi et al. do not contain the dimensions and material characteristics of the tube in its two 'surge-pressure' modes, these calculations are only used to verify the hydrodynamic coefficients based on visual correspondence. Figure E.4 shows some similarities, but in Figure E.4b the influence

of the mode shape is missing. A comparison of Figure E.4a with the hydrodynamic coefficient of the bulging tube motions of Figure F.19 shows two major differences. The values on the x-axis and both y-axes differ from the figure of Fathi et al., but the ratio between the peak values of the added mass and damping coefficients is approximately the same. Figure E.4a claims that for higher modes, the peaks of the added mass and damping are shifting towards the lower wave periods, which cannot be obtained from Figure E.20a. [24].

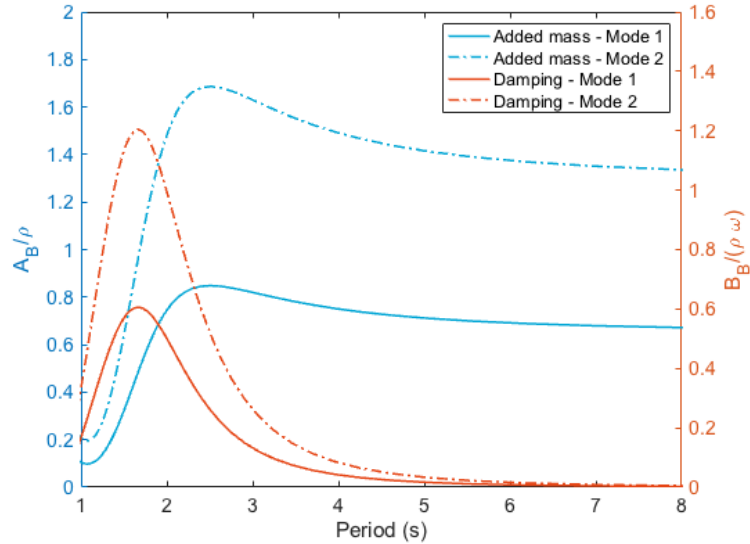


Figure F.19: Hydrodynamic coefficients of first bulging mode against wave period.

One important remark has to be made about the 'surge-pressure' mode shapes, which are not normalised in the same way as done for modal analysis. The mode shapes found by Fathi et al. are given in Figure F.20 and these can be compared to the mode shapes that are found by the FCFM. Some differences can be obtained. The mode shapes of Fathi et al. are normalized by setting the maximum values to 1, while for the current model the integrated area under the mode shape  $X$  is set to zero. Since the hydrodynamic coefficients in the FCFM are related to  $\partial X/\partial x$ , first two mode shapes (and also the higher modes) show some differences. This is one of the arguments for the differences in the values of the hydrodynamic coefficients found by the FCFM and the research of Fathi et al.

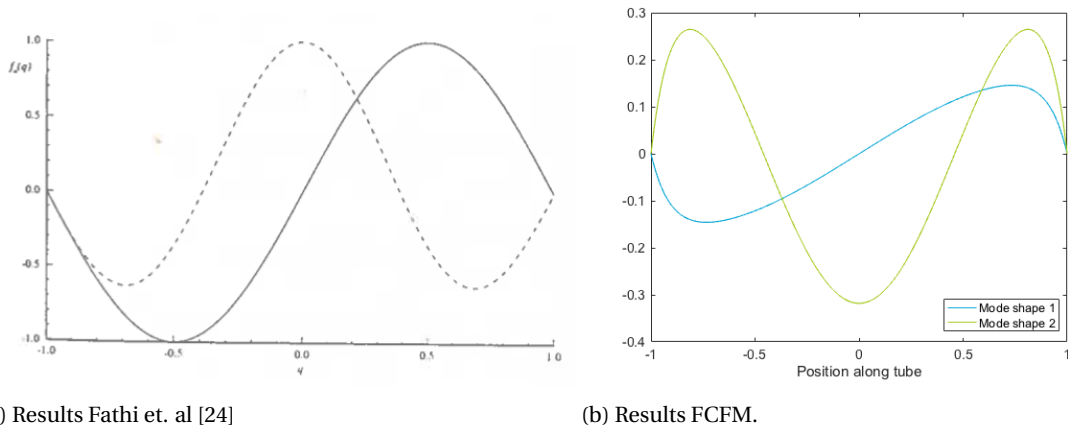


Figure F.20: Exciting forces of a bulging tube, where the first mode is represented by the solid curves and the second with the dashed curves in F.20a.

Another result found by Fathi et al. is the exciting force of the 'surge-pressure' modes of a distensible tube. The results of Fathi et al. and the FCFM are shown in Figure E.21. In both graphs the first two modes are plotted, where in both figures the peak decreases and it shifts to lower periods. A small shift between the

modes is observed, which could be caused by deviations in mode shape and dimensional characteristics of the tube. A small local minimum is observed in Fathi's results for the first mode shape, which show the same behaviour of the exciting forces in short waves. These wiggles are also visible in Figure F.13, where these peaks are coupled to the wave length (and therefore wave period) of the mode shapes. The magnitude of the peaks is adapted due to the normalisation of the mode shapes, where differences are caused by 3D effects and the differences in geometrical characteristics of the observed tube.

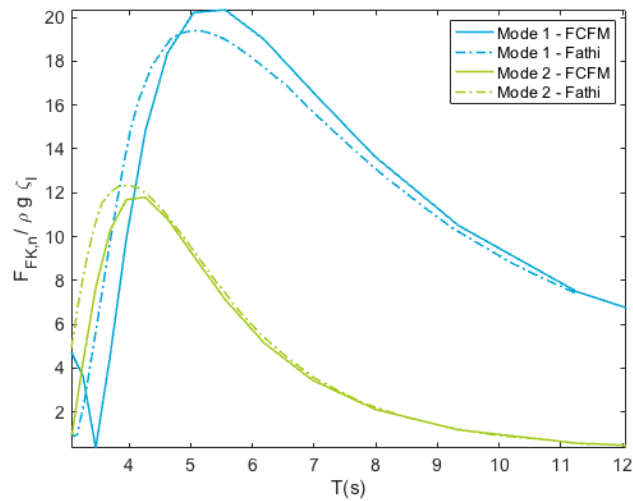


Figure F.21: Exciting forces of a bulging tube.

The results of bending are also verified with the results obtained by Fathi et al. [24]. They observed 4 bending modes which are given in Figure E.22a. These mode shapes are the same as the mode shapes obtained by the FCFM (see Figure E.22b). The difference is found in the magnitudes of the mode shapes, which is due to the normalisation procedure.

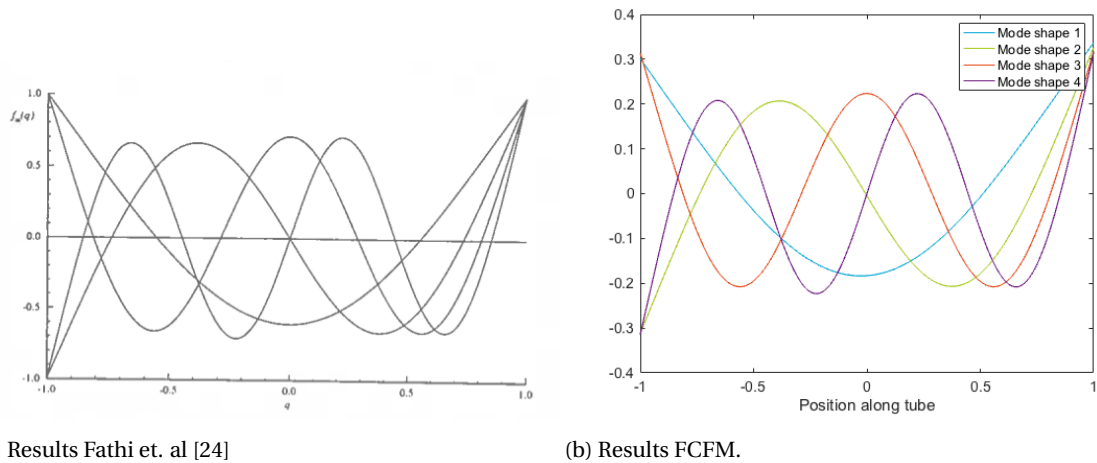
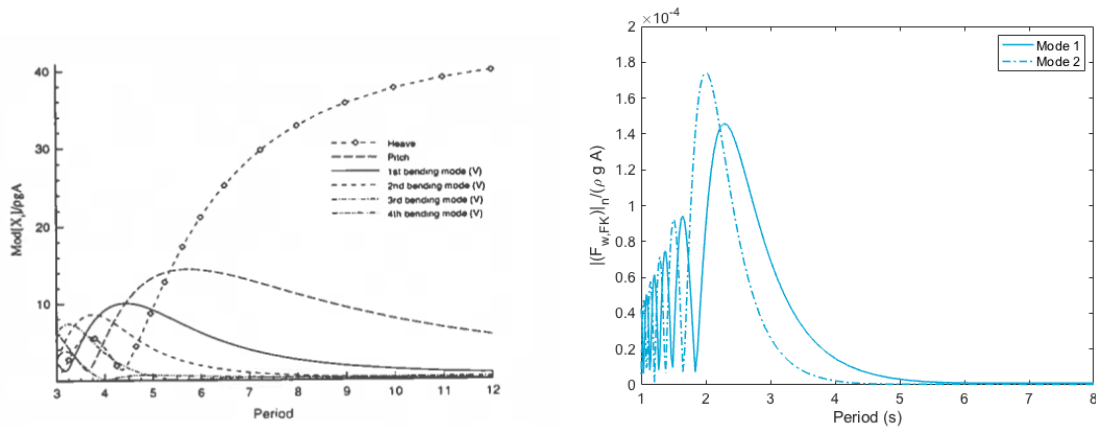


Figure E.22: Mode shapes of a bending tube.

For the bending modes the hydrodynamic coefficients are not given by Fathi et al., but results of the wave exciting force for the heave, pitch and first four bending modes are presented in Figure E.23a. The excitation force is given with respect to the wave period, where Figure E.23b shows the resulting values of the wave exciting force found by the FCFM (for only the first two bending modes). The values of the wave exciting force is scaled with  $\rho g \zeta_l$  where the peak values are increasing for increasing order, which is contrary to the results of Fathi et al. This difference can be caused by different normalisation of the modes, which are checked by a second run of the model with normalisation and length-scales as used by Fathi et al. The results of this run for the first four modes are plotted in Figure E.24a and the exciting forces for these four modes are plotted in Figure E.24b. The analogy between Figure E.24b and Figure E.23a is improved largely by the length scale. Since the directional cosines are included in Equation E.20, a higher length-scale will increase the values of the peaks in Figure E.23b. Comparison between the Figures E.23b and E.24b proves that the peak values depend on the length scales in combination with the mode shapes.

The major differences between the FCFM and the results of Fathi et al. in Figure E.24b are caused by 3D effects and tuning of the geometry characteristics. Some dimensions of the tube, like the mass, wall thickness and submersion depth, are not presented in the article of Fathi et al.. Since these values are not specifically given by Fathi et al., the differences could be only given by reverse engineering. The results of this second run with different length scale and normalisation supply the cause of the differences found for the differences in the excitation force in the first two bending modes.

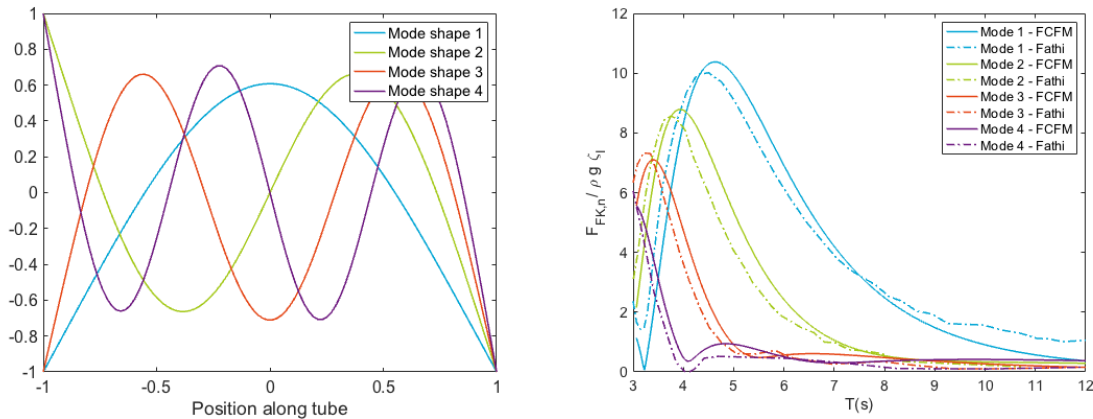
Since the bulging modes are based on the research executed by Babarit et al. [8], their validation could be applied to the FCFM results as well. Experimental values are plotted in Figure E.15 where the red dots represent the experimental values. The material and geometry characteristics are presented in Table E.2, which correspond to the values used by Babarit et al. The blue line in Figure E.15 represents the results of the FCFM and the green line shows the numerical results of Babarit et al. [8]. The numerical values of Babarit et al. show some differences for the peaks, which is due to a difference in eigenfrequencies of both numerical methods. As mentioned before two of his eigenfrequencies, at  $\omega = 0.8724$  Hz and  $\omega = 2.814$  Hz are not included in the FCFM, but these values are not visible in the graph as well. Fluid damping of the inner fluid and wall damping is not taken into account, and the material characteristics like the distensibility  $D$  of the tube is tuned with respect to the experimental values. So difference between numerical and experimental values should be fixed by the including damping terms and a proper definition of the distensibility of the material. The values found by the FCFM (denoted by the blue line), differ from the values found by the method of Babarit et al. especially for the resonance periods, which are shifted with 0.5 s. The absence of the three-dimensional effects of the radiation coefficients on the mode shapes and the assumption that diffraction effects will be small, could cause this shift in resonance period.



(a) Results Fathi et. al [24]

(b) Results FCFM at  $d/R = 1.25$ .

Figure E.23: Exciting forces of a bending tube.



(a) Results Fathi et. al [24]

(b) Results FCFM.

Figure E.24: Mode shapes and exciting forces of a bending tube (with length scale  $L/2$ ).

For further research, it could be valuable to execute experiments with a well-known elastic material for a slender tube. Since most elastic materials do not have linear behaviour, some extra assumptions have to be made about the elasticity of the material, for example taking a visco-elastic material for the tube's wall. Results for the pressure distribution along the tube, would increase insight into the contribution of the radiation, diffracted and incident pressure components along the beam. Since the model does not include the viscous damping of the inner fluid and the wall damping, this would be interesting to add to the model. And finally, the three-dimensional interaction of the two-dimensional hydrodynamic coefficients should be taken into account, including diffraction of the incoming wave.

### Check assumptions of model

The model excludes viscous and diffraction forces, which is assumed in Appendix E and the previous sections of this Appendix. Since a linear gravity wave is assumed in an incompressible, inviscid and irrotational fluid, the viscous forces are neglected. Diffraction of the incoming wave is neglected to keep the model simple, but it can be added in a later stage of the model. Figure E.25 shows roughly the validity of the linearized theory based on the assumption that the wavelength ( $\lambda$ ) is much greater than the tubes diameter ( $D$ ). For a small ratio of  $\lambda/D$ , the wave slope is high and diffraction or even breaking of the waves is of importance [45].

The second region that is highlighted in Figure E.25 is the viscous region, where the ratio between wave height ( $H$ ) and the tube's diameter is of interest. Since linear wave theory indicates a orbital movement of a particle in a deep water wave [34], a  $H/D$ -ratio (where  $H = 2 \cdot \zeta_I$ ) implies a small circular particle path with respect to

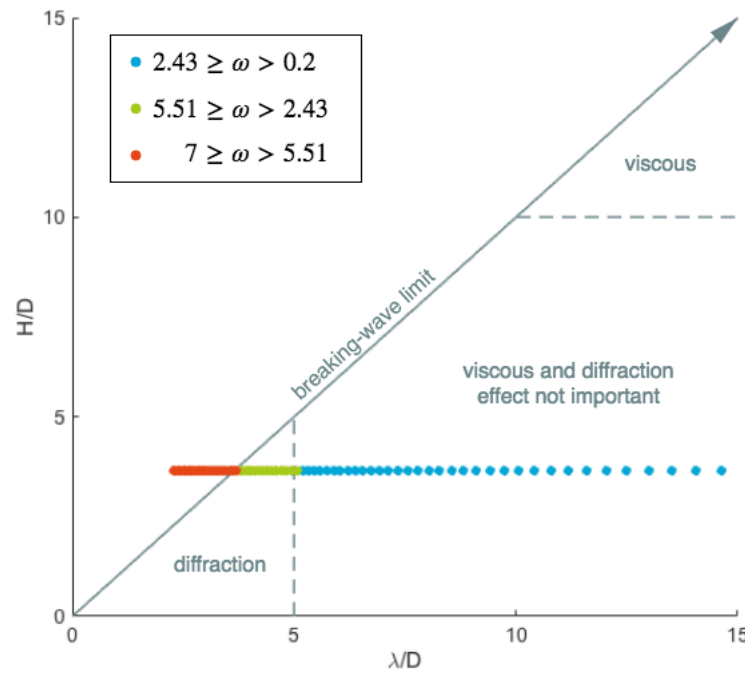


Figure E.25: Regions of importance of viscous and diffraction forces on the structure. Figure adapted from [45].

the tubes diameter (where  $D = 2 \cdot R_s$ ). For large ratios of  $H/D$ , the dimension of the particle path and tube's diameter are of the same order and flow separation will occur. Flow separation is a viscous effect, where the flow is change with respect to the flow assumed in linear potential theory. As shown in Figure E.25, this means that some of the observed frequencies are out of the range where viscous and diffraction effects or not important. To fulfil the assumptions, two options could improve the current model:

- Restrict the range of incident wave frequencies to the values inside the range where viscous and diffraction effects can be neglected. So for the given tube dimensions (of Table F.2) this means that  $\omega \leq 2.43$  Hz.
- Add diffraction to the model, where diffraction of the end effects of main importance. A considerable amount of strip theory method has included diffraction in their numerical codes [8, 36, 69], which means that it would be possible to extend the model with diffraction.

## F.5. Conclusions

This appendix drawn some conclusions to the main question and secondary questions 2 and 3 of Section A.2:

### 2. How can Frank's close-fit method be adapted to deal with deformable bodies in still water?

In Appendix E relevant literature with respect to the response of a deformable body in waves is shown. The calculations of the modal response is investigated in this Appendix. The Frank close-fit method is not implemented for a deformable body in still water, because the body is not driven into a forced oscillation, so radiation is not of interest. The response of a bulge WEC in still water is only focussing on the dry bending and bulging modes. In this Appendix these modes are derived by a mode superposition method. The results of this 'dry' mode shapes and frequencies deviate a little bit from the modes found by Babarit et al. which is caused by a difference in boundary conditions for the tube. Besides the boundary conditions, Babarit et al. observed some 'numerical' eigenfrequencies and corresponding modes, which are not physically correct.

### 3. How can Frank's close-fit method be adapted to deal with deformable bodies operating in regular waves?

The response of a bulge WEC is observed in this section, where loads due to incoming and radiated waves are included. The 'dry' mode shapes and frequencies are transformed into 'wet' mode shapes and frequencies, where the hydrodynamic added mass reduces the value of the natural frequency of the individual modes. Mode superposition is utilized and the normal coordinates of each mode are obtained for a tube operating in incident gravity waves and with a certain level of radiation damping. The results that are found are compared to the results found by Babarit et al. [8] and Fathi et al. [24]. In general, the values of the numerical model show the same behaviour as the reference work, but differences are obtained due to differences in geometrical dimensions, boundary conditions and normalisation methods.

The main goal of the current study was to identify the advantages of the implementation of the FCFM into a hydro-elastic problem. The results of this Appendix show that the implementation is promising, but that some differences are found between several methods to calculate hydro-elastic response of a bulge WEC. The implementation of the Frank close-fit method results into hydro-elasticity is shown to reduce the computational time, since the radiation problem is solved by only 36 panels along the submerged cross-section. The findings of this research could provide insight into a hydro-elastic problems as an estimation of the final performance of a wave energy converter or similar types of application.

Considerably more work needs to be done to determine the three-dimensional interaction of the segments along the tubes length and the diffraction effects on the hydro-elastic response of a bulge WEC. Implementation of some viscous terms could increase the validity of the model, since the wall damping and inner fluid damping are excluded in the current model.